

Doctoral school: Science of matter, Radiation and the Environment
Discipline: Theoretical, Analytical and Physical Chemistry

**Theoretical Study and Modeling of the Phase Transitions between
Alumina (Meta)stable Structures**

Presented by

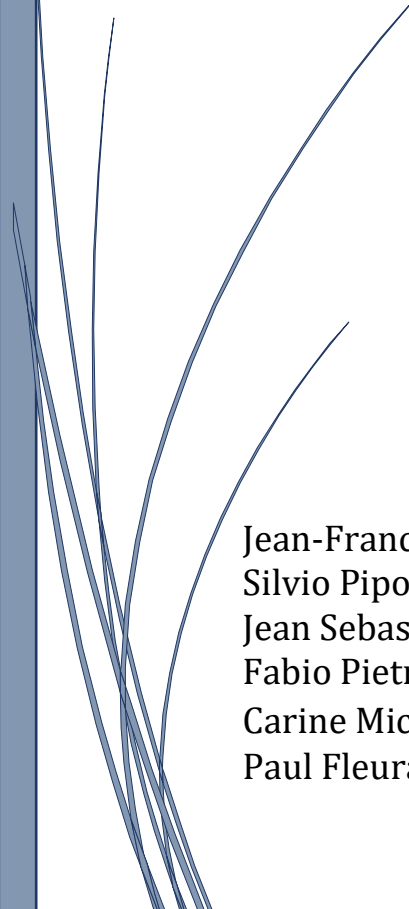
Mohammad Hellani

Defended on 27/10/2022

Thesis submitted for the degree of
Ph.D. of the University of Lille

Jury members

Jean-Francois Paul	Professor, Lille University	Directeur
Silvio Pipolo	Assistant Professor, Lille University	Co-supervisor
Jean Sebastien Filhol	Professor, Montpellier University	Reviewer
Fabio Pietrucci	Associate Professor, Sorbonne University	Reviewer
Carine Michel	CNRS Research Director, ENS of Lyon	Examiner
Paul Fleurat-Lessard	Professor, University of Bourgogne	Examiner - President



Ecole Doctorale Sciences de la Matière, du Rayonnement et de l'environnement
Discipline : Chimie Théorique, Analytique et Physique

**Etude Théorique et Modélisation des Transitions de Phase entre
des Structures (Méta)stables d'Alumine**

Présentée par

Mohammad Hellani

Soutenue le 27/10/2022

Thèse présentée pour le diplôme de
Docteur de l'Université Lille

Membres du jury

Jean-Francois Paul	Professeur, Université de Lille	Directeur
Silvio Pipolo	Maître de conférences, Université de Lille	Co-encadrant
Jean Sebastien Filhol	Professeur, Université de Montpellier	Rapporteur
Fabio Pietrucci	Maître de Conférences, Sorbonne Université	Rapporteur
Carine Michel	Directrice de recherche CNRS, ENS-lyon	Examineur
Paul Fleurat-Lessard	Professeur, Université de Bourgogne	Examineur – Président

"In the midst of difficulty lies opportunity." Albert Einstein

Abstract

Gamma alumina is widely used as support for catalysis but its structure is not fully defined as it is only poorly crystallized. A possible method to overcome this lack of experimental data is to study it theoretically, by classical molecular dynamics as the crystallization of liquid alumina occurs through the formation of gamma alumina. It is then possible to define various crystallographic phases which will be related to the phase known experimentally and in a second step to define the reaction paths of the phase transitions as well their activation free energies.

However, the direct simulations of transformations between crystalline and amorphous systems are very hard due to the extremely low nucleation rate and to the difficulty of defining the reaction coordinate. Finding a general collective variable (CV) scheme for such a family of transformations is, in fact, a hard task, but the PathCV-PIV combinations has been proven to be successful in the case of water. In this work, we perform molecular dynamics simulations on a pure alumina system showing that using accelerated approaches, as Metadynamics, and the PathCV-PIV CV the challenging task of simulating phase transitions in materials at the atomistic level can be accomplished. The use of this CV allows tracking transitions among liquid, amorphous and crystalline forms of alumina providing transformation mechanisms and free energy landscapes. We will show the application of such an approach to the simulation of the crystallization of amorphous alumina at different temperatures and characterize the crystallization mechanics of gamma alumina showing that the aluminum-oxygen reciprocal orientation precedes the oxygen network ordering. Finally, we studied the connection between stable and metastable crystalline phases of alumina and the effect of temperature on the free energy landscape.

Keywords: Phase Transitions, Free Energy Profile, Metadynamics, classical MD, Alumina phase structures.

Resumé

L'alumine gamma est largement utilisée comme support en catalyse même si sa structure n'est pas complètement définie car elle n'est mal cristallisée. Une méthode possible pour pallier ce manque de données expérimentales est de l'étudier théoriquement, par la dynamique moléculaire classique la cristallisation de l'alumine liquide qui peut conduire à l'alumine gamma. Il est alors possible de définir différentes phases cristallographiques connues expérimentalement et dans un second temps de définir les chemins réactionnels des transitions entre ces phases ainsi que leurs énergies libres d'activation liées à ces transformations.

Cependant, les simulations directes de transformations entre systèmes cristallins et amorphes sont très difficiles en raison du taux de nucléation et de la difficulté à définir la coordonnée de réaction. Trouver un schéma général de variables collectives (CV) pour une telle famille de transformations est, en fait, une tâche difficile, mais les combinaisons PathCV-PIV se sont avérées efficaces dans le cas de l'eau. Dans ce travail, nous étudions par dynamique moléculaire les transformations de l'alumine montrant qu'en utilisant des approches accélérées, comme la métadynamique, et la variable collective PathCV-PIV, il est possible de simuler les transitions de phase dans les matériaux. L'utilisation de cette variable collective permet de suivre les transitions entre les formes liquides et cristallines de l'alumine en proposant des mécanismes de transformation et des paysages d'énergie libre.

Dans cette thèse, nous démontrons que l'application d'une telle approche à la simulation de la cristallisation de l'alumine à différentes températures est possible et nous caractériserons les mécanismes de cristallisation de l'alumine en alumine gamma en montrant que l'orientation réciproque aluminium-oxygène précède l'ordre du réseau d'oxygène. Enfin, nous avons étudié les liens entre les phases cristallines stables et métastables de l'alumine et l'effet de la température sur le paysage énergétique libre.

Mots clés: Transitions de phases, Profil d'énergie libre, Métadynamique, MD classique, structures de phases d'alumine.

Acknowledgements

This thesis couldn't have taken place without the financial support of Université de Lille and UCCS Laboratory.

I would like to express my deepest gratitude to my supervisors, Jean-Francois Paul and Silvio Pipolo, for the opportunity they provided me with to pursue this doctoral research. Their unwavering support, invaluable guidance, and encouragement have been instrumental in shaping the trajectory of my academic journey. Silvio, in particular, deserves special recognition for his dedicated assistance and for being by my side at every crucial juncture of my work. It was a pleasure to work with you two.

To my parents, whose boundless love and encouragement have been the base of my existence, I owe an immeasurable debt of gratitude. Your constant and enduring support and belief in my dreams have fueled my determination and shaped my journey in profound ways. To my dearest brother Ali, your constant backing and faith in my abilities have been a source of strength and inspiration. Your presence has been a guiding light, and I am endlessly grateful for your love and support.

To my dearest friends Nouredin Osseiran and Siveen Thleijeh, your presence has been a source of strength throughout this journey. From the late-night talks to the celebratory moments of breakthroughs, you have been a constant reminder of the beauty of true friendship. The memories we've shared and the challenges we've overcome have not only enriched this experience but have also left an unforgettable mark on my life. To my beloved Joelle Al Aseel and Marwa Saab, whose infectious spirits and warm presence brought countless smiles to my days, I am extremely thankful.

Lastly, to my friends Ali Qais, Ahmed Caracalla, Wissal Adhami, Berta Farah, Sandy Albacha, Ibrahim Hatoum, Balsam Hamieh, Wafa Ksila, Afef Salhi, Grece Abdalla and Nicolas Mtr thank you for your consistent assistance and support. I am deeply appreciative of the time, effort, and insights you shared along this journey.

Thank you all for being part of this experience.

Table of contents

Abstract.....	1
Resumé.....	2
Acknowledgements.....	4
Table of Figures	10
Chapter 1 LITERATURE OVERVIEW	16
1.1 Introduction.....	17
1.2 Transformations in condensed matter	19
1.2.1 Phase transitions.....	19
1.2.2 Structural Phase Transitions and their Energy Profile	19
1.3 Aluminum Oxide and it's phase structures	21
1.4 Aim of the research work.....	24
Chapter 2 Methods	26
2.1 Introduction to Electronic Structure.....	27
2.2 The Schrodinger Equation.....	27
2.3 Molecular Dynamics (MD) Simulations.....	29
2.3.1 Introduction to computer Simulations.....	29
2.3.2 Principle of MD.....	30
2.3.3 Classical MD.....	32
2.3.4 Force Fields.....	33
2.3.5 Long Range Electrostatic forces	34
2.3.6 Velocity Verlet Algorithm	35
2.3.7 System Size and Periodic Boundary Conditions.....	36

2.3.8	Molecular Dynamics Ensembles	37
2.3.9	Molecular Dynamics limitations	38
2.3.10	Enhanced Molecular Dynamics	38
2.4	Analysis Methods	43
2.4.1	Radial Distribution Functions and coordination numbers.....	43
2.4.2	X-Ray Diffraction pattern	44
2.4.3	Steinhardt's order parameters.....	45
2.4.4	Mean square displacements.....	46
Chapter 3	Computational Details	47
3.1	Simulations Details	47
3.1.1	For classical Molecular Dynamics	47
3.1.2	Quantum simulations.....	48
3.2	Codes Used.....	48
3.2.1	GROMACS	49
3.2.2	PLUMED	49
3.2.3	CP2K.....	49
3.2.4	VMD.....	50
Chapter 4	Crystallization of Gamma alumina.....	52
4.1	Preparation of structures.....	53
4.1.1	Reference structures preparation.....	53
4.1.2	Amorphous structures:	54

4.2	Crystallization of Gamma Alumina	55
4.2.1	Crystallization of Alpha Alumina	55
4.2.2	Crystallization of Gamma Alumina	57
4.2.3	Temperature dependence.....	61
4.2.4	DFT energy calculations:	68
Chapter 5	Transitions among crystalline phases	70
5.1	Optimization of Switching Functions for the PIV vector	71
5.2	Transitions between Alpha and Gamma structures.....	72
5.2.1	Alpha to Gamma phase transition	72
5.2.2	Temperature Dependence:.....	78
5.3	Transitions between Theta and Gamma structures	89
5.4	Transitions between Alpha and Theta structures	95
Chapter 6	Conclusions	99
Chapter 7	References	104

Table of Figures

Figure 1: 3D representation of the Gibbs free energy surface. Metastable and stable phases are depicted, corresponding to local and global minima, respectively.[10]	20
Figure 2: Schematic of the main phase transformations of aluminas upon heat treatment[19]......	23
Figure 3: The basic Molecular Dynamics loop.....	31
Figure 4: different types of potentials used for a force field.....	33
Figure 5: schematic representation of periodic boundary conditions in 3D, primary real cell located in the middle surrounded by the image cells	37
Figure 6: example of metadynamics simulations: the free energy landscape (black line) is traced as a function of a collective variable, together with the sum of the landscape plus the bias potential at different times (colored lines)	39
Figure 7: Free energy profile (black line) as function of reaction path sampled using distinct overlapping Umbrella windows (blue parabolas)	42
Figure 8: Scheme representing the strategy to calculate the RDF (dotted circular shell) of the reference atom in red by estimating the probability of the blue atoms within the circular shell.	44
Figure 9: 3D graph showing the time progress of the metadynamics simulation starting from the amorphous structure (Am) to the alpha structure (α) passing by Gamma structure (γ) in the s - z space.	56
Figure 10: Comparison between partial Al-Al radial distribution functions calculated for Amorphous structure (Am), alpha alumina structure (α), and two gamma aluminas (the Reference and Crystallized Gamma obtained in this work). X-ray Diffraction pattern calculate for	

experimental gamma structure (A), the reference gamma from literature (B) and the crystallized gamma structure (C). 57

Figure 11: 3D graphs showing the convergence of the Q_6 [O - O] (A), Q_6 [Al - O] (B) and Volume (C) as function of time projected along the path collective variable S, alongside with the Free Energy Surface (D) of the transformation as a function of the same parameter. The shadowed region shows the initial basin on the left of the barrier. Snapshots of the initial (Am) and final crystallized (G) structures of the transformation. 58

Figure 12: A) Steinhardt parameters Q_6 [O - O], Q_6 [Al - O], Q_4 [Al - O] and the coordinate “s” as a function of time during the metadynamics. B) Angular coefficient of the linear interpolation of the different plots (in A) done on an increasing set of (time ordered) points along the metadynamics..... 61

Figure 13: 3D graph showing the unconverged free energy of the metadynamics simulations starting from the amorphous structure (around $s \sim 1.1$) to the gamma structure (around $s \sim 1.9$) in the s - z space at low temperatures. 62

Figure 14: 3D graphs showing the Steinhardt parameter Q_6 [O - O] (A), Q_6 [Al - O] (B) and Volume (C) as function of time projected along the path collective variable S, alongside with the Free Energy Surface (D) of the transformation as a function of the same parameter s at 800 and 900K respectively. 63

Figure 15: Free Energy Profiles for the amorphous-gamma transformation (left) and RDFs of the initial and final state at low temperatures (800 - 1000K). 64

Figure 16: 3D graph showing the unconverged free energy of the metadynamics simulations starting from the amorphous structure (around $s \sim 1.1$) to the gamma structure (around $s \sim 1.9$) in the s - z space at high temperatures. 65

Figure 17: 3D graphs showing the Steinhardt parameter Q_6 [O - O] (A), Q_6 [Al - O] (B) and Volume (C) as function of time projected along the path collective variable s , alongside with the Free Energy Surface (D) of the transformation as a function of the same parameter s at 800 and 900K respectively. 66

Figure 18: Free Energy Profiles for the amorphous-gamma transformation (left) and RDFs of the initial and final state at low temperatures (1500 - 2000K). 67

Figure 19: Mean Square Displacements (MSDs) of the disordered system at different temperatures..... 67

Figure 20: Comparison between RDFs calculated from the DFT and classical MDs simulations for both gamma and alpha alumina structures..... 68

Figure 21: RDFs between Aluminum atoms alongside with different switching functions tested in this thesis. 72

Figure 22: 3D graphs showing the A) time progress of the metadynamics simulation at 1000K starting from the alpha to gamma structure as function of simulation time (ns) and B) Unconverged free energy profile in the $s - z$ space..... 74

Figure 23: Free Energy Surface (in Kcal/mol) of the alpha to gamma transition at 1000K as a function of parameter s 74

Figure 24: The variation of Steinhardt parameter Q_4 between different atoms of the system along the transition from alpha to gamma structure at 1000K as function of time(ns) (left) and s (right). 76

Figure 25: The variation of Steinhardt parameter Q_6 between different atoms of the system along the transition from alpha to gamma structure at 1000K as function of time (ns) (left) and parameter s (right)..... 77

Figure 26: The variation of volume of the system along the transition from alpha to gamma structure at 1000K as function of time (ns). 77

Figure 27: 3D graphs showing the A) time progress of the metadynamics simulation at 1200K starting from the alpha to gamma structure as function of simulation time (ns) and B) Unconverged free energy profile in the s - z space..... 79

Figure 28: Free Energy Surface (Kcal/mol) of the alpha to gamma transition at 1200K as function of parameter s. 79

Figure 29: The variation of Steinhardt parameter Q_4 between different atoms of the system along the transition from alpha to gamma structure at 1200K as function of time(ns) (left) and s (right). 80

Figure 30: The variation of Steinhardt parameter Q_6 between different atoms of the system along the transition from alpha to gamma structure at 1200K as function of time(ns) (left) and s (right). 81

Figure 31: 3D graphs showing the A) time progress of the metadynamics simulation at 1500K starting from alpha to gamma structure as function of simulation time (ns) and B) Unconverged free energy profile in the s - z space..... 82

Figure 32: Free Energy Surface (Kcal/mol) of the transition from alpha to gamma at 1500K as function of parameter s. 83

Figure 33: The variation of Steinhardt parameter Q_4 between different atoms of the system along the transition from alpha to gamma structure at 1500K as function of time(ns) (left) and s (right). 83

Figure 34: The variation of Steinhardt parameter Q_6 between different atoms of the system along the transition from alpha to gamma structure at 1500K as function of time(ns) (left) and s (right). 84

Figure 35: 3D graphs showing the A) time progress of the metadynamics simulation at 500K starting from the alpha to gamma structure as function of simulation time (ns) and B) Unconverged free energy profile in the s - z space.....	85
Figure 36: Free Energy Surface of the transition from alpha to gamma structure at 500K as function of parameter s.	85
Figure 37: The variation of Steinhardt parameter Q_4 between different atoms of the system along the transition from alpha to gamma structure at 500K as function of time(ns) (left) and s (right).	86
Figure 38: The variation of Steinhardt parameter Q_6 between different atoms of the system along the transition from alpha to gamma structure at 500K as function of time(ns) (left) and s (right).	87
Figure 39: Comparison between FES computed at different temperatures of the transition from alpha to gamma structure.	88
Figure 40: 3D graph showing the A) time progress of the metadynamics simulation at 1500K starting from theta to gamma structure as function of simulation time (ps) and B) Unconverged free energy profile in the s - z space.....	89
Figure 41: Free Energy Surface (Kcal/mol) of the theta to gamma transition at 1500K as function of parameter s.	90
Figure 42: The variation of Steinhardt parameter Q_4 between different atoms of the system along the transition from theta to gamma structure at 1500K as function of time(ns) (left) and s (right)	90
Figure 43: The variation of Steinhardt parameter Q_6 between different atoms of the system along the transition from theta to gamma structure at 1500K as function of time(ns) (left) and s (right).	91

Figure 44: 3D graph showing the A) time progress of the metadynamics simulation at 1200K starting from theta to gamma structure as function of simulation time (ps) and B) Unconverged free energy profile in the s - z space.....	92
Figure 45: Free Energy Surface (Kcal/mol) of the theta to gamma transition at 1200K as function of parameter s.	92
Figure 46: The variation of Steinhardt parameter Q_4 between different atoms of the system along the transition from theta to gamma structure at 1200K as function of time(ns) (left) and s (right).	93
Figure 47: The variation of Steinhardt parameter Q_6 between different atoms of the system along the transition from theta to gamma structure at 1200K as function of time(ns) (left) and s (right).	94
Figure 48: 3D graph showing the A) time progress of the metadynamics simulation at 1500K starting from the theta to alpha structure as function of simulation time (ns) and B) Unconverged free energy profile in the s - z space.....	95
Figure 49: RDFs of the 3 structures present in the transformation (theta, alpha and the structure I).....	96
Figure 50: The variation of Steinhardt parameter Q_4 between different atoms of the system along the transition from theta to alpha structure as function of time(ns) (left) and s (right).	97
Figure 51: The variation of Steinhardt parameter Q_6 between different atoms of the system along the transition from theta to alpha structure as function of time(ns) (left) and s (right).	98
Figure 52: Convergence of the Volume of unit cell during the transformation of theta to alpha structure.....	98

Chapter 1 LITERATURE OVERVIEW

1.1 Introduction

Glassy materials and their dynamics are essential for the development of many strategic technologies in the fields of telecommunications[1] (fiber optics, laser lenses), health[2] (biomaterials) and energy[3]. The lack of periodicity, symmetry and long-range order in amorphous materials make it difficult to determine their structure, at the atomic scale, using experiments. On the other hand, the structure of defect free crystalline materials can be described by specifying the structure of a single unit cell (defined by a small number of independent parameters and limited number of atoms). The unit cell can be determined experimentally from diffraction data obtained from X-ray and neutron sources. In amorphous material, due to their lack of long-range order, diffraction techniques only yield information related to pair correlations. A unique atomic scale definition cannot be obtained from this pair correlation data. This is the reason why computer simulation has played such an important role in determining the structure and dynamic processes of glasses.

Alumina (Al_2O_3) is one of the simplest covalent oxides that has received recent attention. Al_2O_3 particles are used as supports for catalytic nanoparticles, but the structure of the active phase (gamma-alumina) is still debated. Thin films are also used as protective layer that render unique chemical durability and mechanical strength on metals. Even though several studies have been carried out on crystalline alumina, the structure of pure Al_2O_3 glass has not been studied experimentally due to the difficulties involved in its synthesis, particularly in quenching Al_2O_3 melts.

The advent of high-speed computers since the late 1960s has transformed research in science and engineering by inserting a significant element in between theory and experiment: the computer simulation. In computer simulations, the models of the material and of the interaction

between the objects (atoms, molecules, particles ...) are provided by theorists while the calculations are carried out by the machine using an algorithm implemented in a suitable programming language. Using this method, realistic systems can be investigated which opens a road towards a better understanding of real experiments. Simulations have begun to appear frequently in experimental structural biology papers[4][5], where they are used both to interpret experimental results and to guide experimental work.

Computational structure prediction methods have been widely used for the prediction of structures such as proteins as well as crystal phases of materials, but they lack of information about transformation mechanisms and energetics. Molecular Dynamics is a simulation technique that propagates the displacement of atoms depending on forces and time and can be used to explore structures in materials. When kinetic barriers are higher than thermal energy, MD is not able to sample the configurational space and accelerated approaches and enhanced methods as metadynamics need to be used. Recently, a combination of enhanced sampling techniques with topological parameters has been proven to correctly describe thermodynamics properties of phase transitions in water [6]. The aim of this PhD work is to apply such a computational method to the study of phase transitions among glassy and crystalline phases of Alumina.

1.2 Transformations in condensed matter

1.2.1 Phase transitions

A structural phase transition takes place in a crystal when distortions or reorientations in lattice symmetry appear. It is considered as a fundamental phenomenon that changes the properties of solid-state materials. Being considered as ordering phenomena in crystals, solid-solid phase transitions are of fundamental importance because they directly control the microstructure of the materials[7] and greatly change the physical properties of the solid[8]. Therefore, enriching the theories and computational models in investigating the microscopic behavior of the different phases and the atomistic mechanism involved is crucial in solid state physics and chemistry[9]. A considerable number of experimental and theoretical works are devoted to the study of such transformations, and interest in them does not fade.

1.2.2 Structural Phase Transitions and their Energy Profile

First-order (discontinuous) transitions are of special interest due to their inherent behavior, which means that the system must overcome an extensive energy barrier in order to pass through one phase to another which can be seen from the illustrative Figure 1. The energy barriers are often too large to be crossed on achievable time-scales, hence a metastable structure instead of the stable one is often observed as the carbon diamond. On the other hand, if the barrier between the minima is small, the system will eventually jump into the global minimum. In general, the position of the local and global minima is temperature dependent.

The kinetics of the transformation depends on temperature and on the energy barrier (or called the activation energy). This activation energy can be thought as the magnitude of the

potential barrier separating the energy minima. It is the energy difference between the reactants and the activated complex (or transition state) which is the maximum on the transformation path free energy. The kinetic constant can be estimated through the relation:

$$k = A e^{-E_a/RT} \quad (1)$$

Where E_a is the activation energy for the reaction, A is the pre-exponential factor of the reaction, R is the universal gas constant, T is the temperature. Even without knowing A, E_a can be evaluated from the variation in reaction rate coefficients as a function of temperature.

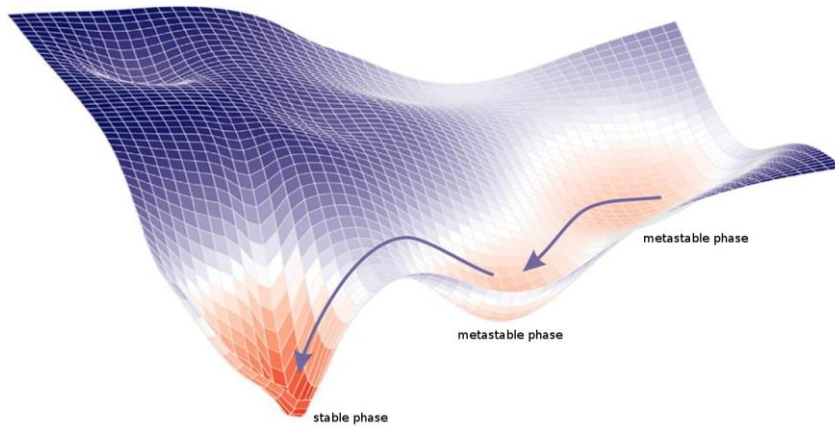


Figure 1: 3D representation of the Gibbs free energy surface. Metastable and stable phases are depicted, corresponding to local and global minima, respectively.[10]

Macroscopically, the structural phase transition is usually accompanied by substantial changes in various physical and chemical properties of the system. While using computer simulations to study these transitions, the unit cell of the crystal undergoes a considerable change. Therefore, simulating such processes should take into account such unit-cell modifications (constant-volume molecular dynamics are not suitable for simulations of solid-solid transitions). Instead, the constant pressure MD should be used, allowing the simulation box to change both its size and shape[10].

1.3 Aluminum Oxide and its phase structures

Metal oxides and especially aluminum ones are among the most abundant components of earth's crust and play a crucial role, e.g., in environmental chemistry, material sciences, and (photo)catalysis[11]. Out of this huge class, effort has been devoted to aluminas in its different forms[12][13].

Alumina, also called aluminum oxide, is a white, odorless and inert material which is considered as an electric insulator. It is also known for its strength and hardness with relatively high thermal conductivity with a melting point of 2320 °C[14]. It serves as the raw material for a broad range of advanced ceramic products and as an active agent in chemical processing. It is used for example as a catalyst support, in electronic-device fabrication[15], as a cutting-tool material, as a protective barrier against corrosion on alumina-forming alloys.

Alumina occurs in nature as a monocrystals called corundum. If they contain, intimately mixed, microcrystals of magnetite (Fe_3O_4) or hematite (Fe_2O_3), they are called emery. If the corundum monocrystals contain some elements in isomorphic substitution for Al^{3+} in their structure, gemstones and semi-precious gemstones are formed[16]. In the early days, aluminas heated at temperatures under 1100°C were considered as amorphous or non-crystalline materials (very ill defined). Later, it was recognized the presence of five crystalline aluminum hydroxides; they have crystals varying from micro to millimetric size. Stumpf et al [17] showed that, between the temperatures of dihydroxylation of aluminum oxide and α -alumina first crystallization, a number of well characterized intermediate crystalline alumina structures are formed; called later "transition aluminas" and received Greek letters to identify them: gamma, delta, theta, kappa, chi, eta and rho[16]. Therefore, the normal transformation from boehmite (γ - AlOOH) to α phase shall

go through γ, δ, θ phases and the transformation temperature for the final α phase is about 1200 °C[18]. A schematic of the most relevant paths in alumina phase transformations is reported by Igor et al.[19] in Figure 2. Transition alumina (especially γ) represent an important group of materials due to their very attractive and structural properties (fine particle size, high surface area and catalytic activity of their surfaces) making them a material of choice in a range of applicants such as catalysts, catalytic supports, adsorbents, hard protective coatings, abrasives, or membrane[20].

The polymorphism of different metastable structures can be classified in terms of the oxygen sublattice structure and the distribution into this sublattice of aluminum ions in tetrahedral and octahedral interstitial sites. As already mentioned, in α -Al₂O₃, the oxygen sublattice is hexagonal-close-packed (hcp) structured with 2/3 of octahedral sites occupied with cations, while $\gamma, \delta, \eta, \theta$ have a face-centered cubic (fcc) arrangement of oxygen atoms and cations present in various proportions in both octahedral and tetrahedral sites[21]. The polymorph of θ -Al₂O₃ is understood as monoclinic when half of Al³⁺ ions are in octahedral and other half in tetrahedral sites. However, the situation is much more complex for the γ -alumina; its structure (commonly believed that it can be described as a defect cubic spinel) is still actively studied[20]. Krokidis et al. [22] found that the equilibrium structure of γ -alumina corresponds to a percentage of tetrahedral aluminum of about 25 – 30%, in agreement with NMR data. For a pure gamma alumina, the correct stoichiometry requires the introduction of vacancies in the spinel cation sites. Unfortunately, there is no agreement on the location of these vacancies which forms a huge debate[23].

Furthermore, the transition aluminas have similar diffraction patterns, low crystallinity, and small particle size[24]. All these factors in addition to the continuous nature of the transformation between the forms during heating has made it difficult to probe such fine and

irregular structures by traditional analytical techniques[25]. In addition, Samir et Al. [26] also studied the phase transformations from transition alumina $\gamma \rightarrow \delta \rightarrow \theta \rightarrow \alpha - \text{Al}_2\text{O}_3$ by in situ X-rays diffraction from the ambient to 1200 °C. It revealed the coexistence of various phase transformations during the heating cycle[26].

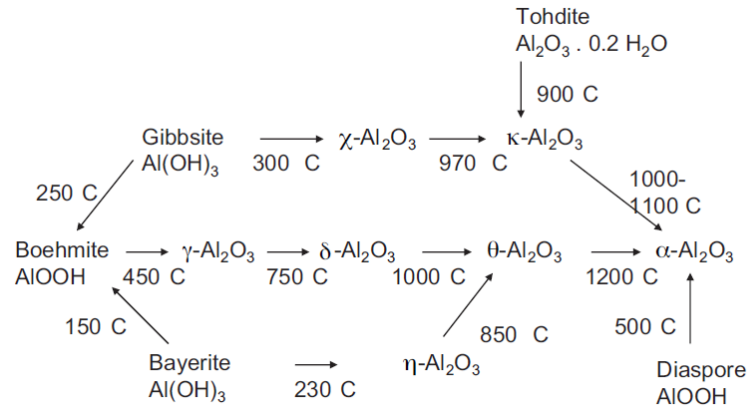


Figure 2: Schematic of the main phase transformations of aluminas upon heat treatment[19].

Boehmite has a very ordered structure of cation and anion sublattices with interstitial hydrogen, but as it is heated, dehydration (probably partial) occurs[24]. This process leaves vacancies in the crystal lattice that either stay vacant or become occupied by aluminum cations that shift their positions and coordination number. A previous theoretical study done by Krokidis et al.[22] showed that the aluminum atoms migrate from the octahedral to tetrahedral sites. This phase transition (because of the dehydration) creates structurally disordered metastable aluminas, with the γ form having the least ordered cation sublattice. As a result, γ is the least thermodynamically stable alumina form[24]. Upon heating gamma alumina, its cation sublattice becomes more ordered as the material undergoes a phase transition into δ and θ phases, resulting in increasing stability[24].

1.4 Aim of the research work

Many experimental studies have been done on phase transformations in alumina[26] mainly using X-ray diffraction patterns for their characterization. On the other side, atomistic details on the microscopic structure of some phases and the mechanisms of the transitions are still missing. In this work we, therefore, explore phase transitions between crystalline and amorphous phases of alumina using computational tools.

In Chapter 1, we (i) provide an overview of the computational methods used to do the calculations, reported throughout the thesis (ii) discuss the main aspects of Molecular Dynamics (MDs) and enhanced techniques. Then we describe tools used to characterize structures. Details and parameters used to perform the simulations are specified in Chapter 3. The techniques employed to build the unit cells of the different phase structures are introduced in Chapter 1. Finally, in the last two chapters (5 and 6), we present the results obtained.

Chapter 2 Methods

2.1 Introduction to Electronic Structure

Classical physics describes and explains many aspects of nature at an ordinary (macroscopic) scale. As technological improvements allowed scientists to probe the microscopic world in more detail, it became obvious by around the 1920s that very small pieces of matter follow a different set of rules from those we observe for large objects. Matter begins to behave very strangely, especially with evidence indicating that light and matter both have wave and particle characteristics at the atomic and subatomic level. Louis-Victor de Broglie proposed in his doctoral thesis that matter and radiation have both particle and wavelike behavior. On the other hand, Werner Heisenberg considered the limits of how accurately we can measure properties of an electron or other microscopic particles and proposed what we now call the Heisenberg uncertainty principle: It is fundamentally impossible to determine simultaneously and exactly both the momentum and the position of a particle. This principle, that can be shown to be a consequence of wave-particle duality, can be considered as the heart of what distinguishes quantum theory from classical mechanics.

In 1926, an Australian physicist, Erwin Schrödinger (Nobel Prize in Physics, 1933), developed wave mechanics, a mathematical technique that describes the relationship between the motion of a particle that exhibits wavelike properties (such as an electron) and its allowed energies. He set up the most fundamental equation in quantum mechanics, the Schrodinger's equation. The solution of this equation, called the wavefunction, determines all particle properties.

2.2 The Schrodinger Equation

Using Quantum mechanics, the N body system is not described anymore as point particles, but particles will be described using the wavefunction $\Psi(\vec{r}, t)$ which contains all the information

about all particles of the system. In addition, positions are no longer defined but instead a distribution function described as the modulus squared of the wavefunction $|\Psi(\vec{r}, t)|^2$ determines the probability density of finding a particle in a specific point in space. The time evolution of the quantum system is described through the general time-dependent Schrödinger equation as following:

$$H\Psi = i\hbar \frac{\delta\Psi}{\delta t} \quad (2)$$

Where Ψ is the wave function, \hbar is the Planck constant divided by 2π [27] and H is the Hamiltonian operator acting on the wavefunction. On the other hand stationary state might be described by the time-independent Schrödinger equation:

$$H\Psi = E\Psi \quad (3)$$

In the stationary state, the Hamiltonian is not dependent on the time explicitly and corresponds to the total energy of the system (sum of potential and kinetic energy operators).

Since there is no analytical solution to the Schrödinger equation for multiple nuclei and electrons, Max Born and J. Robert Oppenheimer proposed to simplify the problem by decoupling the motion of the atomic nuclei from the motion of the electrons. The electrons can be assumed to adapt to the state of the atomic nuclei instantaneously when the velocities of the nucleus are small compared to that of electrons. As a result, the total wave function Ψ of the complete system can be written as a product of the time-dependent wave function of the atomic nuclei Ψ_N and the time-independent electron wave function Ψ_e

$$\Psi(\mathbf{R}, \mathbf{r}, t) = \Psi_n(\mathbf{R}, t) \Psi_e(\mathbf{r}, \mathbf{R}) \quad (4)$$

where $\mathbf{R} = (R_1, R_2, R_3, \dots, R_N)$ and $\mathbf{r} = (r_1, r_2, r_3, \dots, r_K)$ are the coordinates of the N nuclei and the K electron, respectively. The wave function Ψ_e of the electronic subsystem depends parametrically only on the coordinates \mathbf{R} and not on the velocity V_R of the nuclei. Thus, the electronic

wavefunction can be computed by solving a time-independent Schrodinger equation for a given fixed nuclei position R [27]:

$$H_e(R) \Psi_e(r, R) = E_e(R) \Psi_e(r, R) \quad (5)$$

$$(T_n + E_e(R))\Psi_n(R, t) = i\hbar \frac{\delta\Psi_n(R, t)}{\delta t} \quad (6)$$

The Born-Oppenheimer approximation is valid usually for molecules in the ground state, as long as the electronic eigenvalues E_e (representing the potential energy surface) are not overlapping.

It is not possible to solve the Schrodinger equation analytically for a many-body system, therefore many approximations are made to solve the ground state electronic structure problem to reasonable accuracy. Some important types of modern calculations are Hartree-Fock (HF), configuration interaction (CI), coupled cluster (CC), Moller-Plesset (MP) perturbation theory and Density Functional Theory (DFT). Each of these approaches have certain accuracy and computational power consumption and one can be chosen depending on the required accuracy.

2.3 Molecular Dynamics (MD) Simulations

2.3.1 Introduction to computer Simulations

We carry out computer simulations in the aim of understanding the properties of assemblies of particles. The two main families of molecular simulation techniques are the molecular Dynamics (MD) and Monte Carlo (MC)[28], in addition to other hybrid techniques which combine features from both. The objective of MC simulation is to generate an ensemble of representative configurations under specific thermodynamics conditions for a complex system by applying random perturbations to the system. MC simulations do not provide information about time evolution, unlike MD which studies the temporal evolution of the coordinates and momenta (the

state) of a given structure[29]. Such an evolution is called the trajectory. Therefore, the main advantage of MD on MC is that it allows to compute the dynamical properties of the system: transport coefficients, time-dependent responses to perturbations, rheological properties and spectra.

Computing the dynamical properties and the trajectory of a many-body system is a challenging task, and no analytical solution is generally available both for classical and quantum dynamics. The only method that is proved to overcome this limitation is the numeral simulation. This kind of simulation has applications in a wide range of physics and chemistry fields, from simulating the galaxies we live in down to the molecules and atoms we are made of.

MD simulations have become much more powerful and accessible over the past few years. Until recently, MD required a supercomputer in order to perform most high-impact work. The present generation of computers takes advantage of parallelism and accelerators to speed-up the process. The most popular simulation codes (VASP[30], Abinit[31], AMBER[32], CHARMM[33], GROMACS[34], or NAMD[35]) have long been compatible with the messaging passing interface (MPI). When a large number of computer cores can be used simultaneously, MPI can greatly reduce the computation time.

2.3.2 Principle of MD

The molecular dynamics (MD) method consists of the numerical, step by step, solution of the classical equation of motion for nuclei. It was first introduced by Alder and Wainwright in the late 1950's [36] in their study of the interaction of hard spheres. The first MD simulation of a protein was performed in the late 1970's by McCammon [37], and the groundwork that enabled these simulations was among the achievements mentioned in the 2013 Nobel Prize in chemistry[38]. It is a widely used computational biophysics method which efficiently provides

insight into many biochemical processes at an atomistic level (structure-property relations, mechanism, dynamical, thermodynamical properties).

The principle of MD is based on the notion that Newton’s second law of motion is valid even at the atomic scale, apart from some exceptions including hydrogen tunneling. The trajectories are determined by solving numerically Newton’s equations of motion for a system of interacting particles. The input that is necessary are the atom initial positions, velocities, masses, a model representing the forces acting between the particles, and the definition of boundary conditions to be employed. Forces come either from electronic structure calculations (See Section 2.2) or using the empirical force fields. MD is a deterministic way to simulate the movement of the atoms. The classical equation of motion to solve is the following:

$$m_i \frac{d^2 r_i}{dt^2} = f_i = - \frac{\partial}{\partial r_i} U (r_1, r_2, \dots, r_N) \quad (7)$$

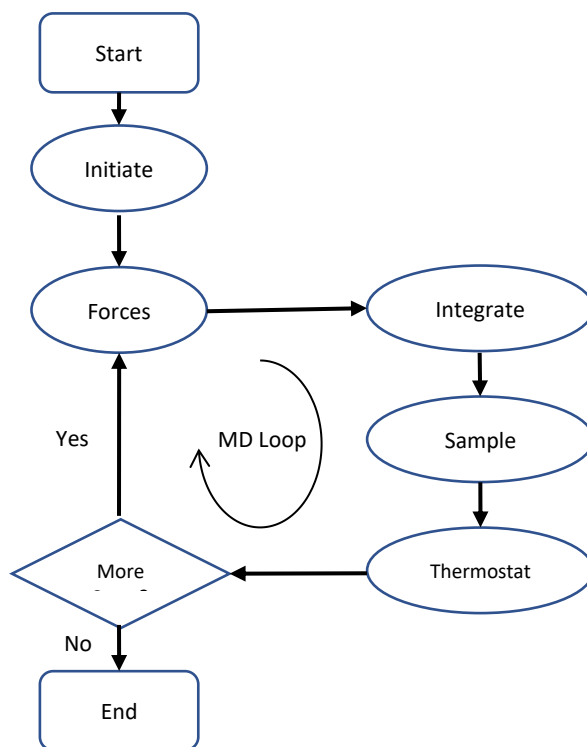


Figure 3: The basic Molecular Dynamics loop

where $U(r_1, r_2, \dots, r_N)$ is the potential energy depending on the coordinates of the N particles. This is a system of N coupled second order nonlinear differential equations that cannot be solved exactly, so equation (7) must be solved numerically step by step using an appropriate integration algorithm (e.g. Velocity Verlet Algorithm[39]) to obtain new positions and velocities. This is iterated to the end of the simulation. During the simulation system's properties can be calculated from the positions and velocities.

2.3.3 Classical MD

As explained in Section 2.2, approximations are made to solve the electronic structure problem and obtain the ground state energy. When the number of electrons in the simulation cell is large, the calculation of electronic energies, by the solution of the time-independent Schrödinger equation for electrons, is prohibitive and a reasonable approximation is Classical Molecular Dynamics. Classical MD is fast, at least in comparison with ab initio molecular dynamics (electronic structure calculations for evaluation of the forces). Large systems can be simulated in the order of billions of atoms; hence it is possible to simulate for example heat transport. Long simulation time (up to hundreds nanoseconds) can also be achieved, and processes that take a relatively long time to manifest, e.g. diffusion, can be studied[40].

In a classical MD simulation, all degrees of freedom of the electrons are disregarded, as well as quantum effects due the ions, so classical MD deals only with the motion of atomic nuclei under the effect of a parametrized potential. Forces are calculated from the parameterized potential, either fitted to empirical data or to first principles calculations. Specifically, forces are computed as the gradient of the parametrized potential (i.e., the force field).

$$\vec{F} = -\vec{\nabla}V(\mathbf{R}) \tag{8}$$

2.3.4 Force Fields

Potentials used in chemistry are generally called “forcefields”, while those used in material physics are called “analytical potentials”.

The force field (FF) is a mathematical expression describing the dependence of the energy of a system on the coordinates of its particles. It consists of an analytical form of the interatomic potential energy $U(r_1, r_2, \dots, r_N)$, and a set of parameters included in this form that are obtained either from ab initio or semi-empirical quantum mechanical calculations or by fitting to experimental data such as neutron, X ray, NMR, IR, Raman and neutron spectroscopy, etc. Most force fields in chemistry are empirical and consist of a summation of forces coming from a “chemical” description of the interactions of atoms in molecules: chemical bonds, bond angles, dihedrals, non-bonding forces associated with van der Waals forces and electro-static forces. Ideally, it should be simple enough to be calculated quickly, but should be sufficient to fully describe the properties of interest of the system studied.

Figure 4 illustrates the main energy terms contributing to a force field $V(R)$. The bonded energy terms describe bond stretching (V_{bond}), angle bending (V_{angle}) and torsion around dihedral angles (V_{dih}). The non-bonding terms are the Van der Waals interactions (VdW), the repulsive Pauli potentials among electrons clouds and electrostatic (Coulombic - V_{Coul}) potentials.

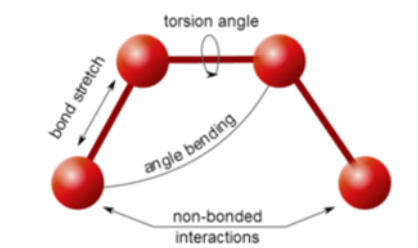


Figure 4: different types of potentials used for a force field

There are many FFs available in the literature, having different degrees of complexity, and oriented to treat different kinds of systems. In our work, the interactions between Al and O atoms are described by a Buckingham potential[41] in the original parametrization of Matsui[42]. This force field has shown to reproduce good experimental results such as a structure, density, bulk modulus, thermal expansion coefficient and melting temperature of Alumina[42].

2.3.4.1 Buckingham and Coulombic Potential[42]

The general form of Buckingham-electrostatic potential that models both the Short-range interactions between ions and long-range electrostatic interactions between the atoms is shown as below:

$$U_{ij}(r_{ij}) = A_{ij} \exp\left(\frac{-r_{ij}}{\rho_{ij}}\right) - \frac{C_{ij}}{r_{ij}^6} + \frac{1}{4\pi\epsilon_0} \frac{q_i q_j}{r_{ij}} \quad (9)$$

Where q_i and q_j are the charges of the ions i and j respectively, r_{ij} is distances between ions, ϵ_0 is the permittivity of free space and A_{ij} , ρ_{ij} , C_{ij} are the Buckingham potential parameters. The first and second terms represent the attractive van der Waal (vdW) and repulsive Pauli potentials, respectively, while the last term accounts for the long-range Coulombic interaction.

2.3.5 Long Range Electrostatic forces

The treatment of the long-range electrostatic contribution is a fundamental issue in molecular dynamics since it is the most expensive computational part of an MD simulation. Several methods have been developed for the treating of this contribution at affordable computational costs.

In this thesis, we have used a developed version of the Ewald summation method[43], called the Fast Smooth Particle-Mesh Ewald (SPME)[44][45]. Ewald summation rewrites the

potential as sum of short-range term whose sum quickly converges in real space and a long-range term whose sum quickly converges in the reciprocal space. In SPME, the direct space is similar to the Ewald sum, while the reciprocal part is performed using the 3D Fast Fourier Transform (3DFFT's).

2.3.6 Velocity Verlet Algorithm

First, as stated above, equation (7) can be solved numerically. So, we need to discretize the trajectory and use an integrator to propagate positions at discrete time intervals

$$r_i(t_0) \rightarrow r_i(t_0 + \Delta t) \rightarrow r_i(t_0 + 2\Delta t) \rightarrow \dots r_i(t_0 + n\Delta t) \quad (10)$$

Where r_i is the position of atom i and Δt is the time step. One common algorithm to integrate the Newton's equation of motion is the Verlet algorithm[46]. It is derived from a Tylor expansion of the positions in two different directions of time:

$$r(t + \delta t) = r(t) + \frac{dr(t)}{dt}\delta t + \frac{1}{2}\frac{d^2r(t)}{dt^2}\delta t^2 + \frac{1}{3!}\frac{d^3r(t)}{dt^3}\delta t^3 + O(\delta t^4) \quad (11)$$

$$r(t - \delta t) = r(t) - \frac{dr(t)}{dt}\delta t + \frac{1}{2}\frac{d^2r(t)}{dt^2}\delta t^2 - \frac{1}{3!}\frac{d^3r(t)}{dt^3}\delta t^3 + O(\delta t^4) \quad (12)$$

Adding up the two equations 11 and 12, we can get:

$$r(t + \delta t) = 2r(t) - r(t - \delta t) + \frac{d^2r(t)}{dt^2}\delta t^2 + O(\delta t^4) \quad (13)$$

The Verlet algorithm is simple and compact to code with good energy conservation (time-reversal symmetry). Unfortunately, the velocities play no part in the integration of the equations of motion and one needs to compute them as a separate step with a less accurate expression. It also requires the position as previous time ($t - \delta t$), which means that it is not self-starting.

An alternative version of the Verlet algorithm is the Velocity verlet algorithm[47] by incorporating explicitly the velocities.

The Velocity Verlet algorithm is one of the simplest algorithms and at the same time one of the best as it gives, compared to other integrators, a good long-time accuracy at the cost of a quite poor short time accuracy (shorter allowed time steps) and in addition its memory usage is smaller than the others. Based on a 2nd order Taylor expansion this algorithm can be used to calculate the positions and velocities of the atoms in a system. Starting at a time t with known positions, velocities and forces, we can propagate coordinates and velocities to time $t+\Delta t$. The positions and velocities are given by

$$r(t + \Delta t) = r(t) + v(t)\Delta t + \frac{f(t)}{2m} \Delta t^2 \quad (14)$$

$$v(t + \Delta t) = v(t) + \frac{f(t+\Delta t)+f(t)}{2m} \Delta t \quad (15)$$

With this method the velocities are calculated using updated positions at time $t+\Delta t$.

2.3.7 System Size and Periodic Boundary Conditions

The simulation of a macroscopic system is a hard challenge mainly because of its size, in fact the number of particles that come into play makes the treatment of this problem unfeasible even for the most powerful calculator available at present. A good solution is the use of a simulation box (or called a unit cell) with reasonable size and impose boundary conditions. We could use rigid walls, but then the surface effects would blur the real physics so using Periodic Boundary Conditions (PBC) is the most common choice for bulk properties. The PBC concept can be visualized as a primary cell surrounded by a set of replicas or image cells. Because the atoms in the image cell behave identically as those in the primary cell, it is immaterial to specify which space belongs to the primary cell and which belongs to the image cell. Therefore, the simulation box is surrounded by an infinite number of replicas of itself, as shown in Figure 5. Only the N atoms inside the main cell are considered explicitly, but as soon as one of the atoms leave the cell,

an image particle enters from the opposite side to replace it. The boundaries between the primary and image cell are only matter of imagination and can be drawn starting from any point in the system.

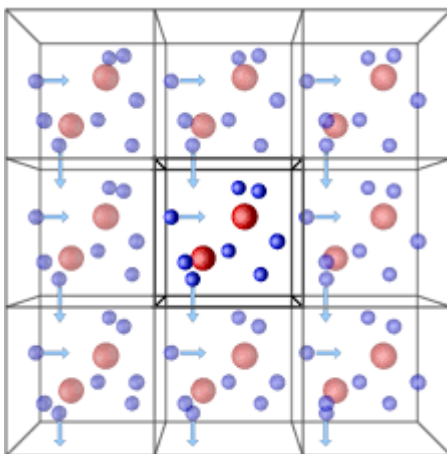


Figure 5: schematic representation of periodic boundary conditions in 3D, primary real cell located in the middle surrounded by the image cells

PBC are used together with the minimum image convention, meaning that only the interactions with the nearest image are considered.

2.3.8 Molecular Dynamics Ensembles

In general, an ensemble is a collection of all possible systems which have different molecular states but have an identical macroscopic or thermodynamic state. Therefore, ensembles are characterized by fixed values of thermodynamic variables.

There exist different ensembles with different characteristics: The basic ensemble for MD is the *NVE or micro-canonical ensemble* at which the volume and energy of the system is conserved at each step without any temperature or pressure control (isolated system occupying fixed volume). The constant-temperature, constant-volume ensemble (*NVT or canonical ensemble*) allows the control of temperature using a specific thermostat. In this case we have to

imagine the simulation box in thermal equilibrium with a heat bath. The *isothermal-isobaric or NPT ensemble* where the pressure and temperature are kept conserved using a barostat and thermostat at once. The change in the simulation cell can be isotropic where the cell shape remains unchanged or anisotropic where the cell shape changes.

2.3.9 Molecular Dynamics limitations

The power of molecular dynamics simulations is still limited by two main challenges. The first one is the computer power: simulations lengths greater than a microsecond are normally prohibitive. The second limitation concerns the classical MD: the empirical force field cannot provide any information about the electronic structure, therefore they are unable, in most cases, to handle electron excitations, charge transfers, etc. Furthermore, their predictive power is limited, as they can be applied only to systems containing the functional groups included in the development of the FF and their accuracy depends on the quality of its parametrization. This is the reason why any simulation should be validated by an appropriate comparison with experimental results.[48]

2.3.10 Enhanced Molecular Dynamics

One of the methods to overcome the timescale limitation of MD is accelerated molecular dynamics[49][50]. When the kinetic barriers are too large to allow an efficient exploration of the configuration space within typical MD timescales, the properties computed from the trajectory cannot be compared to experiments. For this reason, in order to study important biological activities (such as protein-protein association/dissociation) and phase transitions[51], one might need enhanced sampling[49][50] rather than straight unbiased MD.

2.3.10.1 Metadynamics

Metadynamics[52] is a powerful technique for enhancing sampling in molecular dynamics simulations and reconstructing the free-energy surface as a function of few selected degrees of freedom, often referred to as collective variables (CVs). In metadynamics, sampling is accelerated by a history-dependent bias potential, which is adaptively constructed in the space of the CVs, to force the system to leave local minima and thus sample low-probability states.

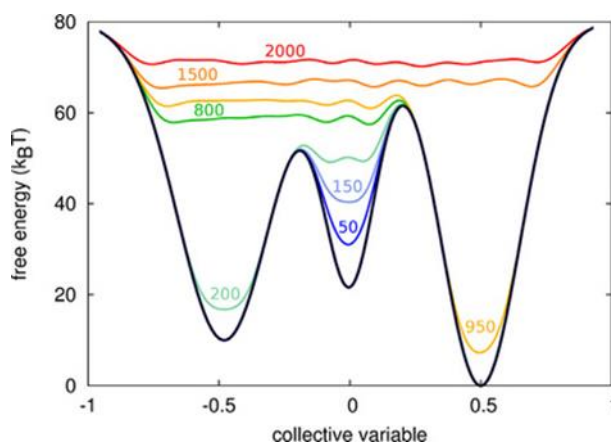


Figure 6: example of metadynamics simulations: the free energy landscape (black line) is traced as a function of a collective variable, together with the sum of the landscape plus the bias potential at different times (colored lines)

2.3.10.2 Collective Variables

Metadynamics techniques rely heavily on a good choice of the reaction coordinate which is the order parameter that describes a reversible path from reactants to products. Finding a good reaction coordinate poses one of the most challenging problems in many applications, especially when they are concerned with complex transformations involving a large number of degrees of freedom.

Designing a collective variable (CV) able to describe a transformation process, i.e., to match the reaction (or transformation) coordinate, means reducing the great number of degrees of

freedom into a few parameters. Metadynamics requires one or more CV to define the space in which the biased potential is applied.

The most general definition of a collective variable ξ is as a differentiable function of the vector of $3N$ atomic Cartesian coordinates, X :

$$\xi(X) = \xi(x_1, x_2, \dots, x_N) \quad (16)$$

Depending on the structure of the system, $\xi(X)$ is often a function of much fewer arguments than $3N$, or can be expressed as a combination of such functions[53]:

$$\xi(X) = \xi(z^{(1)}(X), z^{(2)}(X), \dots, z^{(\alpha)}(X) \dots) \quad (17)$$

with the number of basis function $z^{(\alpha)}$ much smaller than the number of atoms. We refer to $z^{(\alpha)}(X)$ as a colvar component: in the simpler and most common scenario, a single component z is identified with the colvar ξ . These elementary functions can be distances, angles or dihedrals mathematical definitions. More recently functions to describe also many body interactions or topological descriptors are also used.[53]

A good CV should be a dynamically relevant measure for the progress of a reaction. This means being able to distinguish among the different metastable states for the free energy landscape and the transition state. When possible, the number of CVs should be kept low because of the computational cost and the difficulty to deal with high dimensional spaces.

2.3.10.3 Path-PIV CV:

Describing phase transitions involving disordered systems, like amorphous phases or liquids, is a very complex task. Recently, a general CV scheme, the Path-PIV CV[54], has been proven to succeed in describing transitions in water and we are using them in this work to study transitions in alumina.

The Path-PIV CVs depend on the distances between different configurations of the system that are derived from relative atomic positions and, in its simpler construction, it requires only the initial and final guessed states of the transformation without any information about the pathway. The transformation is represented in the two-dimensional space $\{s,z\}$ of the path CVs with s quantifying the progress of the transformation and z discriminating between different pathways. Considering a system of N atoms in Cartesian space, $R \equiv \{R_i\}_{i=1,N}$ where R_i is the three-dimensional position vector of atom i , the configurations A and B of the system are derived from the interatomic Cartesian distances R^A (and similarly R^B) which defines a vector v^A of $\frac{1}{2}N(N-1)$ components called the permutation invariant vector PIV[55]:

$$v^A = \text{sort}(C_{ij}) = \text{sort}\left(C(|R_i^A - R_j^A|)\right), i > j \quad (18)$$

Where C_{ij} is a Fermi-Dirac-like function monotonically decreasing from one to zero in a chosen interval $R_{min} < |R_i^A - R_j^A| < R_{max}$. C_{ij} has the purpose of focusing the metric on the range of distances which are relevant for the physico-chemical process studied. The distances between the desired configurations M and N are computed as square Euclidean distances between the corresponding PIVs ($D_{MN} = \sum(v^M - v^N)^2$), and used to map each configuration M into a point of coordinates s and z in the 2D space that is defined by path CVs, built from the initial state A and final state B of the transformation:

$$s_M = \frac{1 \times e^{-\lambda D_{AM}} + 2 \times e^{-\lambda D_{BM}}}{e^{-\lambda D_{AM}} + e^{-\lambda D_{BM}}} \quad (19)$$

$$z_M = -\lambda^{-1} \log(e^{-\lambda D_{AM}} + e^{-\lambda D_{BM}}) \quad (20)$$

The two coordinates describe the progress from A to B. The freedom given by the coordinate z allows the exploration of a wide energy landscape and maybe the formation of unexpected metastable structures other than the desired ones. The parameter λ can be chosen freely, but a value at $\lambda \approx 2.3/D_{AB}$ is generally used, in order to localize the free energy basins of

reference states A and B around $s \approx 1.1$ and $s \approx 1.9$ respectively and for smooth transformation pathways.

2.3.10.4 Umbrella Sampling and WHAM

Due to the fact that metadynamics doesn't converge easily for complex free energy landscapes and in order to calculate the free-energy difference, a combination of Umbrella Sampling technique and the WHAM approach is used.

In Umbrella Sampling technique[56], a bias is applied to the system to ensure efficient sampling along the whole reaction coordinate. This is aimed at obtaining an overlap between a number of separated simulations (called windows), and in each of them the system is confined in a region of configurational space as shown in Figure 7.

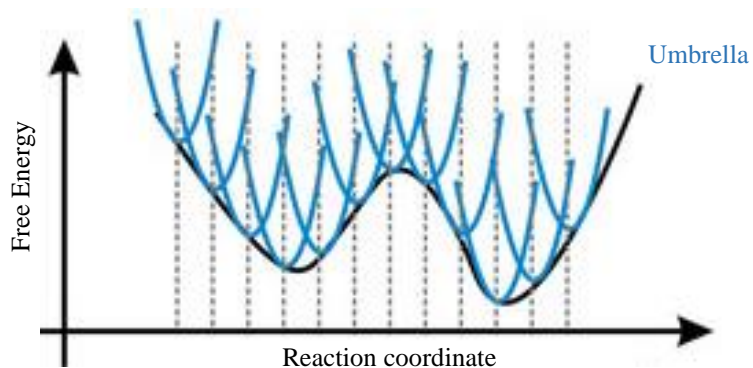


Figure 7: Free energy profile (black line) as function of reaction path sampled using distinct overlapping Umbrella windows (blue parabolas)

The method that allows the calculation of the free energy from the US simulations is weighted histogram analysis method (WHAM)[57] proposed by Kumar et al.[58]. WHAM is used to compute the Free Energy Surface (FES) of the reaction from the overlapping Umbrellas.

2.4 Analysis Methods

Different techniques can be used to distinguish between different structural phases of materials. We were able using the following methods below to have a good differentiation between the considered alumina phase structures.

2.4.1 Radial Distribution Functions and coordination numbers

The pair radial distribution function RDF is an important measure of the structure of condensed matter for several reasons. Radial distribution functions can be determined both experimentally and from simulation, allowing a direct comparison.

The RDF (referred to as $g(r)$) is the probability of finding a pair of atoms at a distance r apart relative to the probability for a completely uniform distribution. The RDF is strongly dependent on the structure of the system. At very short r , the RDF must be zero, because two particles cannot occupy the same space. For a uniform distribution of particles, $g(r)$ would be 1 for all r , therefore accumulation of particles shows up as $g(r) > 1$ and depletion as $g(r) < 1$. Finally, $g(r)$ tends to 1 at large r where the probability of finding a particle is almost 100%.

All the RDFs in this thesis are calculated using the GROMACS codebase, using the tool `gmx rdf`. RDFs are computed for each frame and then averaged along the simulation length.

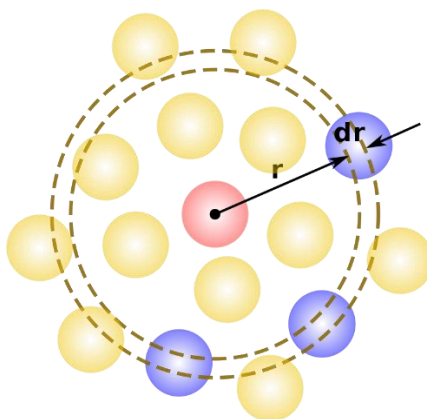


Figure 8: Scheme representing the strategy to calculate the RDF (dotted circular shell) of the reference atom in red by estimating the probability of the blue atoms within the circular shell.

On the other hand, the coordination number indicates how many molecules are found in the range of each coordination sphere. The coordination number can vary from values as low as 2 to as high as 16. The value depends on the relative sizes of the central atom and ligands or surrounding particles. The integration of RDF allows the determination of the number of neighbors around a central atom, so therefore, the integral to the first minimum gives the coordination number.

2.4.2 X-Ray Diffraction pattern

XRD analysis is a powerful technique to study crystal structures. It is used to identify the crystalline phases present in sample of a material. Identification of phases is achieved by comparison of the acquired data to that in reference databases. The powder pattern is considered a “fingerprint” for a given material as it provides information about the polymorph and crystallinity of the material.

All diffraction methods start with directing a monochromatic radiation of x-rays toward the sample. The interaction of these incident rays with the sample produces constructive

interference (and diffracted ray) when conditions satisfy Bragg's Law[59][60]. These diffracted X-rays are then detected, while scanning the sample through a range of incident angles.

2.4.3 Steinhardt's order parameters

In 1983, Steinhardt et al.[61] proposed the family of bond-orientational order parameters (SP) based on spherical harmonics to describe the local atomic environment. As a result, considering distributions of these order parameters across a system can help characterizing the overall system's ordering. It has become a standard tool in condensed matter physics, with applications on glass, jamming, melting or crystallization transitions, and cluster formation[62]. The idea is to express the arrangement of the nearest neighbors using spherical harmonic functions. Spherical harmonics are key functions for representing the angular correlations of a neighboring particle within a spherical cutoff. SP can be defined as :

$$q_{lm}(i) = \frac{1}{N(i)} \sum_{j=1}^{N(i)} Y_{lm}(\hat{r}_{ij}) \quad (21)$$

Where q_{lm} is the bond order parameter of particle i , Y_{lm} is the spherical harmonic function, $N(i)$ is the number of nearest neighbor particles around i , and \hat{r}_{ij} is the vector connecting i and j . However, it is important to construct rotationally invariant combinations of spherical harmonics to have order parameters independent of the alignment of the crystal[63].

l and m are both integers with $m \in [-l, +l]$ and l directly related to the symmetry of the spherical harmonics. The value of $l = 6$ is a good value for the detection of fcc and hcp – like structures, as the hexagonal planes in these crystal lattices have six-fold symmetry[64] and $l = 4$ is used to describe environments with 4 – fold symmetry. Therefore, our calculation focused mainly on two order parameters Q_4 and Q_6 in which are calculated with the help plumed plugin.

2.4.4 Mean square displacements

Mean square displacement MSD analysis is a technique commonly used to determine how large is the displacement of a particle in a time unit. It can help to determine whether the particle is freely diffusing, transported or bounded and limited in its movement. We have used the msd tool of GROMACS to compute all the MSD of atoms from sets of initial positions. This provides an easy way to compute the diffusion constant using the Einstein relation.

Chapter 3 Computational Details

3.1 Simulations Details

3.1.1 For classical Molecular Dynamics

Molecular Dynamics simulations were performed using GROMACS 2018.4[34] with the Buckingham[42] potential forcefield. The equations of motion were integrated with timestep of 1 fs. The electrostatic interactions were calculated by the fast-smooth Particle Mesh Ewald (SPME)[45] algorithm; direct space is similar to the Ewald sum, while the reciprocal part is performed with FFTs. A cutoff of 0.6 nm was used for short range, Vander Waals, and coulomb electrostatic interactions. The simulated system contains 960 atoms and the interaction is described using the Buckingham potential with parameters described in Table 1 parametrized by Steffen et al.[41].

The temperature control was achieved using velocity rescaling with a stochastic term. This thermostat is similar to the Berendsen coupling, but the stochastic term ensures that a proper canonical ensemble is generated. For pressure coupling in NPT simulation, we used the Berendsen barostat which means exponential relaxation pressure coupling with a time constant 0.2ps. The box is rescaled every timestep.

The biased metadynamics simulations were performed using the same version of GROMACS with PLUMED 2.6.0-dev plug-in [65]. We used potential walls for cell parameters in order to prevent cell over prolongation or expansion.

Table 1: potential parameters from Steffen et al.[41] The charges are $q_{Al} = 1.4175$ and $q_O = -0.945$.

	A_{ij} / eV	$\rho_{ij} / \text{\AA}$	$C_{ij} / \text{eV}\text{\AA}^6$
<i>Al-Al</i>	31570921.75	0.068	14.05
<i>Al-O</i>	28476.91	0.172	34.58
<i>O-O</i>	6462.67	0.276	85.09

3.1.2 Quantum simulations

The quantum simulations were done using cp2k 7.0 code. Electronic structure methods (DFT) were used to compute the forces with Gaussian and plane waves method. As of the classical MD, we simulated using NPT ensemble at 1 bar with flexible cell and a 2fs timestep. Temperature was controlled with a canonical sampling through velocity rescaling. Maximum number of SCF iteration to be performed for one optimization was 200 and number of multi grids used was 5 with cutoff 400 Ry.

The exchange and correlation potential is calculated using NO_SHORTCUT and PBE functionals in addition to the Pair potential van der Waals density functional as an additional dispersion corrections (Grimme D3 method with a cutoff of 16 Angstrom).

3.2 Codes Used

All the simulations done in this thesis are done on the Lille University cluster. Gromacs code was chosen to perform all the classical MD simulations (biased and unbiased) with the help of an open-source plugin called PLUMED. The DFT simulations we done using the cp2k code. Finally, trajectories are visualized using the VMD program.

3.2.1 GROMACS

The MD engine selected for this work is the molecular dynamics code GROMACS[34] version 2018.4. This is a highly efficient free and open-source toolkit used by many research groups all over the world, that provides extremely high performance compared to all other programs. It incorporates also the concept of domain decomposition, where the system is divided up into smaller units which are distributed to the different computational units.

GROMACS is a user-friendly, with topologies and parameter files written in a clear text format. There is a lot of consistency checking, and clear error messages are issued when something is wrong. There is no scripting language - all programs use a simple interface with command line options for input and output files. You can always get help on the options by using the **-h** option, or use the extensive manuals provided free of charge in electronic format.

3.2.2 PLUMED

Plumed[66] is a portable plugin that works with a large number of molecular dynamics codes. It can be used to analyze features of the dynamics on-the-fly or to perform a wide variety of free energy methods. It can also work as a command line tool to perform analysis on trajectories saved in most of the existing programs. The first version of Plumed was released in 2009 and there has been one more major release since. Here it is used as a plug-in to GROMACS code to perform the metadynamics simulations.

3.2.3 CP2K

CP2K[67] is an open source electronic structure and molecular dynamics software package to perform atomistic simulations of solid-state, liquid, molecular, and biological systems. It is written in Fortran programming language providing a general framework for different modeling

methods such as DFT using the mixed Gaussian and plane waves approaches GPW and GAPW. It supports a wide range of theory levels and classical forces fields with also different types of simulations.

3.2.4 VMD

VMD[68] or visual Molecular Dynamics is a molecular visualization program for displaying, animating, and analyzing molecular systems. The theoretical Biophysics group at the University of Illinois at Urbana, Champaign developed this open source code for public use[68]. VMD can simultaneously display any number of structures using a wide variety of rendering styles and coloring methods. VMD is written in C++ language, using an object-oriented design; the program, including source code and extensive documentation, is freely available for everyone.

Chapter 4 Crystallization of Gamma alumina

4.1 Preparation of structures

Here we present the procedures followed to prepare different structures (crystallized and amorphous at each temperature) to be used as the reference structures in the PathCV-PIV collective variable.

4.1.1 Reference structures preparation

This section will include the procedure of preparation of the reference structure simulation boxes needed to use the PathCV-PIV collective variable as detailed in section 2.3.10.3. We have considered two types of alumina phase transition structures (Gamma and Theta) in addition to the most stable one (thermally stable Alpha alumina). These 3 structures are considered the most popular and important due to their wide range of applications.

First, we took atomic positions files for each structure from literature. Alpha from W E Lee et al.[69], a Gamma model by Krokidis et al.[22] and Theta from Husson et al.[70]. Simulation boxes are built from supercells containing 960 atoms (384 Aluminum and 576 Oxygen atoms) each. After that, we performed energy minimization (steepest descent algorithm) with maximum step size of 0.01 nm and tolerance of 10 kJ/(mol.nm).

Consecutive molecular dynamics NPT simulations were run with increasing temperatures (500K, 1000K, 1500K, 1800K, and 2000K) starting from the energy minimum at 0K. After that, 50ns NPT simulations at each temperature are done to stabilize and equilibrate the systems. These simulations are used later to define the reference PathCV-PIV structures and calculate statistical properties.

4.1.2 Amorphous structures:

The amorphous state was prepared by starting with the alpha alumina structure at 0K. This initial configuration is heated (rate of 0.1K/ps) to 2800K, where the system is liquid, and thermalized for over 10ns. Then, the samples are cooled to the desired temperatures (rate of 0.1K/pas) and finally thermalized for over 100ns.

Changing the initial state of the amorphous preparation procedure or the rates (up to a 100% variation) did not result in a significant change in the RDF of the final obtained amorphous structure.

4.2 Crystallization of Gamma Alumina

In this section we show (i) the results regarding the crystallization of alpha and gamma alumina, (ii) an analysis of the gamma alumina crystallization mechanism (iii) the effect of temperature on free energy profiles and mechanisms.

4.2.1 Crystallization of Alpha Alumina

In order to study the crystallization process of alpha alumina we set up a metadynamics simulation at 1000K starting from the amorphous phase (the melting point is estimated to be at about 2200K) and specifying the alpha phase as the final reference structure. The PIV vectors are constructed using SF_2 for $PIV_{Aluminum-Aluminum}$ and SF_1 for the rest (the SFs are explained in details in section 5.1). The parameters used for the bias potential are as following: $\{\delta s = 0.03, \delta z = 2, h = 0.0062 \text{ Kcal/mol}\}$, added every 1000 steps. We remark that we don't give any information about the pathway to be followed, leaving the system free to visit stable structures that may be different from the reference ones.

Tracking the pathway followed by the system during this transformation in Figure 9, we see that it first escaped the amorphous region (Am at $s \sim 1.1$), reaching intermediate (meta)stable configuration (high z and $s \sim 1.4$) and finally ended up in the alpha alumina basin (α at $s \sim 1.9$). To obtain a representative structure for each region visited by the system we run standard MD simulations of at least 100ns length starting from an initial structure taken from the metadynamics simulation in the center of the basin (s, z space). The structures obtained are characterized in terms of Aluminum - Aluminum RDFs. In Figure 10, we compare RDF plots of our reference structures and structures obtained from the metadynamics showing that the state reached at $s \sim 1.9$ is the one corresponding to alpha alumina. Moreover, the Al - Al RDF of the intermediate state is almost

superimposable to the one of a gamma alumina model [22] suggesting that such a state is indeed the gamma alumina. This is also confirmed by a comparison between XRD spectra plotted in Figure 10, where we show the experimental XRD spectrum (A) of the commercial gamma alumina [71] and the ones computed on the reference gamma alumina (B) and the intermediate state (C). The two (common) main peaks around $2\theta \sim 46^\circ$ and 67° show that the intermediate structure is crystallized and the agreement with the experimental data validates our hypothesis. Finally, a good match in the distribution of Aluminum coordination numbers (around 1/3 with CN=4 and 2/3 with CN=6) between the crystallized and reference from literature.

The crystallization of alpha alumina at 1000K is then a two-steps process with the crystallization of gamma alumina being the first step. We analyze in detail the crystallization of gamma alumina in the next section.

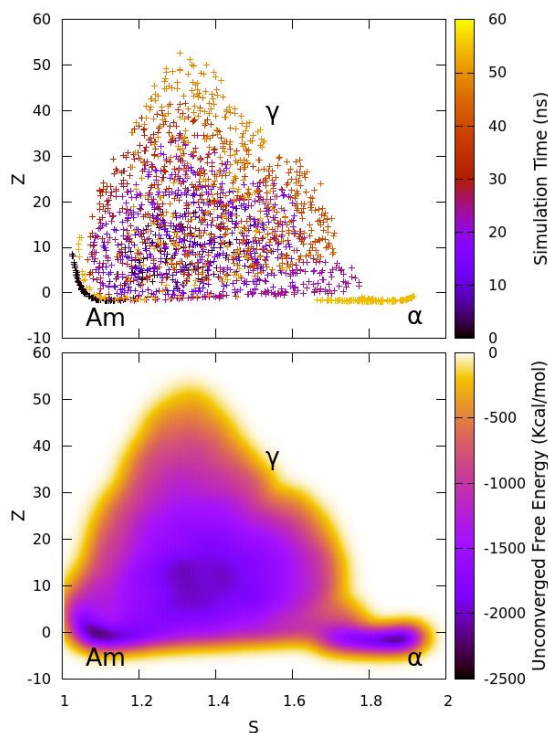


Figure 9: 3D graph showing the time progress and unconverged free energy of the metadynamics simulation starting from the amorphous structure (Am) to the alpha structure (α) passing by Gamma structure (γ) in the s - z space.

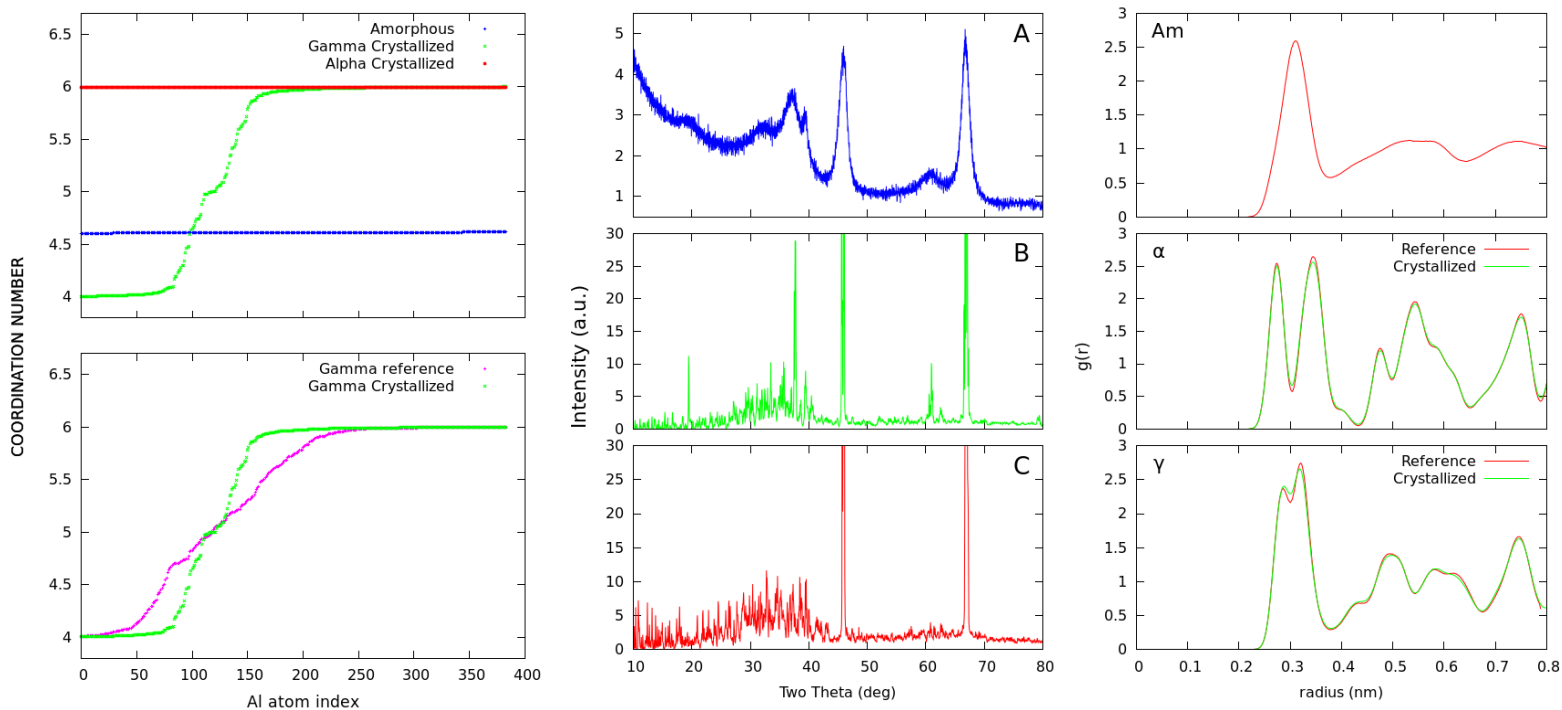


Figure 10: Comparison between partial Al-Al radial distribution functions calculated for Amorphous structure (Am), alpha alumina structure (α), and two gamma aluminas (the Reference and Crystallized Gamma obtained in this work). X-ray Diffraction pattern calculate for experimental gamma structure (A), the reference gamma from literature (B) [22] and the crystallized gamma structure (C). Coordination numbers of each Aluminum with all Oxygen atoms as function of Al atom index for amorphous, Alpha and Gamma (crystallized and reference from literature) structures.

4.2.2 Crystallization of Gamma Alumina

In order to better explore the transition between the amorphous and gamma structures we set up a second metadynamics simulation where we use the gamma phase as the final PIV reference (see Figures 14 and 17 for details). We used SF_1 for the PIV vectors and the bias potential $\{\delta s = 0.0087, \delta z = 0.2, h = 0.0062 \text{ Kcal/mol}\}$, added every 1000 steps. As in Figure 9 the metadynamics simulation draws a continuous path between the amorphous and the gamma phases but in this new PIV-PathCV space the gamma alumina is located in the at $s \sim 1.9$. The Free energy profile of the transformation as a function of the parameter “s”, computed by Umbrella Sampling, is shown in

Figure 11; two minima are found for the amorphous (Am) and gamma alumina (γ) phases respectively. The free energy barrier is about 0.2 Kcal/mol and the transition state is closer to the amorphous basin in the PIV-PathCV space. Bootstrapping errors [57] on the free-energy surface are on average 10^{-5} with a maximum value of 10^{-4} Kcal/mol.

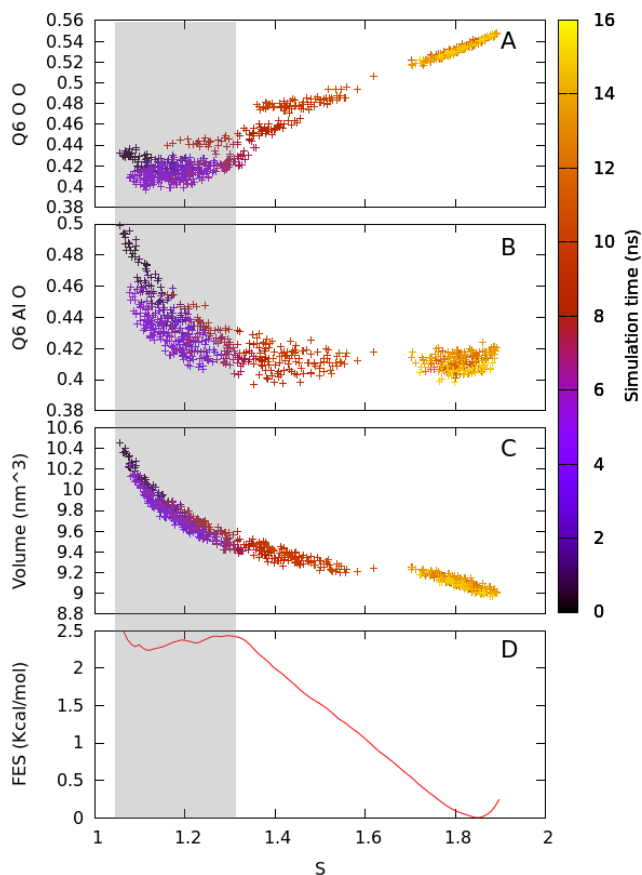


Figure 11: 3D graphs showing the convergence of the Q_6 [O - O] (A), Q_6 [Al - O] (B) and Volume (C) as function of time projected along the path collective variable S , alongside with the Free Energy Surface (D) of the transformation as a function of the same parameter. The shadowed region shows the initial basin on the left of the barrier.

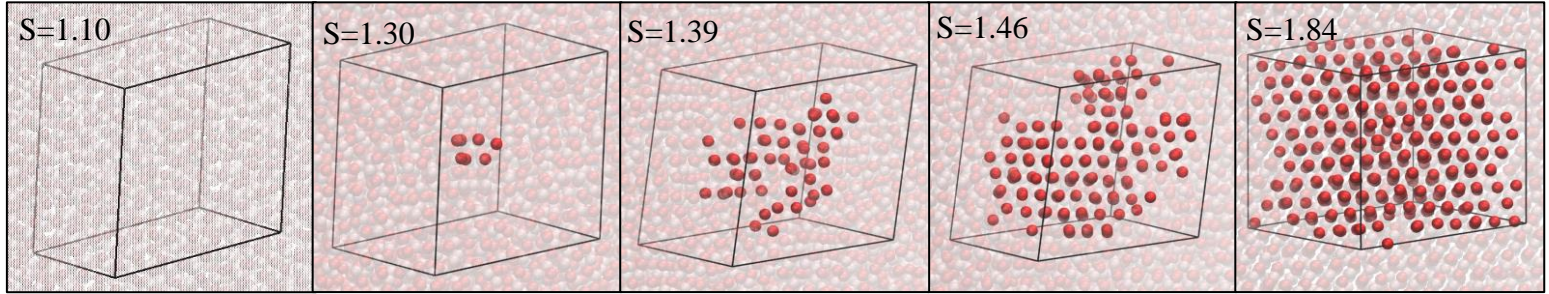


Figure 12: Sequence of snapshots of the umbrella sampling simulation describing the progressive crystallization of the amorphous phase into Gamma Alumina. Atoms in red are Oxygen atoms with a local Octahedral bond order parameter [61] higher than 0.5.

In Figure 11 we show the Steinhardt parameters (Q_4 and Q_6) and the cell volume as function of the s coordinate for the metadynamics simulation. Interestingly, figures 11-A, 11-B and 11-C show that as the system crosses the free energy barrier the Al - O reciprocal orientation changes together with the volume of the cell but the oxygen network remains disordered and rearranges only at a later time. Specifically, the volume of the cell decreases together with the number of the 6-coordinated (octahedral) Aluminum atoms. This is confirmed by the plots of the Steinhardt parameters as a function of time presented in Figure 13, and suggests that the transformation is induced by the increasing number of 4-coordinated (tetrahedral) Aluminum atoms to the detriment of 6-coordinated (octahedral) ones. The decrease of volume suggests that compressing the system could be a way to induce the transformation experimentally. As soon as the number of tetrahedrally coordinated Al atoms is sufficiently big, Oxygen atoms rearrange into an ordered face-centered-cubic network (fcc) through a nucleation process, as shown in Figure 12. This can be confirmed by the work of Hossein Eslami et al. [63] who has presented a full and accurate discriminate between liquid, fcc, hcp, and bcc phases using local order parameters. The perfect fcc crystalline structure is shown to have a combination of $Q_4 = 0.191$ and $Q_6 = 0.57$ (Table 2), while the crystallized Gamma structure reached by the system has an average of $Q_4 \text{ O - O} = 0.161$ and $Q_6 \text{ O - O} = 0.533$ (seen in Figure 13).

Table 2: The order parameters q_4 and q_6 for the perfect (nonthermalized) lattices[63].

Phase	Q_6	Q_4
bcc	0.511	0.036
hcp	0.484	0.097
fcc	0.575	0.191

The snapshots of the nucleation process shown in Figure 12 show that at 1000K the size of the critical nucleus ($s \approx 1.3$) is about a tenth of atoms. Once such a nucleus is formed the crystallization proceeds spontaneously till the formation of a fully crystalline box at $s = 1.84$.

In fact, the ordering process of Oxygen atoms can be achieved spontaneously using normal MD simulation (0.2ns) starting from a configuration just on the right of the free energy barrier ($s = 1.4$). Therefore, the position of the transition state is validated in the CV space. We stress here that the possibility of describing the energetics and the structure of the transition state is a general achievement of the method that is not limited to the application to a crystallization phenomenon.

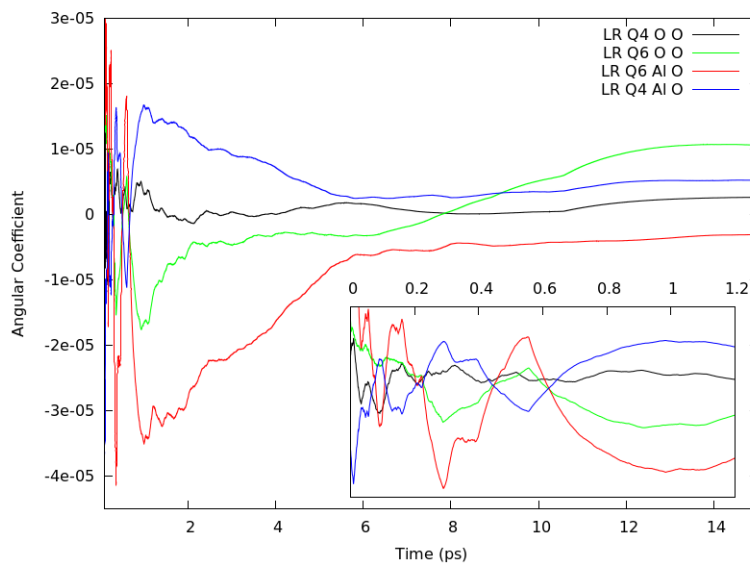
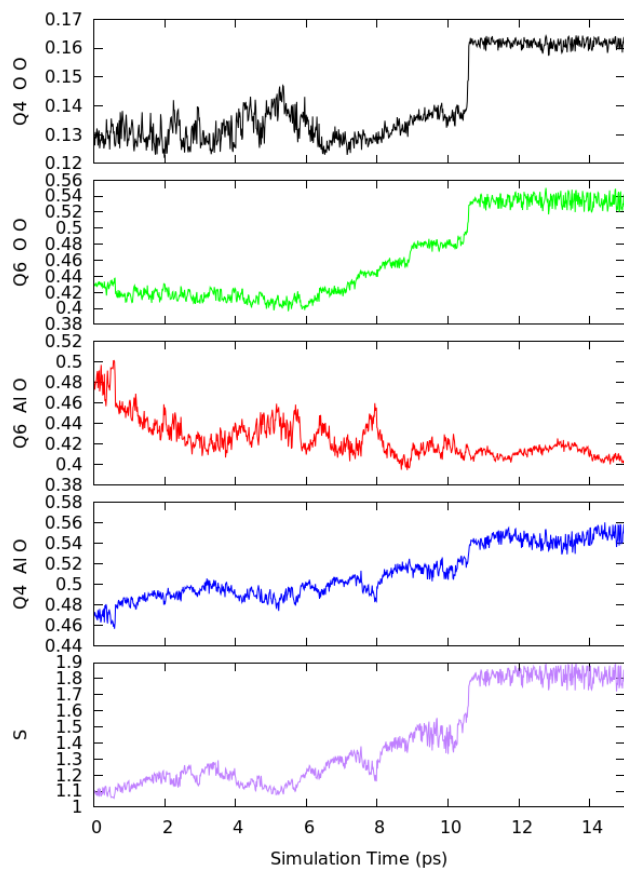


Figure 13: A) Steinhardt parameters Q_6 [O - O], Q_6 [Al - O], Q_4 [Al - O] and the coordinate “s” as a function of time during the metadynamics. B) Angular coefficient of the linear interpolation of the different plots (in A) done on an increasing set of (time ordered) points along the metadynamics.

In the next subsection we analyze the effect of temperature on the gamma alumina crystallization energetics and mechanism.

4.2.3 Temperature dependence

In order to check the effect of temperature on gamma alumina crystallization we run five additional metadynamics simulations at 800K, 900K, 1500K, 1800K and 2000K. All simulations reach a “gamma” state and the Free Energy profiles along the variable “s” together with the RDF of the initial and final snapshots are shown in Figures 16 and 19.

At low temperature (800-1000K) the free energy difference between the gamma and the amorphous phases decreases as a function of temperature (and so does the free energy barrier), crossing the zero between 800K and 900K (see Figure 16). This behavior is kept up to 1500K where the amorphous transforms into gamma during a classic MD (very low barrier) and with the same mechanism found at 800K, 900K and 1000K, more details are given in Figure 13.

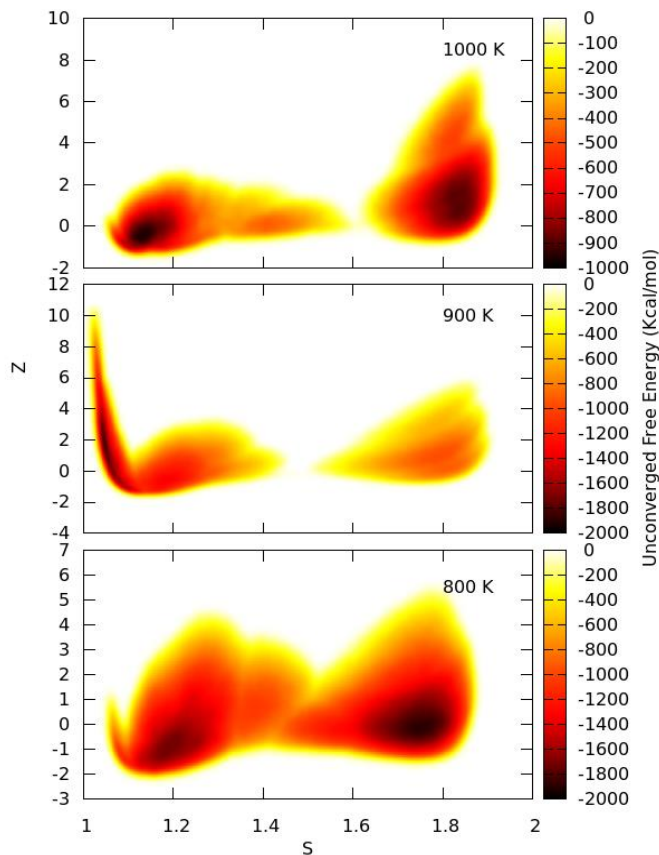


Figure 14: 3D graph showing the unconverged free energy of the metadynamics simulations starting from the amorphous structure (around $s \sim 1.1$) to the gamma structure (around $s \sim 1.9$) in the s - z space at low temperatures.

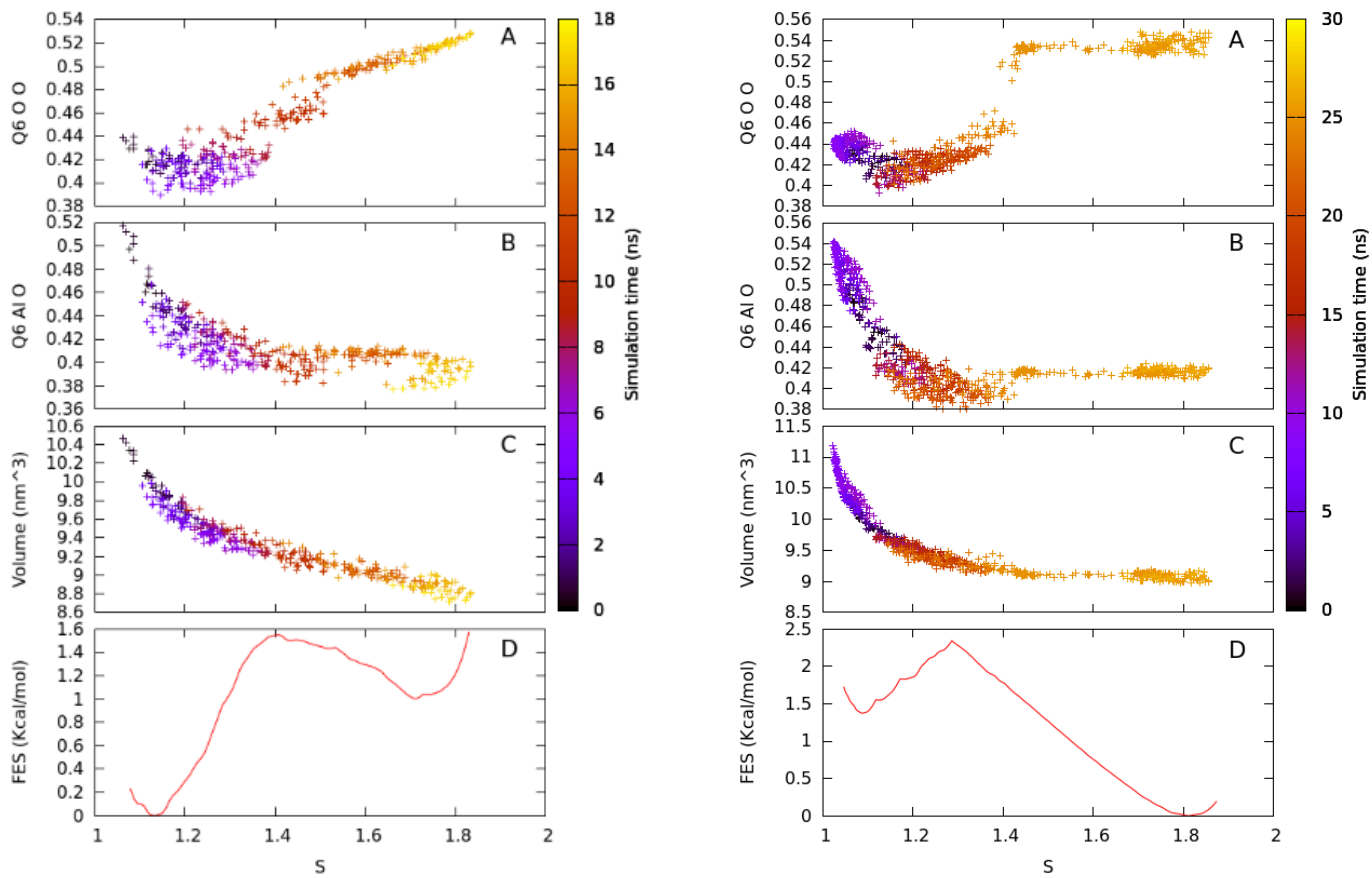


Figure 15: 3D graphs showing the Steinhardt parameter $Q_6 [O - O]$ (A), $Q_6 [Al - O]$ (B) and Volume (C) as function of time projected along the path collective variable S , alongside with the Free Energy Surface (D) of the transformation as a function of the same parameter s at 800 and 900K respectively.

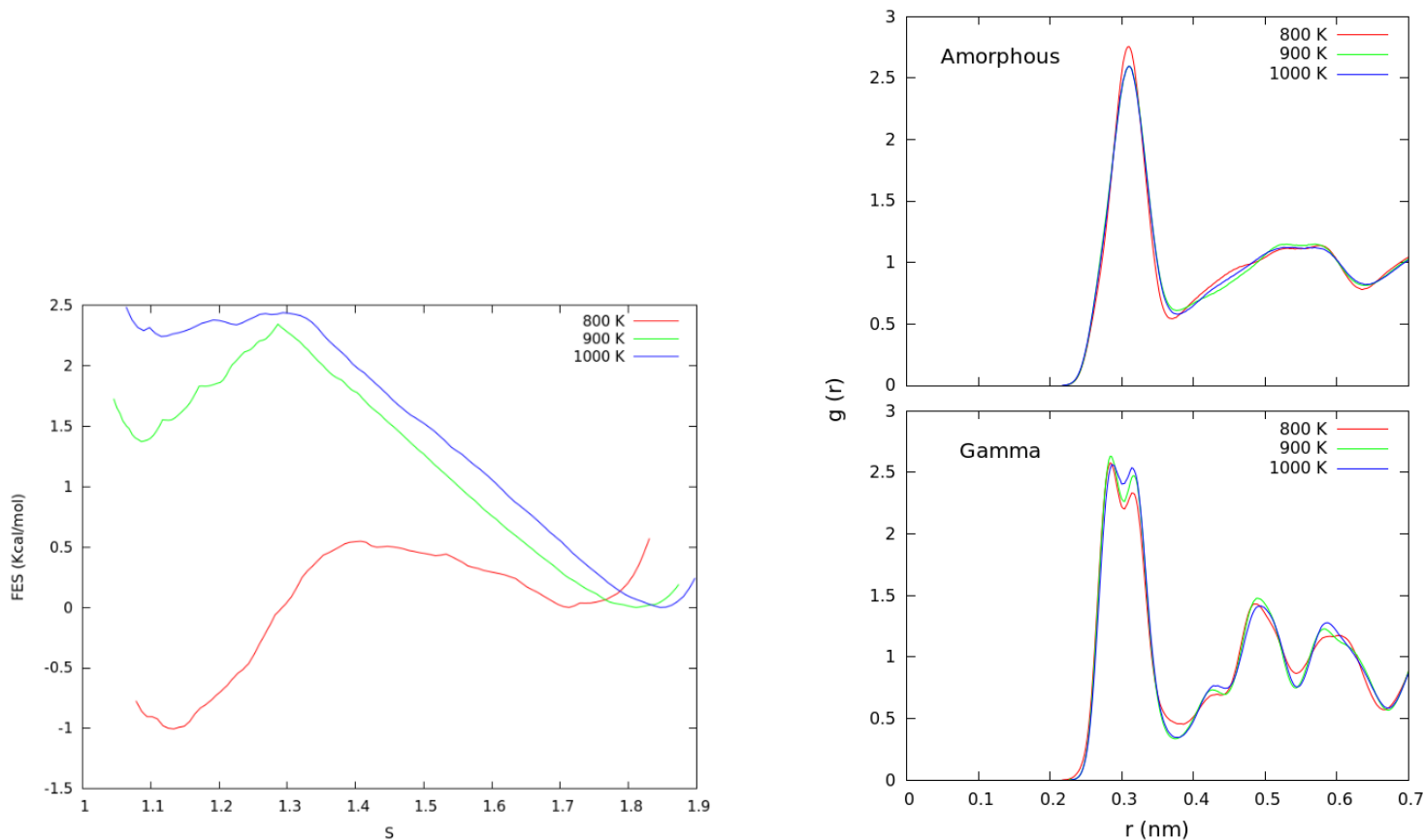


Figure 16: Free Energy Profiles for the amorphous-gamma transformation (left) and RDFs of the initial and final state at low temperatures (800 - 1000K).

At high temperature (1500K - 2000K) the free energy difference and the barrier increase as a function of temperature, as shown in Figure 19. We remark that at 1800K ions start to diffuse, as shown by the Mean Square Displacement (MSD) plots in Figure 20, and the behavior of the disordered system (initial state of the transformation) is closer to a liquid. Nevertheless, the mechanism of the transformation is similar to what we find at 1000K and only changes at 2000K, where the MSD has a dramatic increase (see Figure 20).

Moreover, we note that at high temperature the position of the barrier changes as a function of temperature and moves towards the final state. Being this position connected with PIV distance from the initial state we find that the more the transition state is topologically different from the

initial state the higher is the energy difference between them. Such behavior is often found in organic chemical reactions and known as the Hammond postulate[72].

Bootstrapping errors on free energy barriers shown in figures 16 and 19 are of the order of 10^{-4} Kcal/mol.

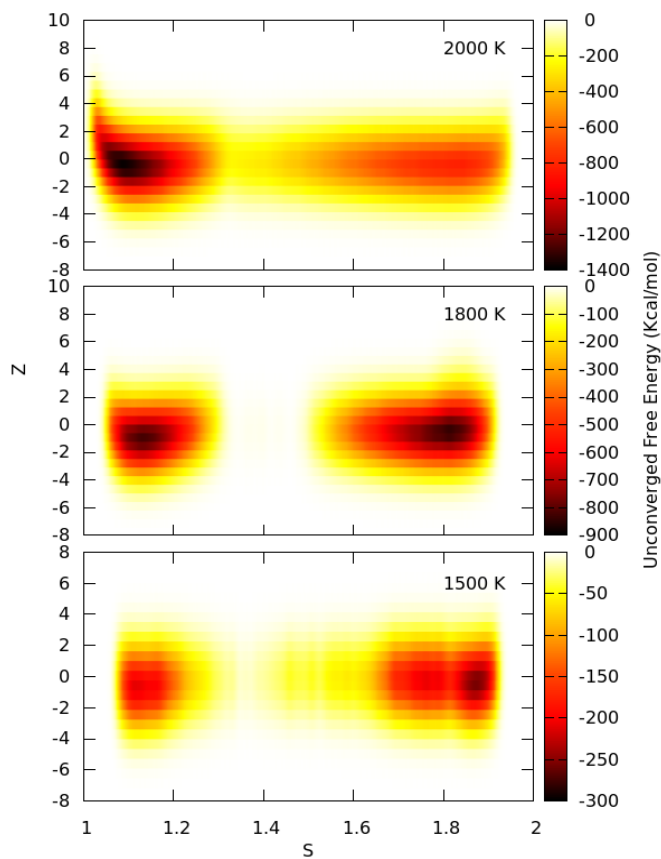


Figure 17: 3D graph showing the unconverged free energy of the metadynamics simulations starting from the amorphous structure (around $s \sim 1.1$) to the gamma structure (around $s \sim 1.9$) in the $s - z$ space at high temperatures.

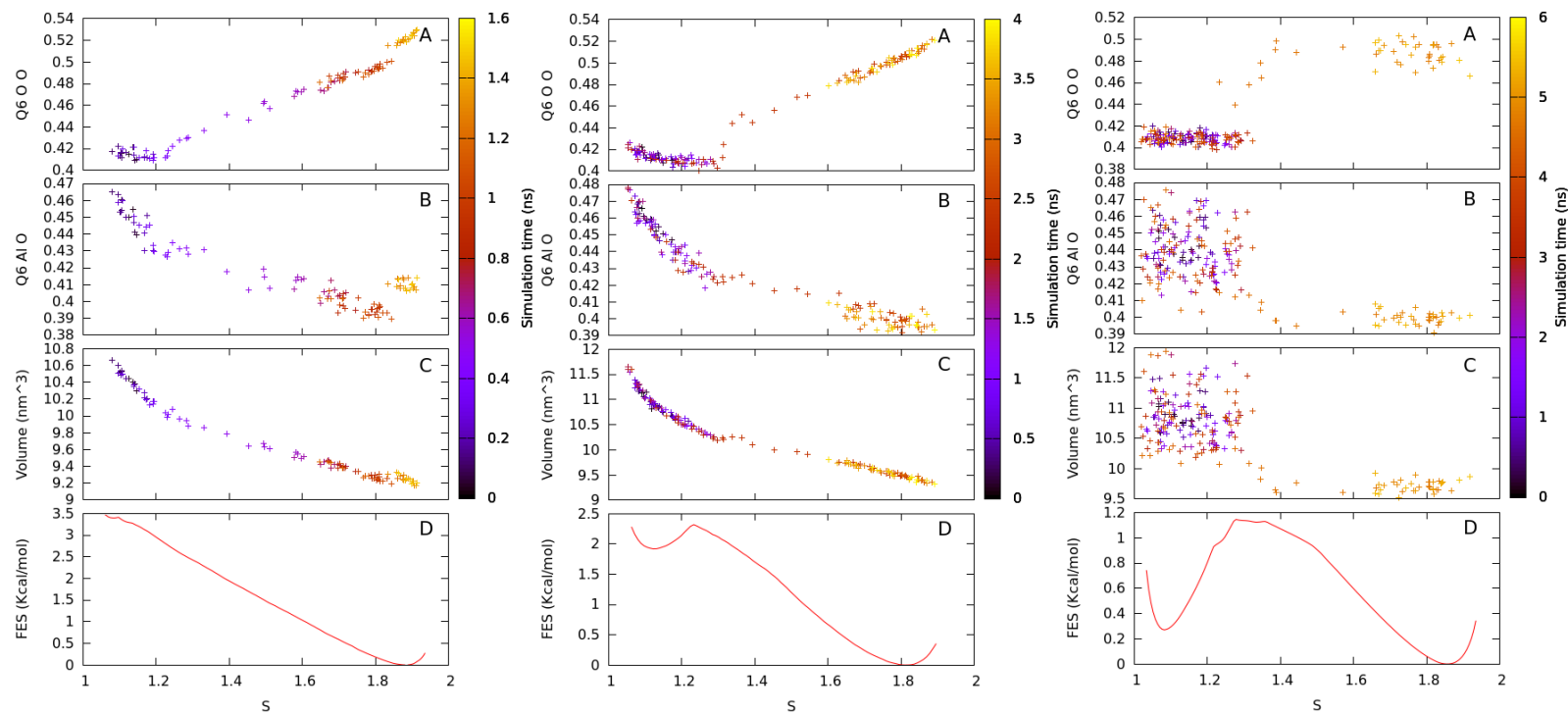


Figure 18: 3D graphs showing the Steinhardt parameter $Q_6 [O - O]$ (A), $Q_6 [Al - O]$ (B) and Volume (C) as function of time projected along the path collective variable s , alongside with the Free Energy Surface (D) of the transformation as a function of the same parameter s at 800 and 900K respectively.

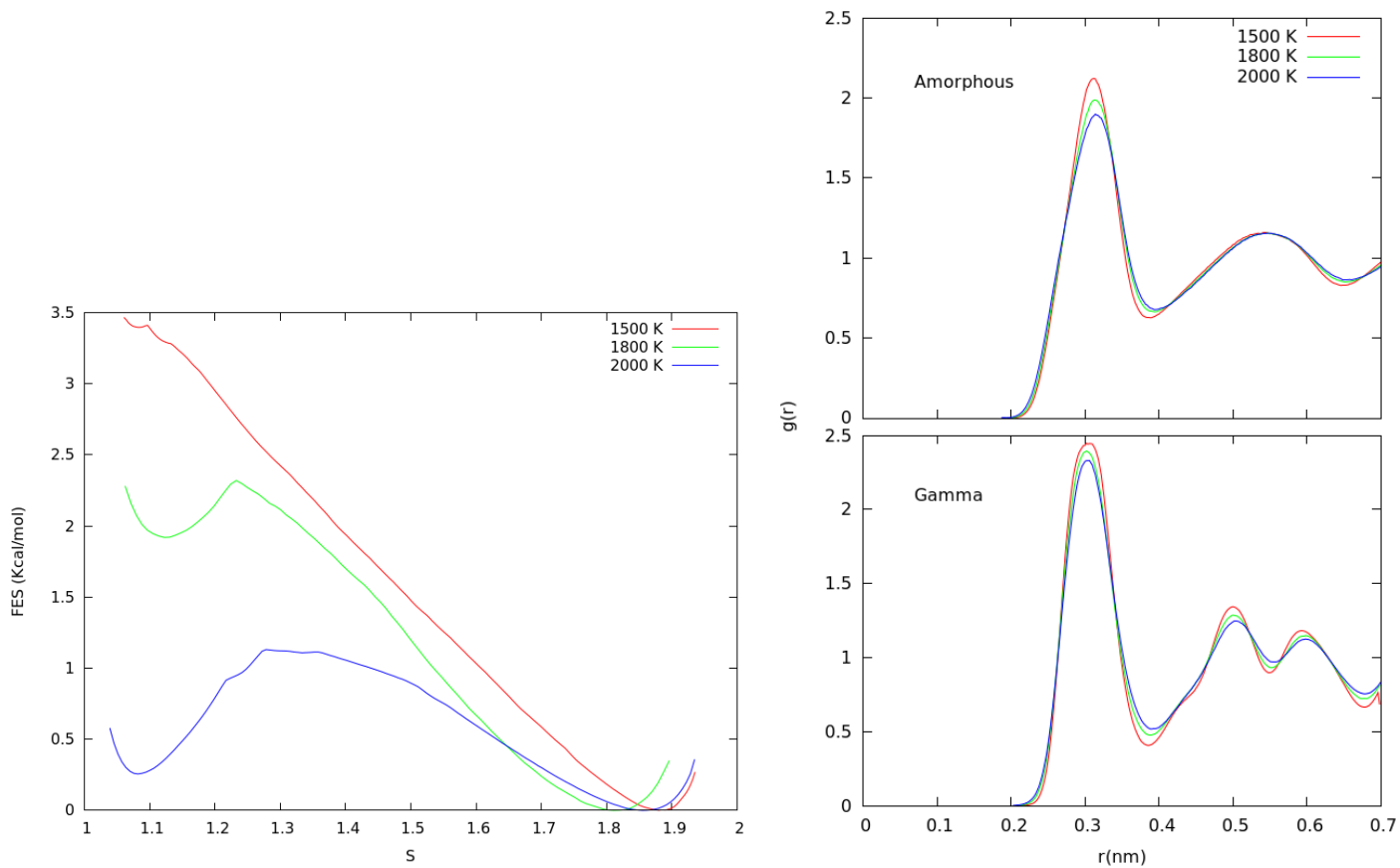


Figure 19: Free Energy Profiles for the amorphous-gamma transformation (left) and RDFs of the initial and final state at low temperatures (1500 - 2000K).

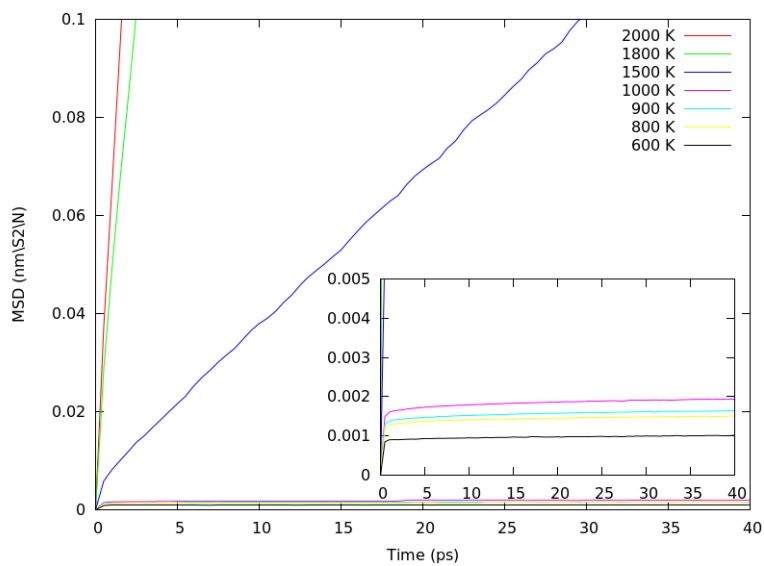


Figure 20: Mean Square Displacements (MSDs) of the disordered system at different temperatures.

4.2.4 DFT energy calculations:

Our goal was to test gamma alumina structure and their energies with respect to what we obtain in the classical molecular dynamics with our forcefield. We have used the same reference alumina structure proposed by Krokidis et al.[22] with a 960 atoms simulation cell. First of all, geometry optimization, done using the cp2k code, was reached after 27 steps with final total QS energy of 10043 a.u. After optimization, a sequence of MD simulations was done increasing temperature from 0 to 2000K with a step of 250K. At each temperature, we run a MD simulation for 4 ps, to calculate energies and characterize the structure using RDF plots. Finally, we compared the RDFs at each temperature with those calculated using classical MD. The comparison between the RDFs gives an overall match. In Figure 21, the RDFs from DFT are shifted manually by -0.026 nm.

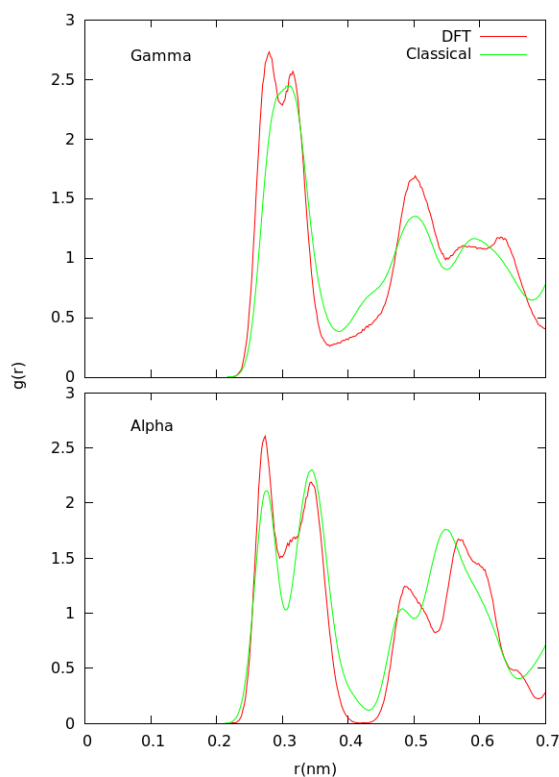


Figure 21: Comparison between RDFs calculated from the DFT and classical MDs simulations for both gamma and alpha alumina structures.

Chapter 5 Transitions among crystalline phases

In the previous section we have studied the first part (crystallization of gamma) of the transformation, i.e., the transition from the amorphous structure to alpha. Now we will proceed to the second part which is the phase transition from Gamma to Alpha alumina,

5.1 Optimization of Switching Functions for the PIV vector

Using the Path-PIV collective variable, PIV vectors are calculated between structures at each step. To calculate these vectors, switching functions are used as implemented in the plumed plugin. In general, the best switching function is the one that enhances the differences between structures present in the simulation at the topological level, therefore, the choice of the switching function to be used in each simulation depends on the reference structures specified.

We have tested 3 switching functions (SFs) for each simulation. Figure 22 shows the difference between these SFs with respect to the Aluminum – Aluminum radial distribution functions of the 3 alumina phase structures: Alpha, gamma and theta. The used SFs are of rational type with a functional form as following:

$$s(r) = \frac{1 - \left(\frac{r - d_0}{r_0}\right)^n}{1 - \left(\frac{r - d_0}{r_0}\right)^m}$$

Where d_0 , r_0 , m and n are parameters of the SFs, where d_0 is kept 0 as default. The parameters used for each SF are as following: SF₁ { $r_0 = 0.4$ nm, $n = 8$, $m = 3$ }, SF₂ { $r_0 = 0.4$ nm, $n = 12$, $m = 6$ } and SF₃ { $r_0 = 0.32$ nm, $n = 32$, $m = 16$ }.

As seen in Figure 22, SF₃ is very sharp and changes rapidly between the first and the second coordination shell, while SF₁ and SF₂ are smoother leading to sensitivity to changes at a larger range.

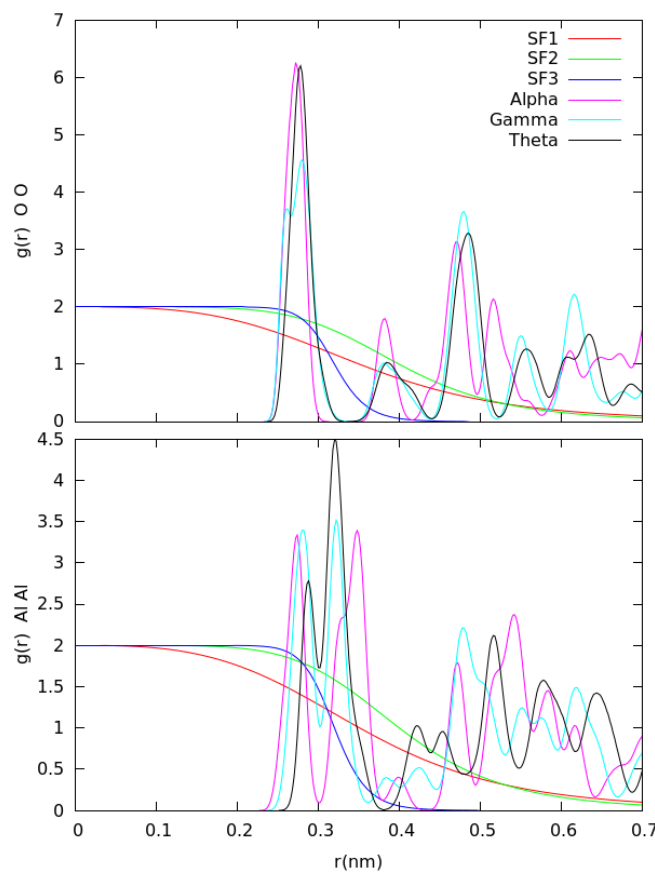


Figure 22: RDFs between Aluminum atoms alongside with different switching functions tested in this thesis.

5.2 Transitions between Alpha and Gamma structures

In this section, alpha and gamma structures are specified as the PathCV-PIV initial and final states in order to track the transformations between them. In the following paragraphs we present metadynamics simulations done in both directions for most of the temperature conditions, for the simulations that reached the final structure FESs are computed via Umbrella Sampling and WHAM.

5.2.1 Alpha to Gamma phase transition

We started the metadynamics simulation at **1000K** specifying alpha and gamma as the initial and final reference structures, respectively. The PIV vectors used in the collective variable

of this metadynamics simulation are constructed using switching functions as follows: SF_2 between Al atoms and SF_1 for Al - O and O - O distances. The parameters used for the gaussian potential are: $\delta_s = 0.008$, $\delta_z = 0.1$, height = 0.0249 Kcal/mol, and added every 1000 steps (a timestep of 1 fs is used).

Figure 23-A shows the progress of the transformation as a function of time in the configurational space $\{s, z\}$. Following the plot, we can see that the system has passed by different regions (seen as colored regions at different s values) in his way to reach the gamma alumina. The dark areas in the unconverged free energy profile (Figure 23-B) is a sign of energy minima. The darker the spot, the more time the system has spent in that area and the higher is the bias potential needed to overcome the barrier separating the region from the neighboring one. The 1D FES of this transformation (see Figure 24) along the variable “ s ” draws attention to the presence of at least 3 main energy minima other than those of the reference structures specified. Therefore, we can say that the path followed by the system is not direct and that it visits 3 metastable states before reaching the gamma alumina. The free energy difference between the initial and final structures is about 2.08 Kcal/mol while the energy barrier is estimated around 2.48 Kcal/mol.

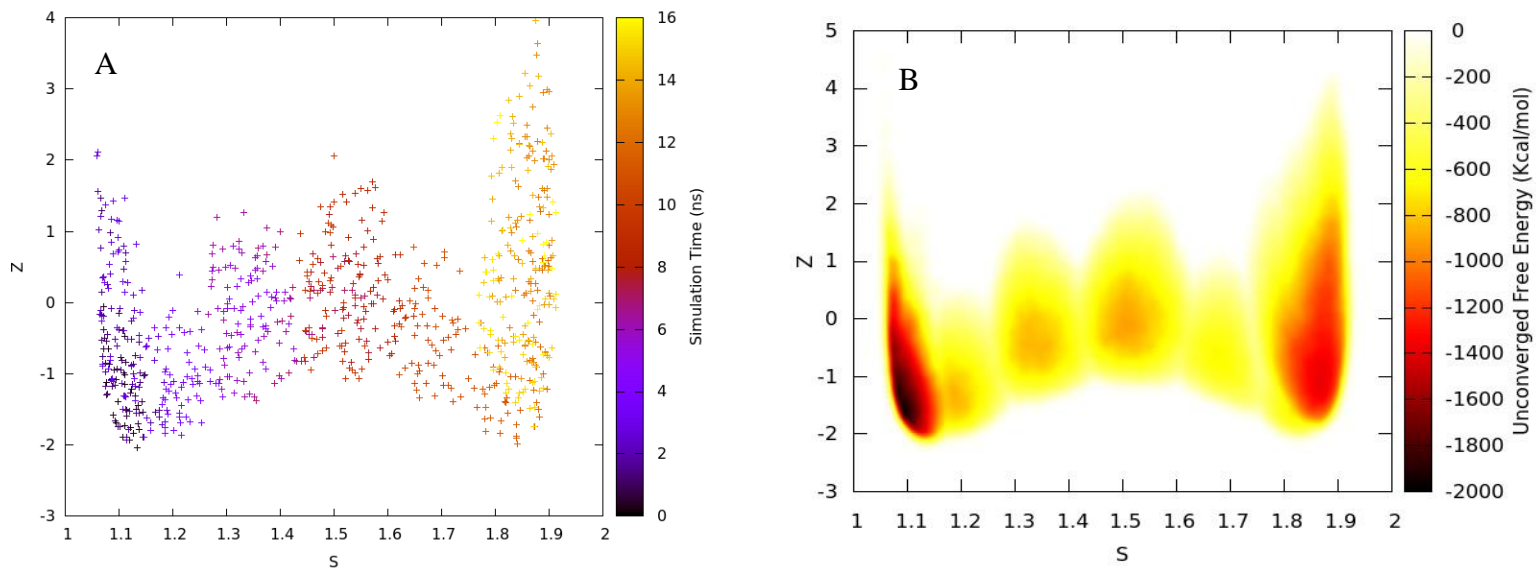


Figure 23: 3D graphs showing the A) time progress of the metadynamics simulation at 1000K starting from the alpha to gamma structure as function of simulation time (ns) and B) Unconverged free energy profile in the s - z space.

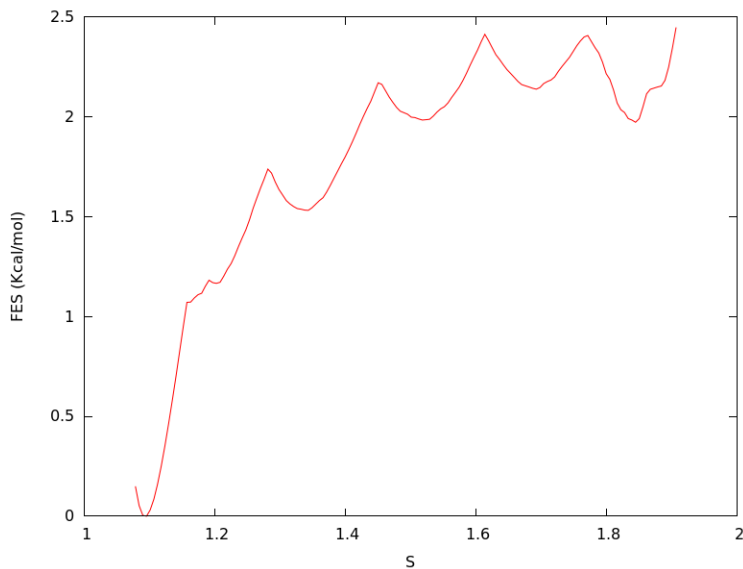


Figure 24: Free Energy Surface (in Kcal/mol) of the alpha to gamma transition at 1000K as a function of parameter s.

As in the transformation presented in 4.2, we studied the mechanism in terms of the Steinhardt parameters Q_4 and Q_6 . In Figures 25 and 26, Q_4 and Q_6 parameters, computed using different atomic couples, as function of the simulation time (ps) and the parameter S are presented.

Moreover, these figures show the behavior of “s” as a function of time, together with a plot of the time progress of the transformation in the CV space.

The Q_4 and Q_6 Oxygen - Oxygen clearly change by discrete steps along time and also along the transformation coordinate, and such steps are in phase with the steps of the transformation coordinate (s) as a function of time, meaning that the different energy minima we see in the FES plot correspond to the symmetry change of the Oxygen-Oxygen network from the hcp of the alpha phase to the fcc of the gamma phase, in a discrete phenomenon. This can be confirmed by the comparison of the starting and final values of the Oxygen-Oxygen steighnart parameters with that of the perfect lattices [63] (see Table 2).

The Oxygens displacements are accompanied by a change in the position of Aluminum atoms and by an increase in the volume of the cell (the expansion of the cell is shown in Figure 27). The decreasing number of the tetrahedral Aluminum atoms ($Q_{4 \text{ Al-O}}$ decreases from 0.59 to 0.54) are offset by a noticeable increase in the octahedral Aluminum atoms ($Q_{6 \text{ Al-O}}$ increased from 0.325 to 0.42). Therefore, we can summarize the mechanism of the transformation from Alpha to Gamma at 1000K with the ordering of Oxygen network combined with the movement of Aluminum atoms from tetrahedral to Octahedral sites.

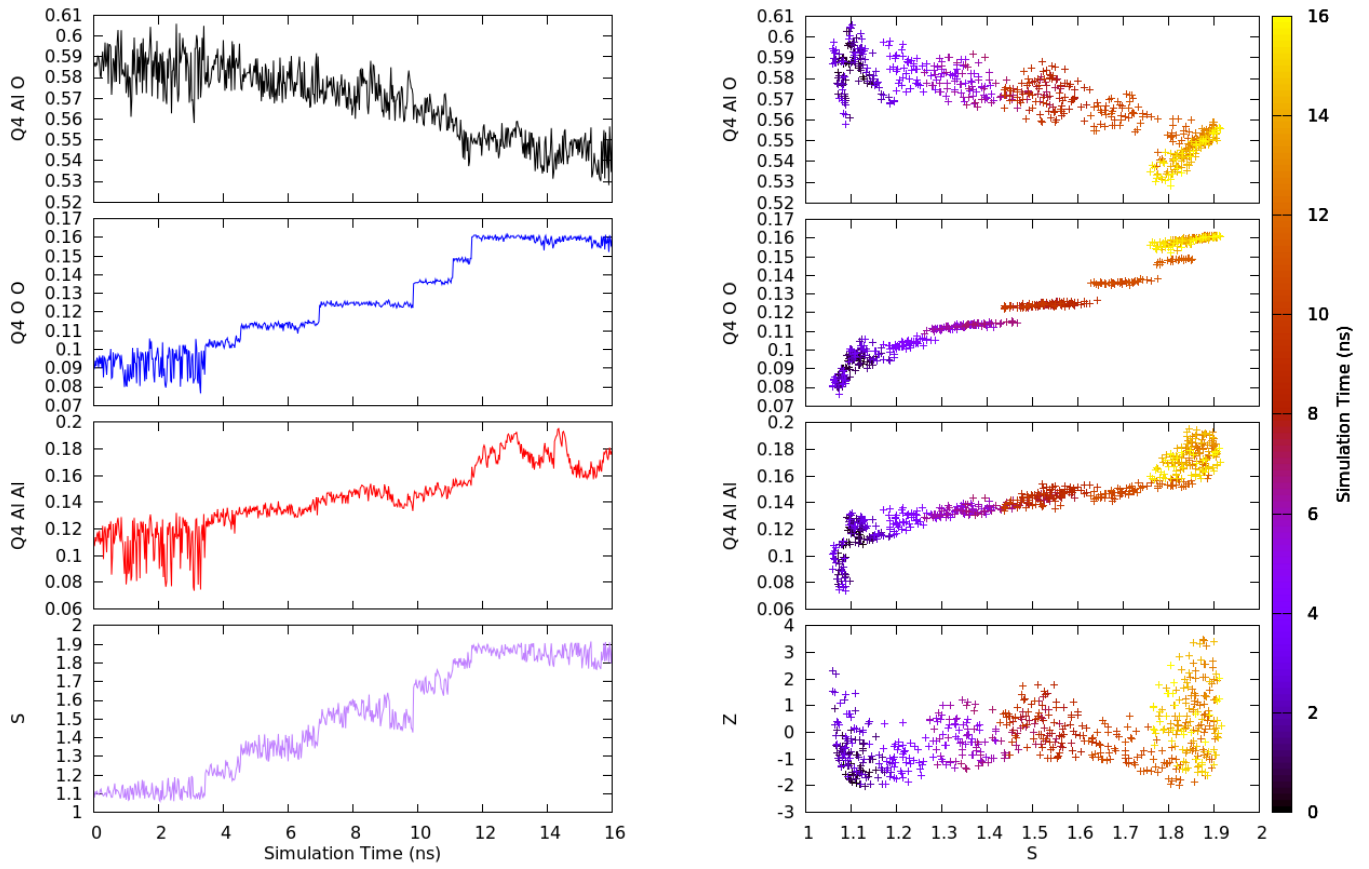


Figure 25: The variation of Steinhardt parameter Q_4 between different atoms of the system along the transition from alpha to gamma structure at 1000K as function of time(ns) (left) and s (right).

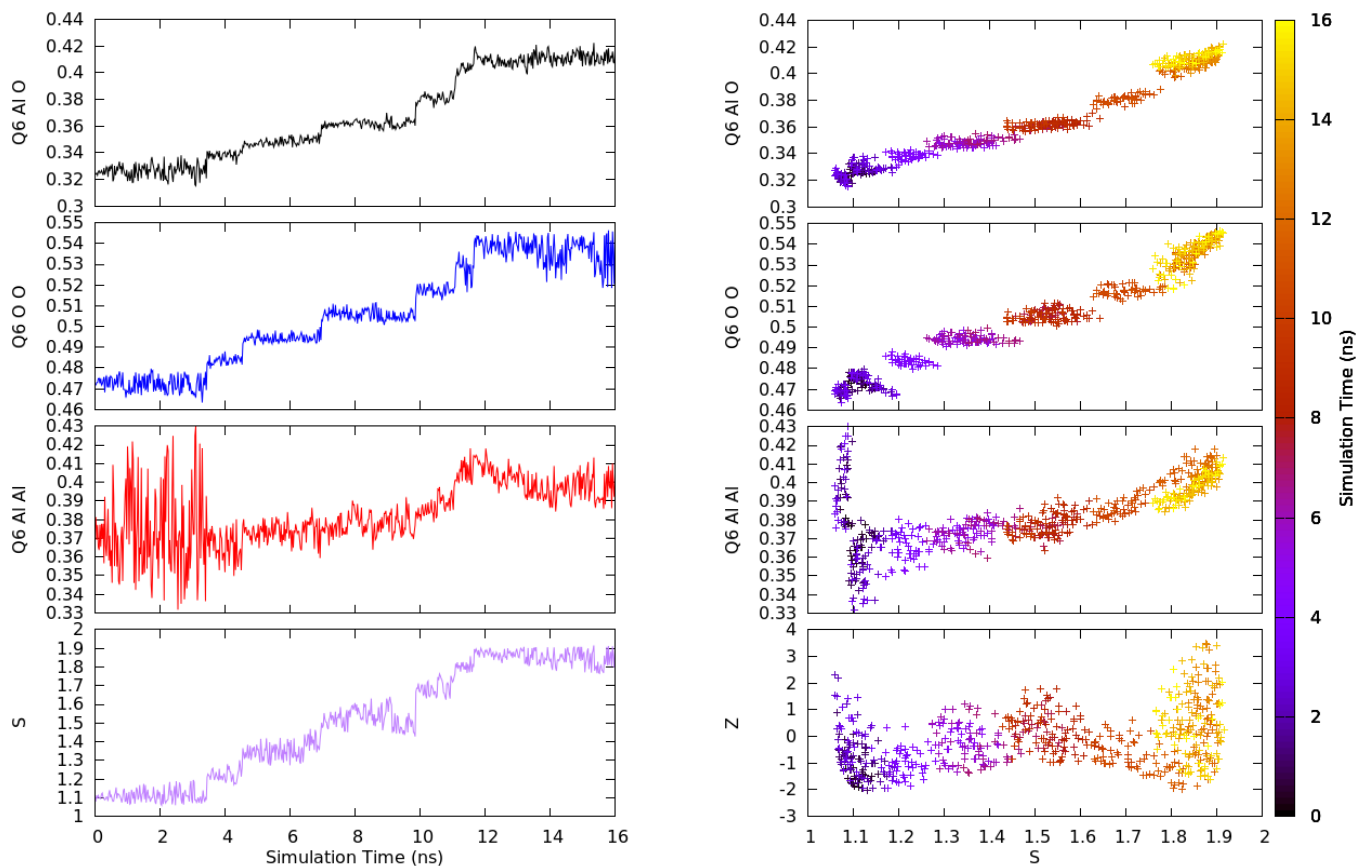


Figure 26: The variation of Steinhardt parameter Q_6 between different atoms of the system along the transition from alpha to gamma structure at 1000K as function of time (ns) (left) and parameter s (right).

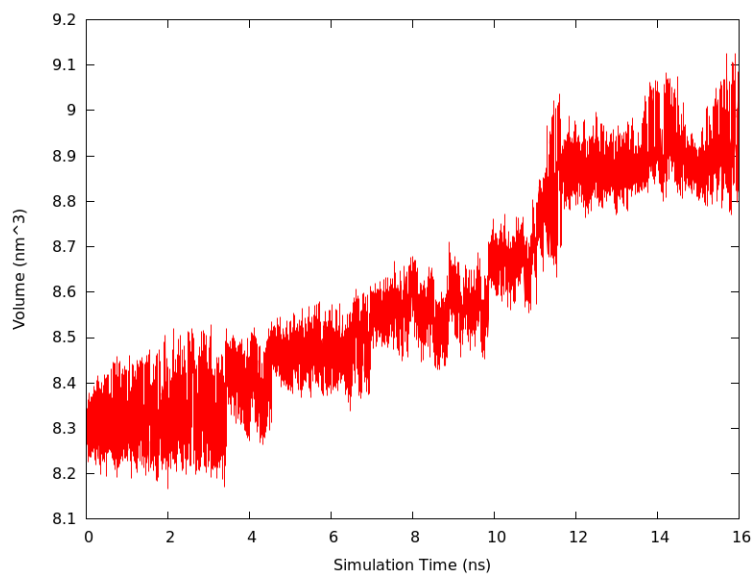


Figure 27: The variation of volume of the system along the transition from alpha to gamma structure at 1000K as function of time (ns).

5.2.2 Temperature Dependence:

We performed the same transformation at different temperatures to study the effect on the FES and the transformation mechanism. In addition to the previous simulation at 1000K, we have performed the simulation at 1500, 1200 and 500K. At each temperature we have tested and optimized numerous parameters including the switching function and gaussian bias potential. The transition was achieved with different parameters at each temperature; however, we will be showing the simulations with the best exploration of the configurational space.

We start by increasing the temperature to 1200K. The simulation used SF_1 between all atoms in the system with the following parameters for the bias potential: width = $\{\delta_s = 0.0087, \delta_z = 1.79\}$, height = 0.00186 Kcal/mol and frequency every 200 steps. The FES and the mechanism are similar to the transformation at 1000K: the system visited some metastable structures (colored regions in Figure 28 (A) and black spots in the unconverged free energy profile in Figure 28 (B)). These intermediates appear as tiny minima along the converged FES in Figure 29 with smaller barriers between them. The difference in free energy between the two stable structures is 2.021 Kcal/mol with an overall energy barrier of 2.885 Kcal/mol. In Figures 30 and 31 we present Q_4 and Q_6 parameters to confirm that the mechanism is similar to the one seen at 1000K.

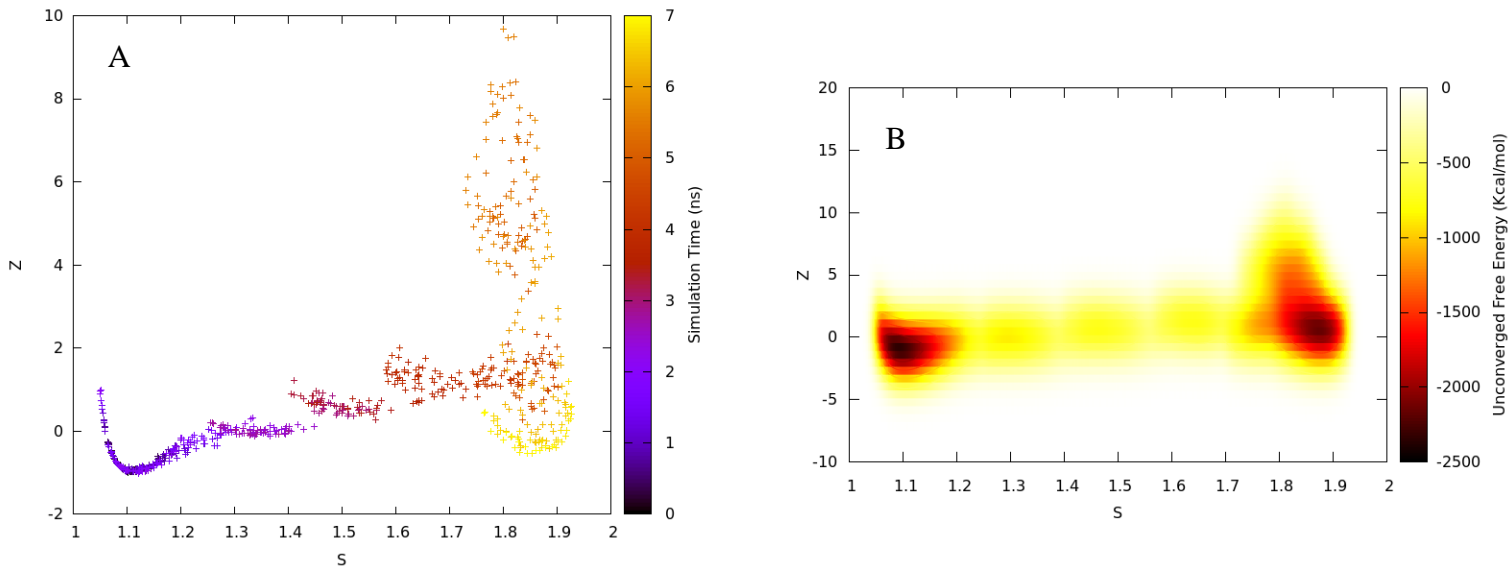


Figure 28: 3D graphs showing the A) time progress of the metadynamics simulation at 1200K starting from the alpha to gamma structure as function of simulation time (ns) and B) Unconverged free energy profile in the s - z space.

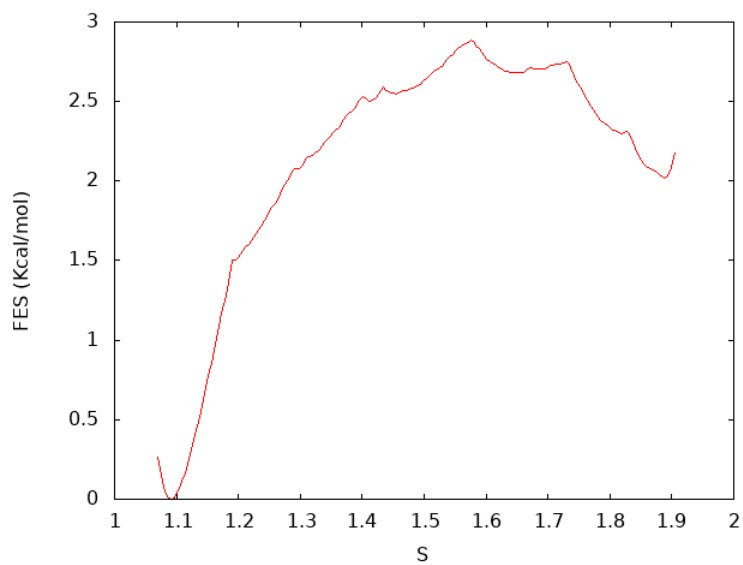


Figure 29: Free Energy Surface (Kcal/mol) of the alpha to gamma transition at 1200K as function of parameter s.

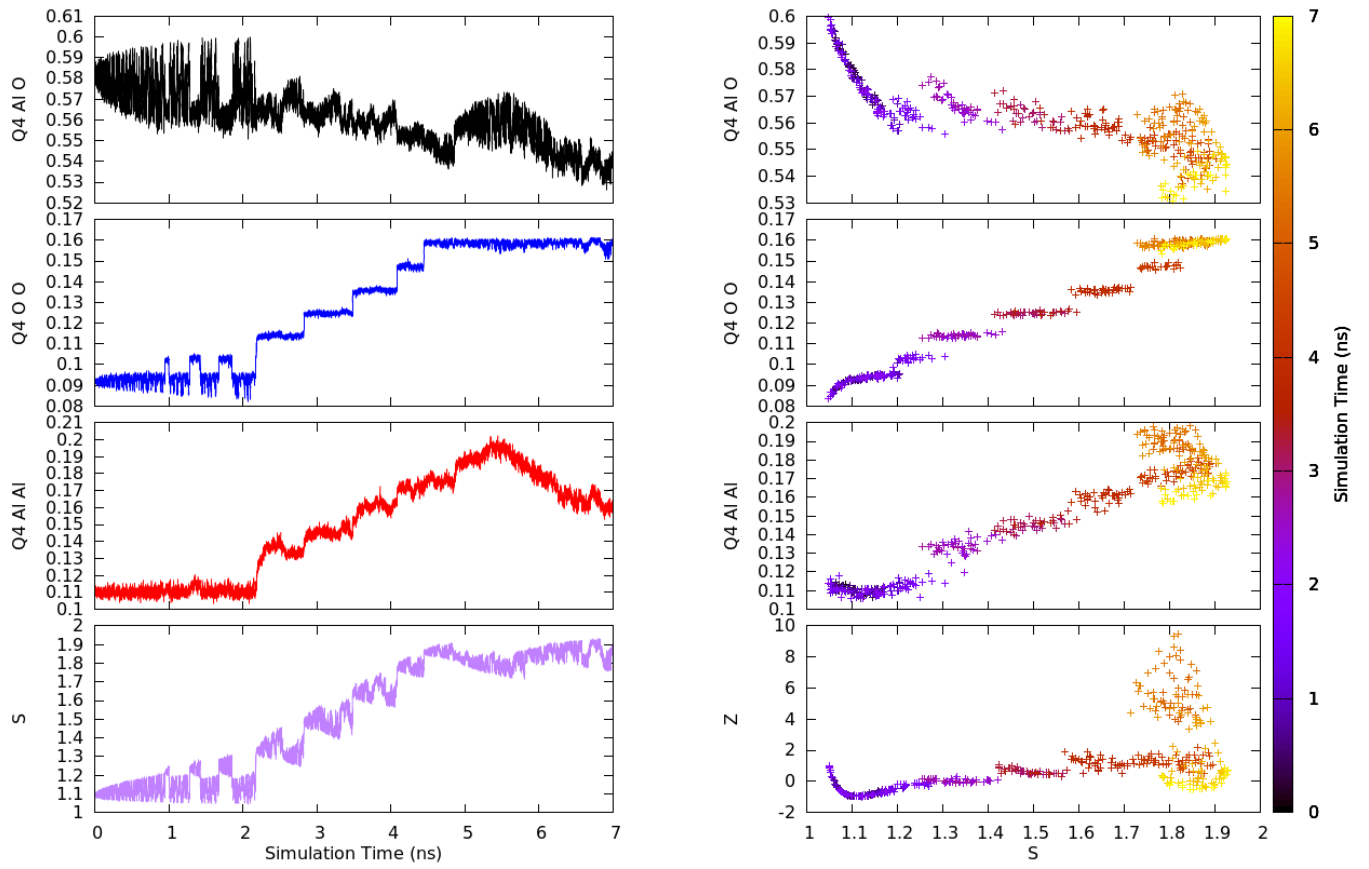


Figure 30: The variation of Steinhardt parameter Q_4 between different atoms of the system along the transition from alpha to gamma structure at 1200K as function of time(ns) (left) and s (right).

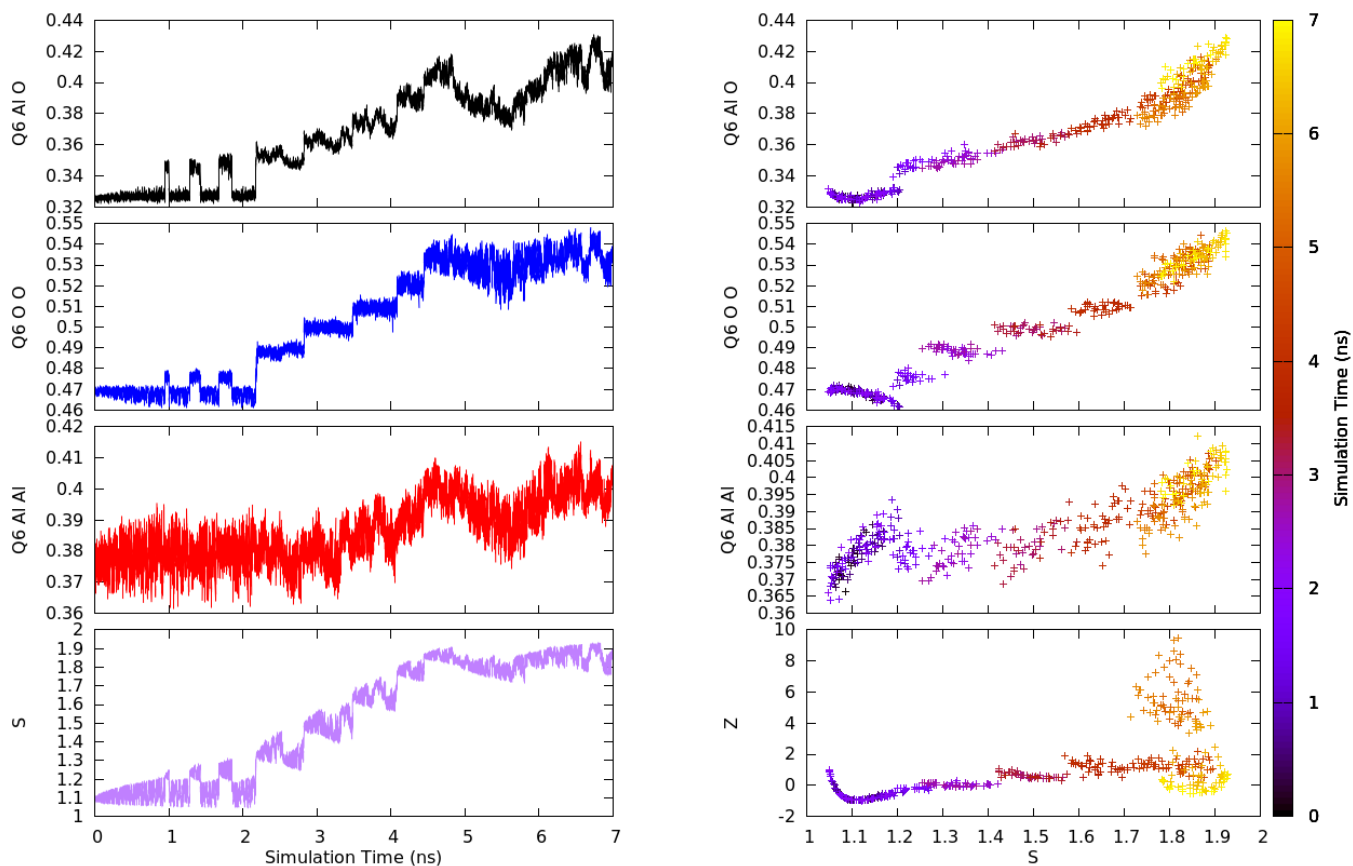


Figure 31: The variation of Steinhardt parameter Q_6 between different atoms of the system along the transition from alpha to gamma structure at 1200K as function of time(ns) (left) and s (right).

Increasing temperature to 1500K, the simulation reaches a good alpha structure (compared with energies and RDFs with the reference Alpha alumina). We used SF_3 for PIV_{Al-Al} and SF_1 for the rest. The gaussian biased potential added is of width = $\{\delta_s = 0.0087, \delta_z = 1.7976\}$, height = 0.02489 Kcal/mol and frequency every 1000 steps.

The transition appears to be smooth; only two main energy minima can be seen in the 3D configurational space (Figure 32) and converged Free energy surface computed after umbrella sampling (Figure 33). The difference in free energy between the initial and final structures is around 1.98 Kcal/mol which is more or less the same as the one obtained at 1000K, while the energy barrier decreases to about 1.994 Kcal/mol.

Figures 34 and 35 show the Steinhardt parameters as a function of time and the parameter s . In Figure 34 we still see a few steps in the evolution of Oxygen - Oxygen Q_4 as a function of time, but the other parameters change in a smoother way along time and the transformation coordinate.

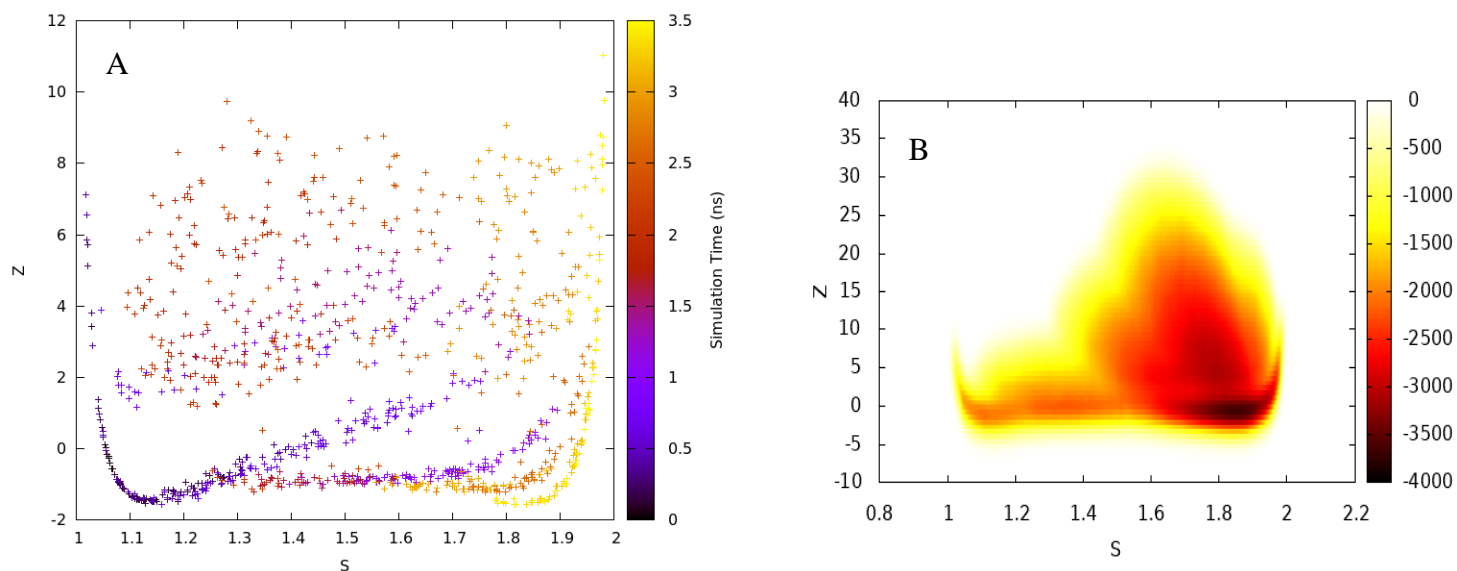


Figure 32: 3D graphs showing the A) time progress of the metadynamics simulation at 1500K starting from alpha to gamma structure as function of simulation time (ns) and B) Unconverged free energy profile in the $s - z$ space.

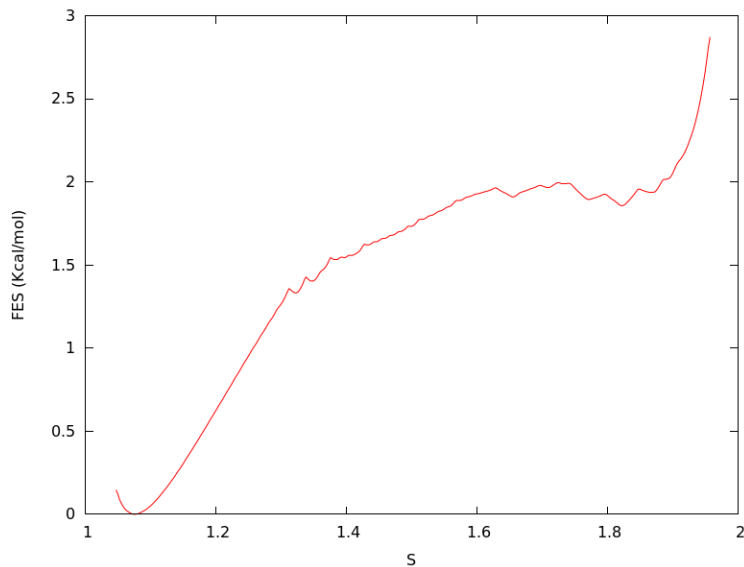


Figure 33: Free Energy Surface (Kcal/mol) of the transition from alpha to gamma at 1500K as function of parameter s .

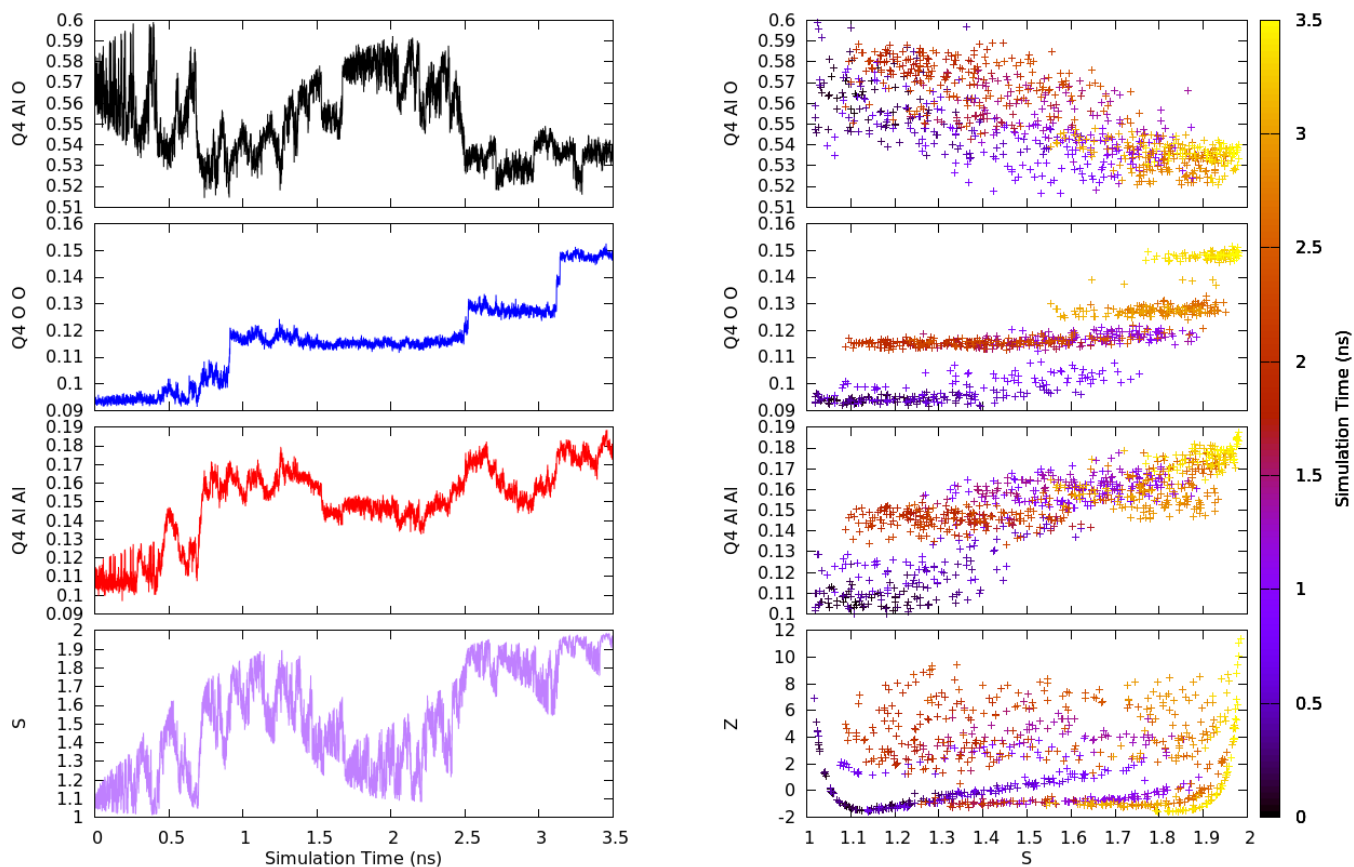


Figure 34: The variation of Steinhardt parameter Q_4 between different atoms of the system along the transition from alpha to gamma structure at 1500K as function of time(ns) (left) and s (right).

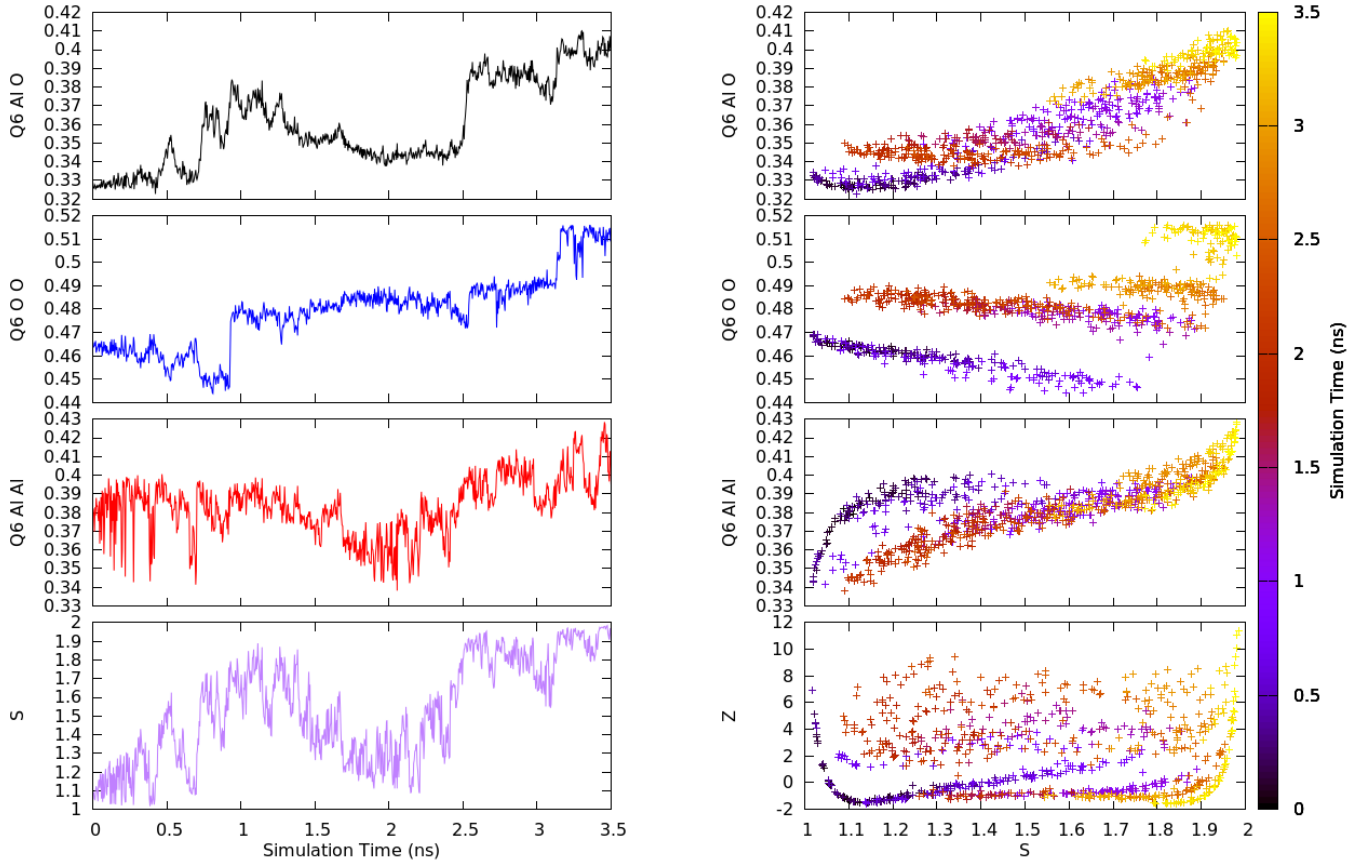


Figure 35: The variation of Steinhardt parameter Q_6 between different atoms of the system along the transition from alpha to gamma structure at 1500K as function of time(ns) (left) and s (right).

To summarize, increasing temperature from 1000 to 1200 to finally 1500K we still find parameters changing step-by-step in a discrete fashion but free energy barriers between the different intermediate structures decrease as a function of temperature and at 1500K the FES becomes smooth. This behavior can be explained with the increase in the kinetic energy of the system as a function of temperature.

In order to check whether this behavior also holds at lower temperatures, we performed the transformation at **500K**. At this temperature, the system has a lower kinetic energy and atoms need stronger bias potential to change their relative positions. Therefore, simulations at this temperature were longer. This simulation used SF_2 for PIV_{Al-Al} and SF_1 for the rest of PIV calculated with parameters for the biased potential as follows: $\delta_s = 0.008$, $\delta_z = 0.2$, and height =

0.0186 Kcal/mol added every 1000 steps. A step-by-step discrete mechanism, just as we've found at 1000K is clear both in FES (figures 36 and 37) and Steinhardt's parameters plots (figures 38 and 39).

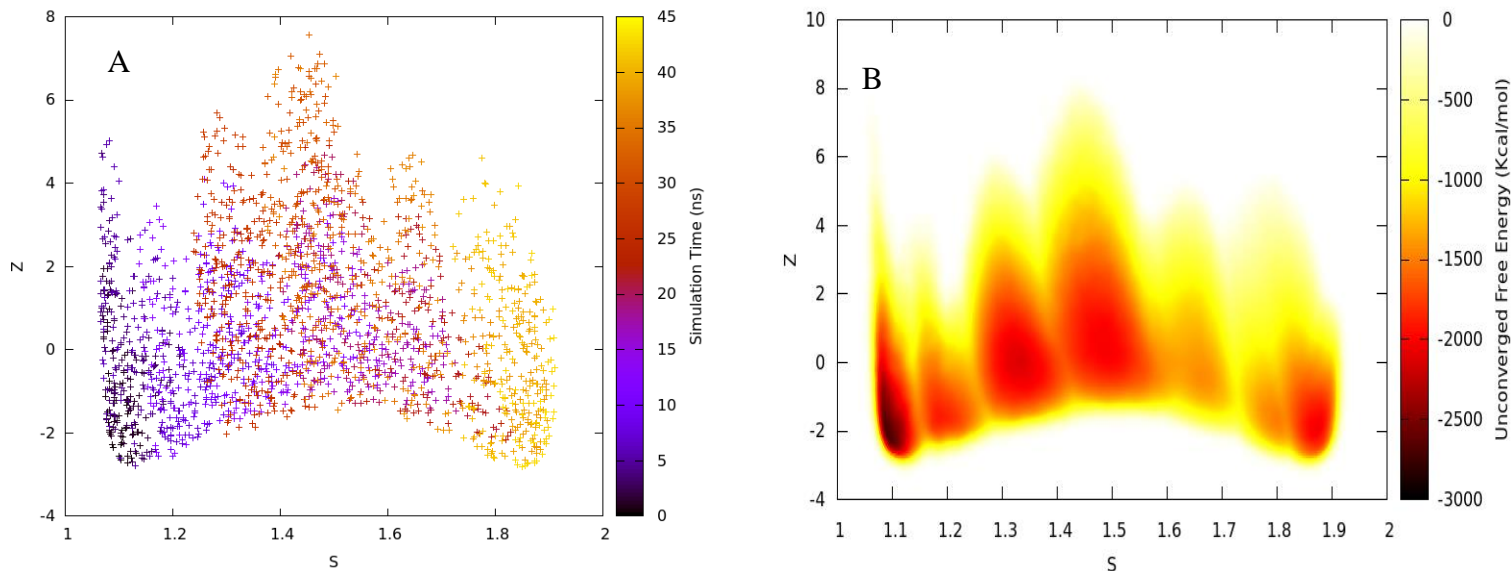


Figure 36: 3D graphs showing the A) time progress of the metadynamics simulation at 500K starting from the alpha to gamma structure as function of simulation time (ns) and B) Unconverged free energy profile in the $s - z$ space.

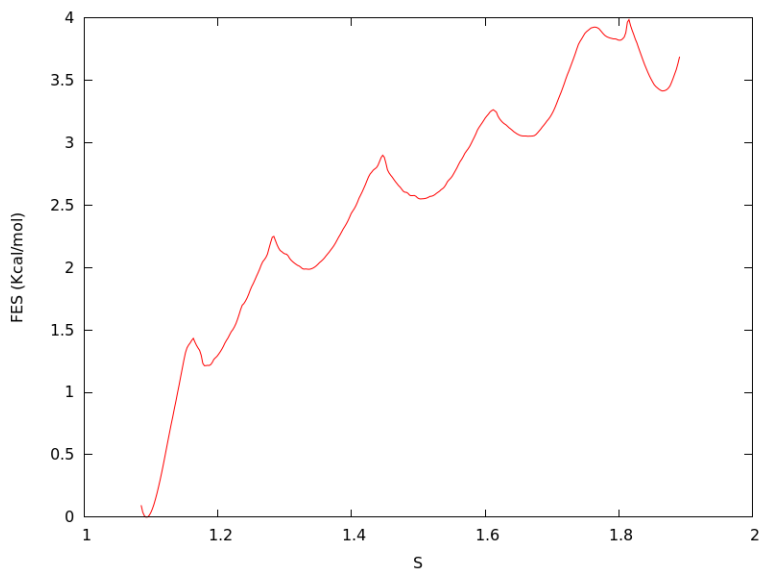


Figure 37: Free Energy Surface of the transition from alpha to gamma structure at 500K as function of parameter s .

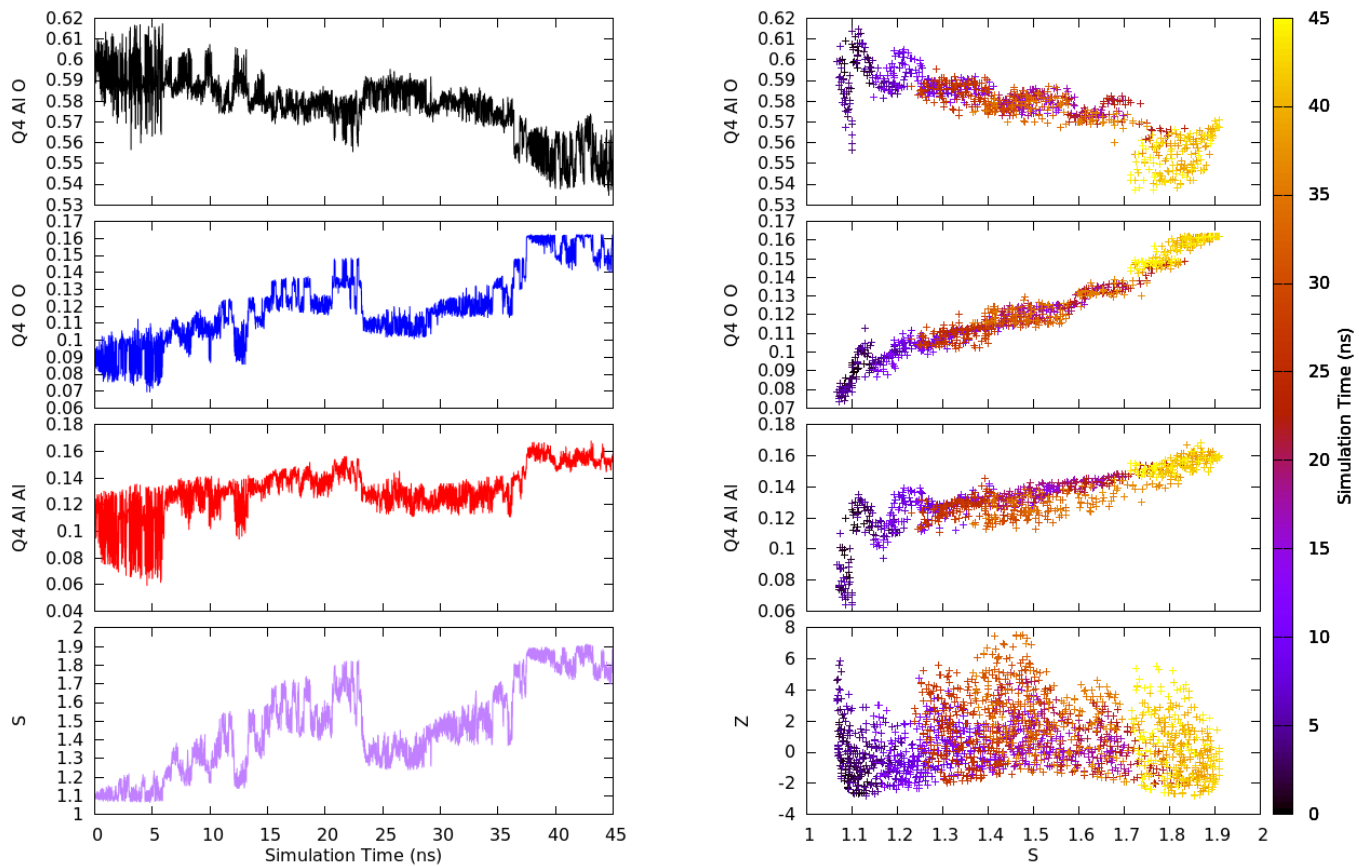


Figure 38: The variation of Steinhardt parameter Q_4 between different atoms of the system along the transition from alpha to gamma structure at 500K as function of time(ns) (left) and s (right).

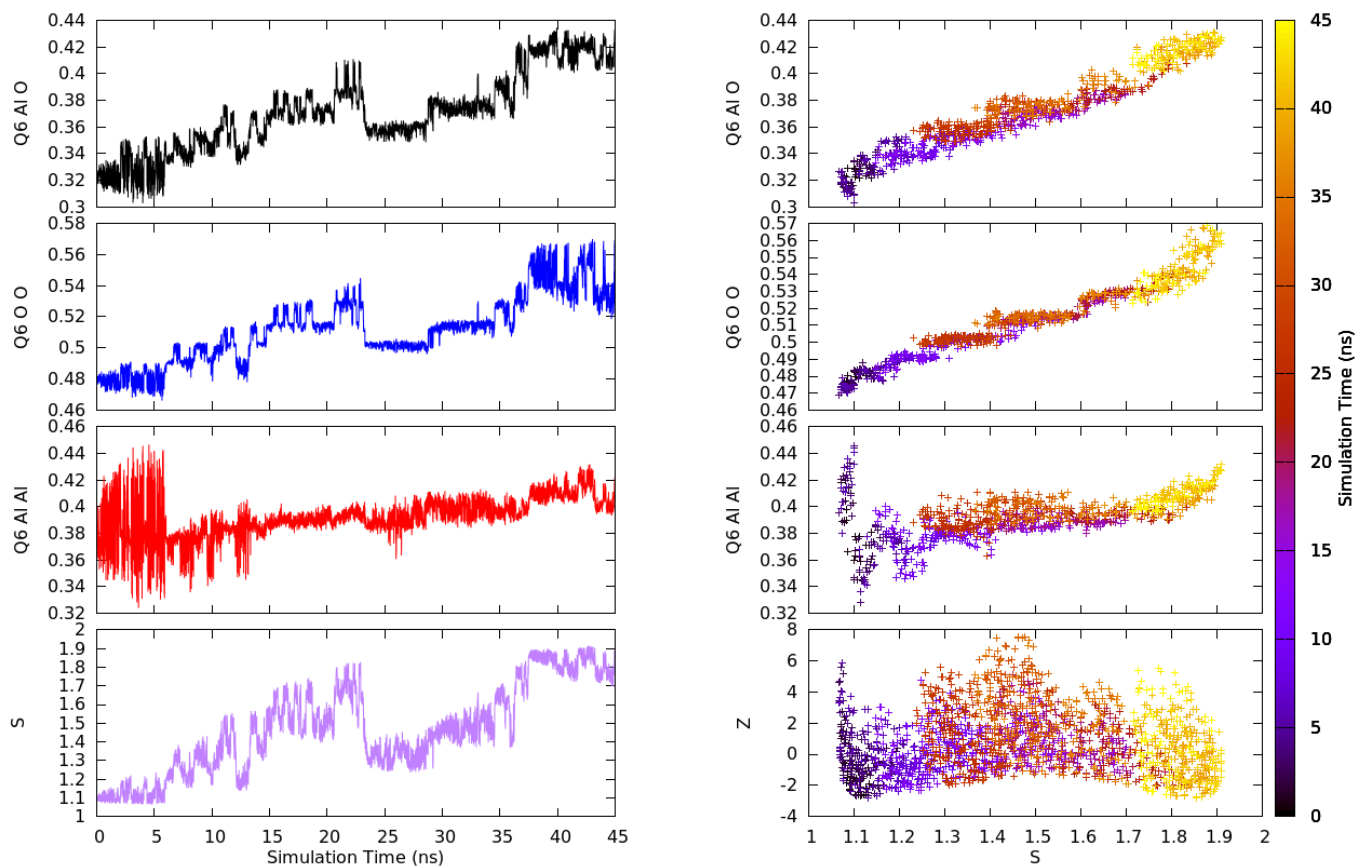


Figure 39: The variation of Steinhardt parameter Q_6 between different atoms of the system along the transition from alpha to gamma structure at 500K as function of time(ns) (left) and s (right).

In Figure 40 we summarize the FES plots at different temperatures to highlight the lowering of the barriers between intermediate structures as a function of temperature. Concerning the free energy difference, we find that gamma becomes more and more stable as the temperature increases from 500 to 1000 K but moving from 1000K to 1500K the free energy difference remains substantially constant at about 2 kcal/mol.

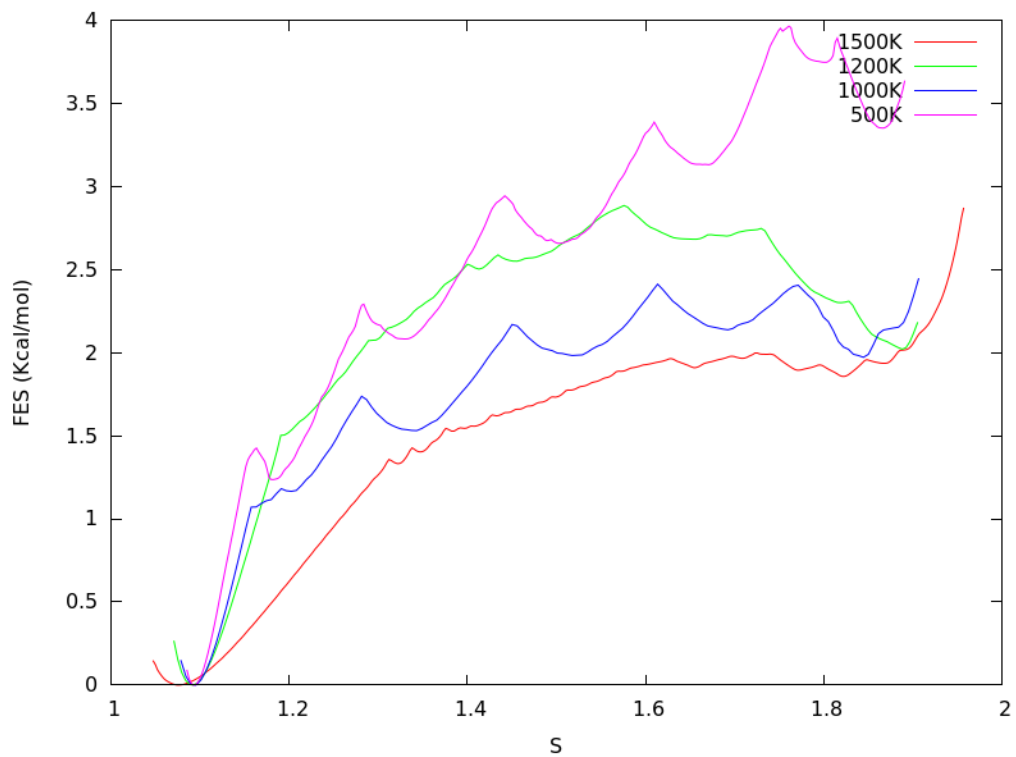


Figure 40: Comparison between FES computed at different temperatures of the transition from alpha to gamma structure.

5.3 Transitions between Theta and Gamma structures

In this section we present simulations on the transformation between the gamma and theta alumina at 1200K and 1500K. According to literature, these two structures have the same face-centered cubic (fcc) arrangement of oxygen atoms but the cations occupy octahedral and tetrahedral sites with different ratios. Therefore, the only way to discriminate between these two structures is by focusing on the Aluminum network to build the PIV.

In the simulation at 1500K we used a bias gaussian potential with parameters: $\delta s = 0.008772$, $\delta z = 1.79$, height = 0.0037 Kcal/mol and added with frequency every 400 steps. The two 3D configurational space plots represented in Figure 41 (time progress of simulation and unconverged free energy profile) show that the transformation is direct and fast. The FES computed with US is shown in Figure 42 shows that the difference in energy between the two structures is very low (0.317 Kcal/mol) with a tiny energy barrier of 0.863 Kcal/mol. Figures 43 and 44 show the Steinhardt's parameters for this transformation.

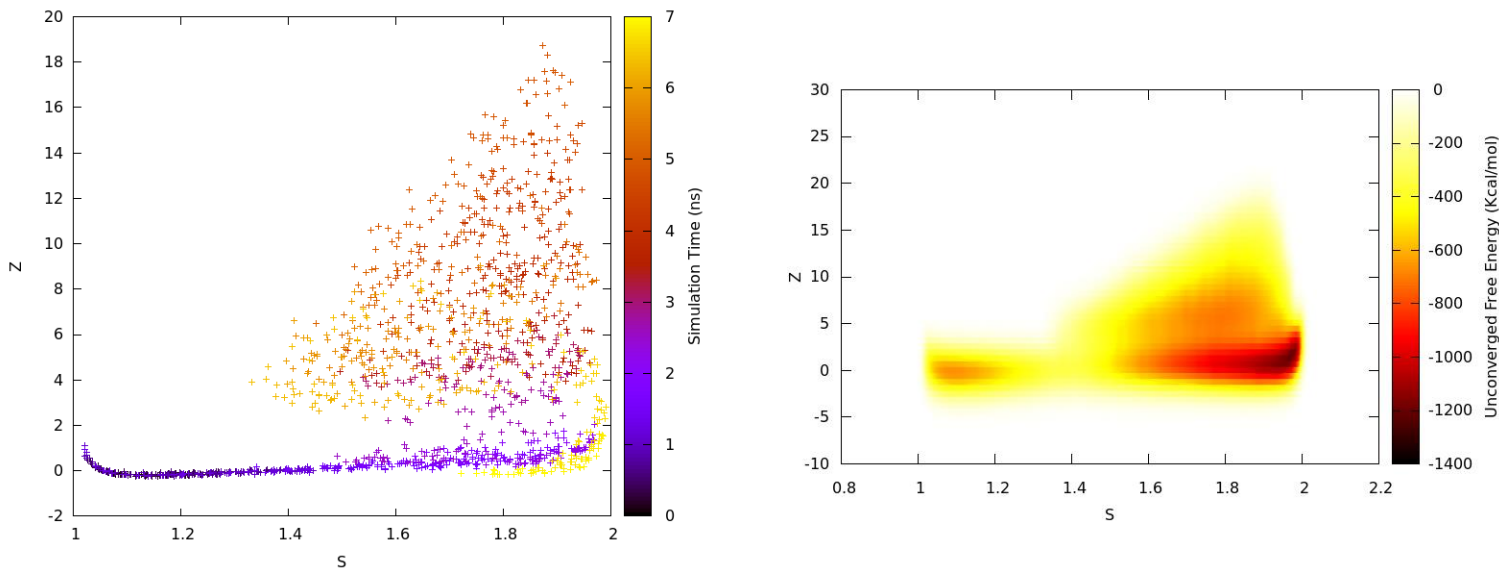


Figure 41: 3D graph showing the A) time progress of the metadynamics simulation at 1500K starting from theta to gamma structure as function of simulation time (ps) and B) Unconverged free energy profile in the $s - z$ space.

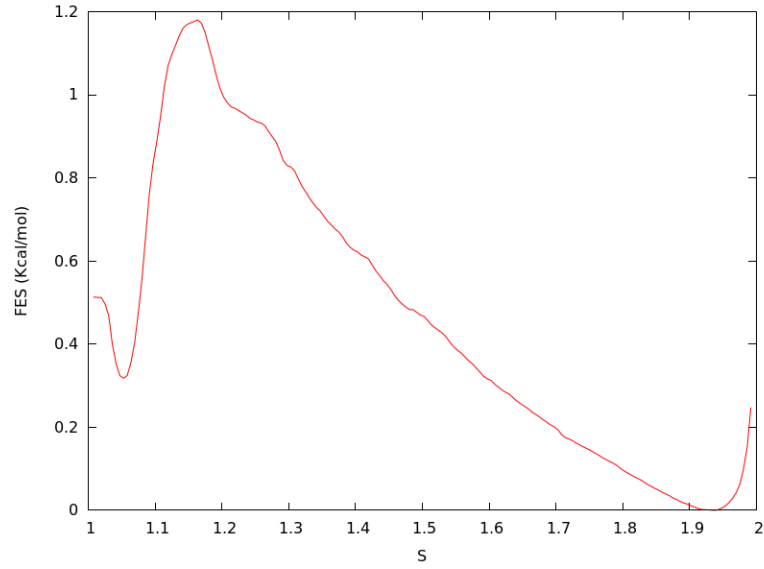


Figure 42: Free Energy Surface (Kcal/mol) of the theta to gamma transition at 1500K as function of parameter s .

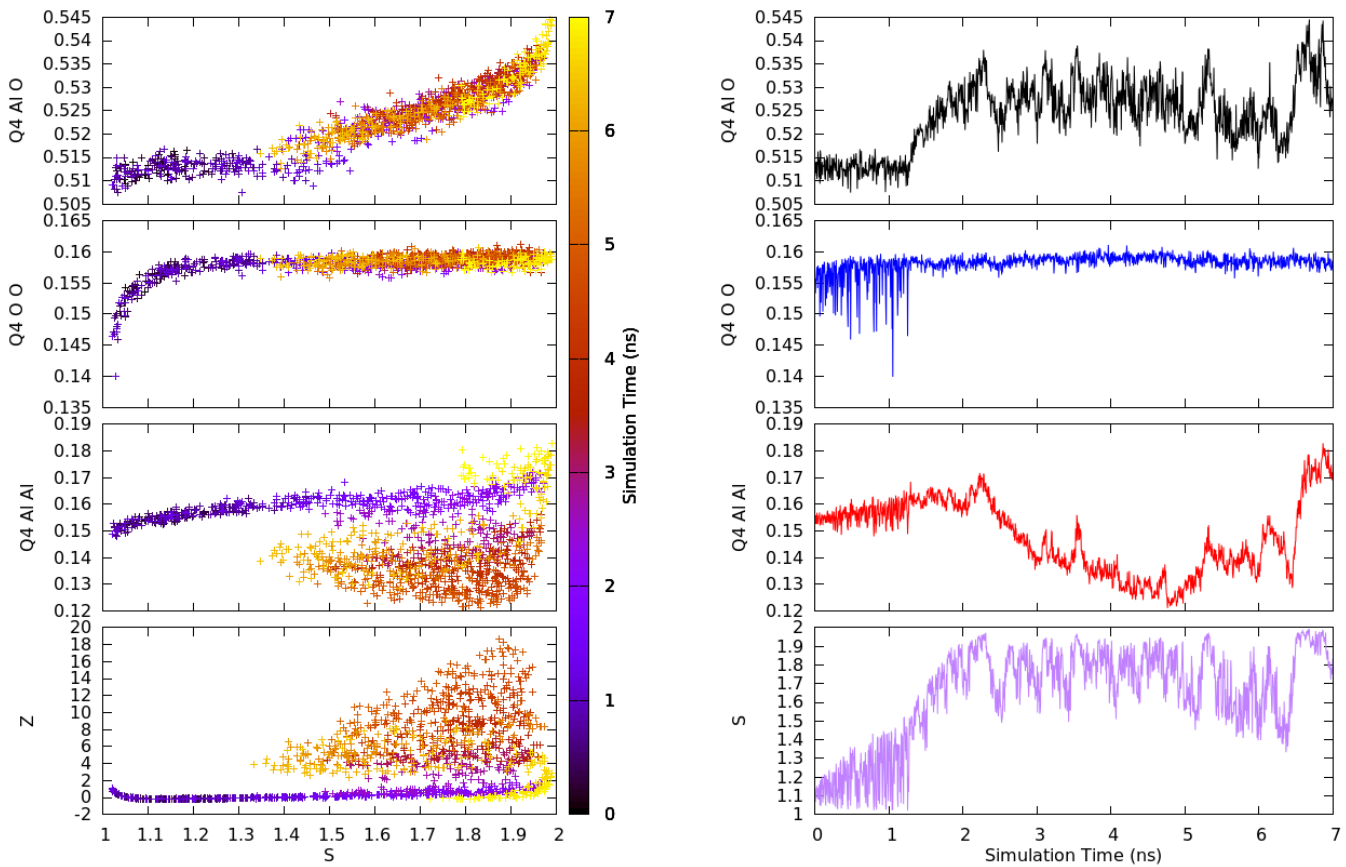


Figure 43: The variation of Steinhardt parameter Q_4 between different atoms of the system along the transition from theta to gamma structure at 1500K as function of time(ns) (left) and s (right)

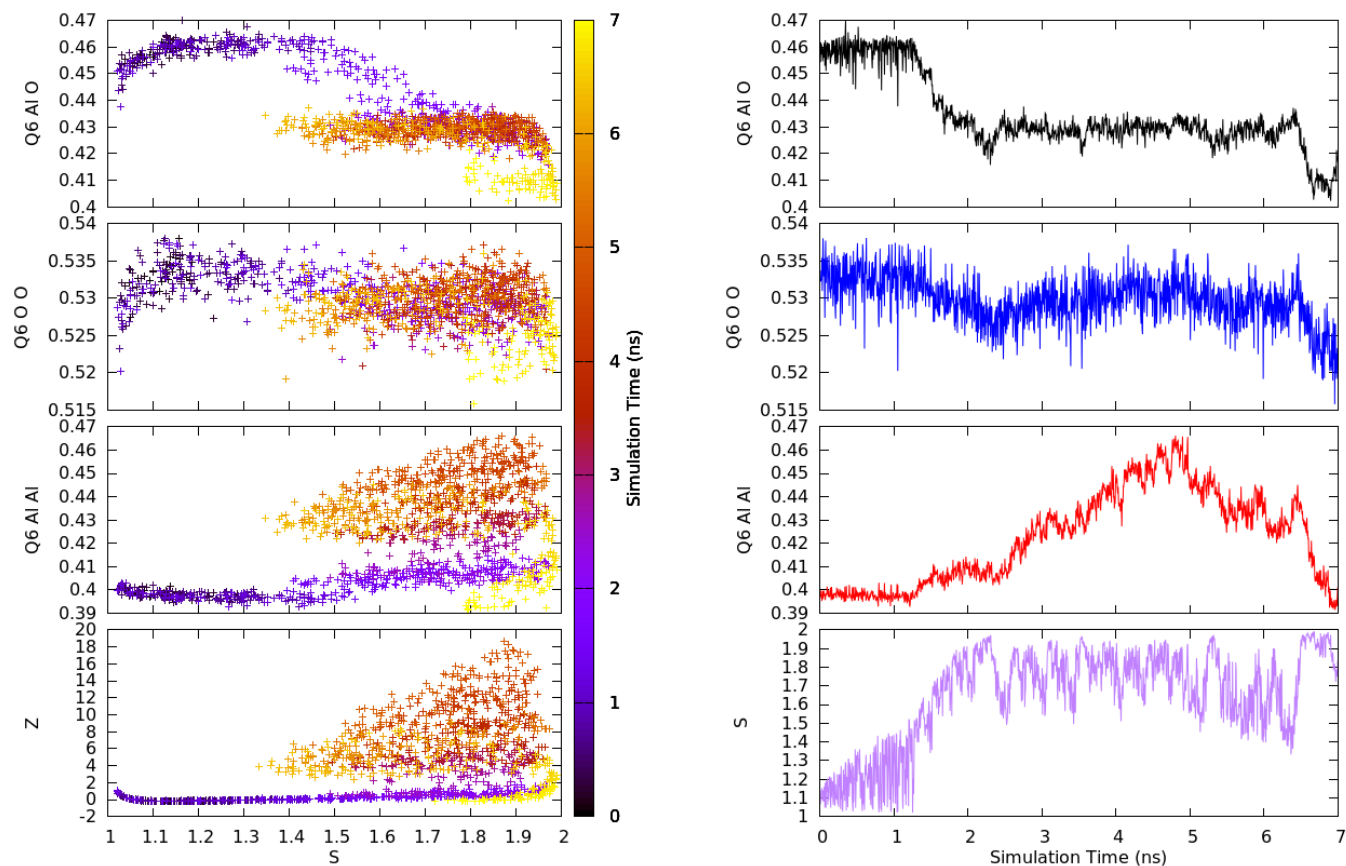


Figure 44: The variation of Steinhardt parameter Q_6 between different atoms of the system along the transition from theta to gamma structure at 1500K as function of time(ns) (left) and s (right).

At 1200K ($\delta s = 0.00877$, $\delta z = 0.79$, height = 0.0037 Kcal/mol) no big differences are found with respect to 1500K, free energy plots and descriptors are presented in figures below (Figures 45, 46, 47 and 48). At this temperature, the FES shows that theta becomes more stable than gamma.

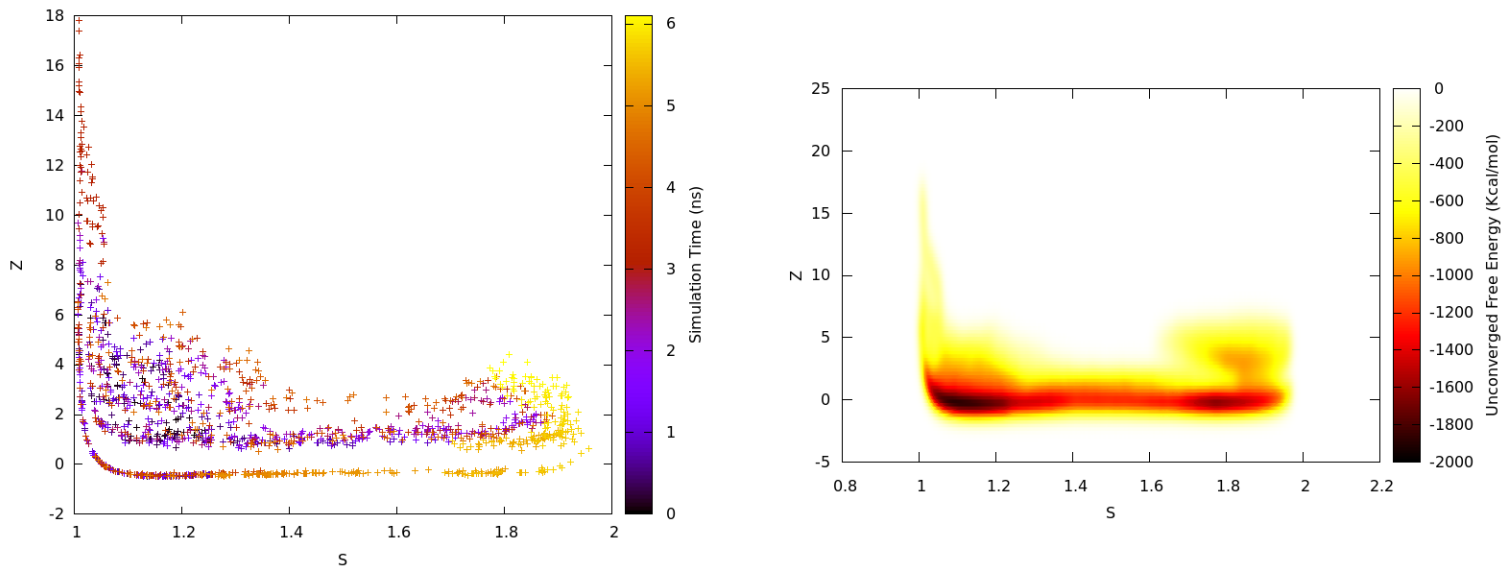


Figure 45: 3D graph showing the A) time progress of the metadynamics simulation at 1200K starting from theta to gamma structure as function of simulation time (ps) and B) Unconverged free energy profile in the s - z space.

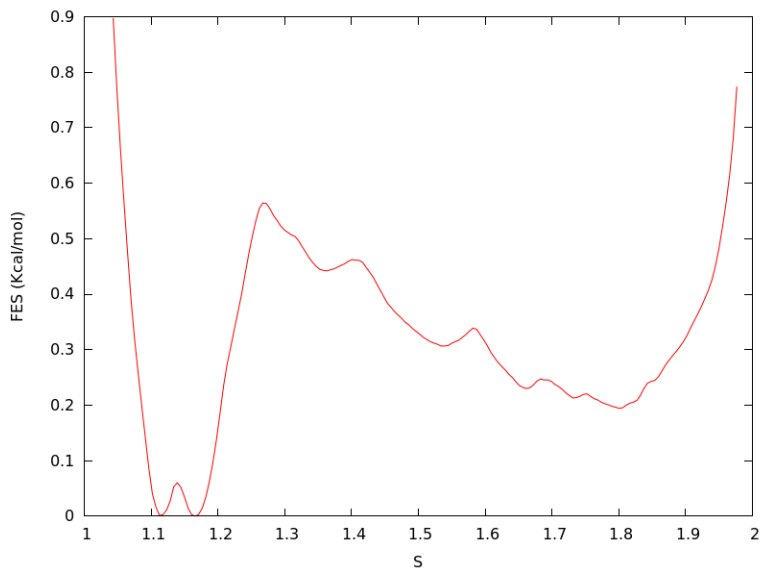


Figure 46: Free Energy Surface (Kcal/mol) of the theta to gamma transition at 1200K as function of parameter s.

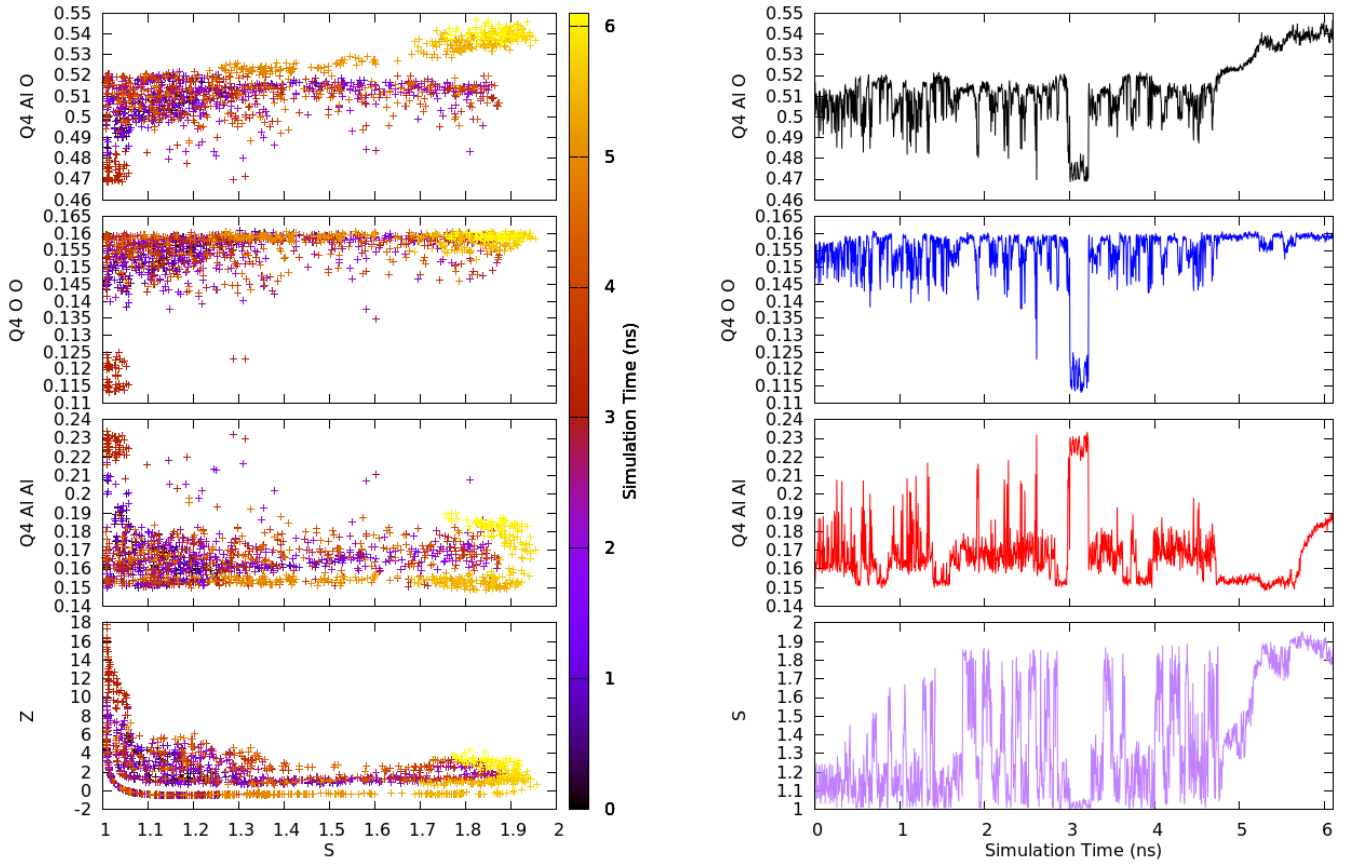


Figure 47: The variation of Steinhardt parameter Q_4 between different atoms of the system along the transition from theta to gamma structure at 1200K as function of time(ns) (left) and s (right).

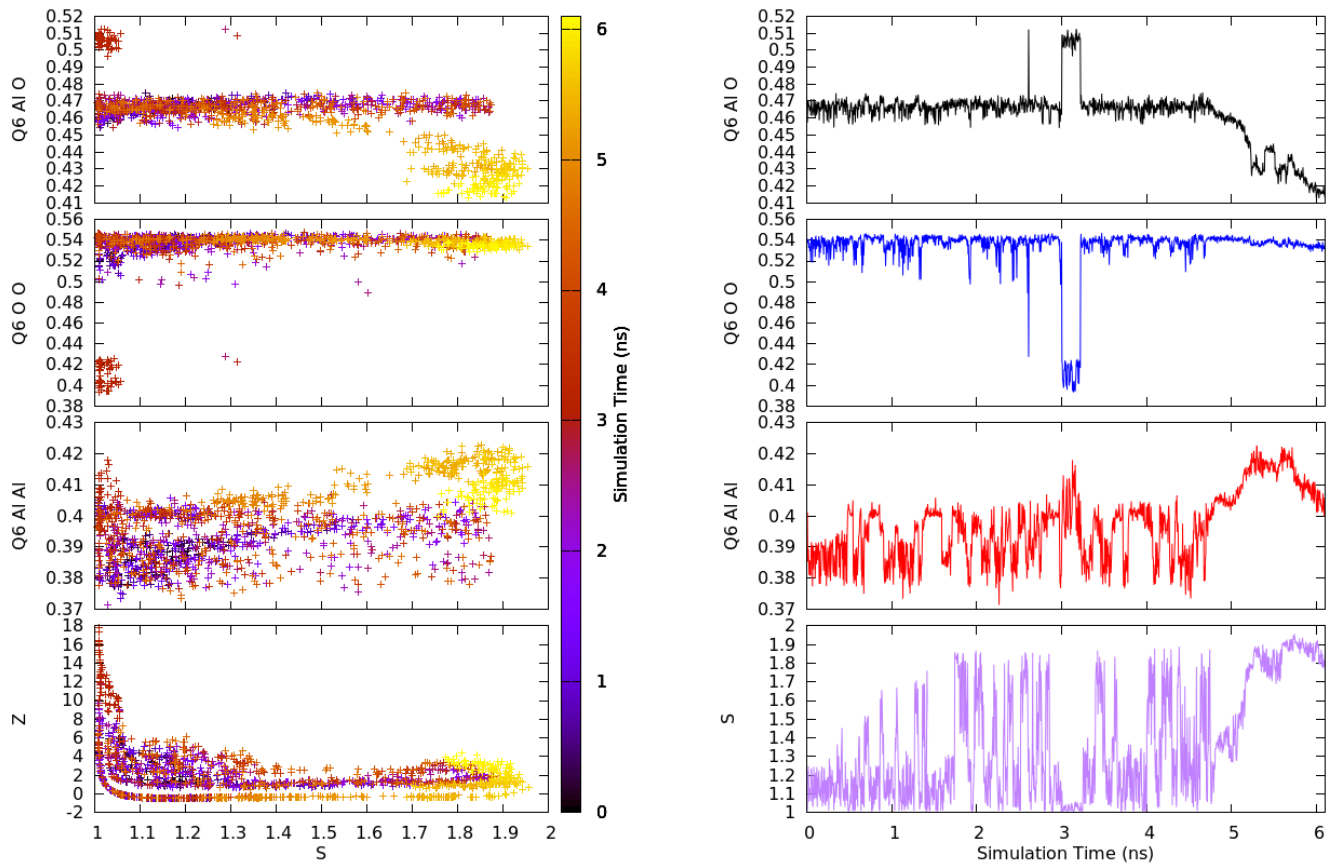


Figure 48: The variation of Steinhardt parameter Q_6 between different atoms of the system along the transition from theta to gamma structure at 1200K as function of time(ns) (left) and s (right).

5.4 Transitions between Alpha and Theta structures

In this chapter, we will be presenting the transformation from **Theta to Alpha alumina at 1500K**. SF_2 is the switching function used between Aluminum atoms and SF_3 between the rest of the atoms in the system, moreover we used the following simulation parameters: $\delta s = 0.0087$, $\delta z = 0.1$, $h = 0.0497$ Kcal/mol, added every 1000 steps.

Analyzing the progress of the transformation in Figure 49, we see that the system escaped the Theta region at 3.3ns to reach a basin at high Z (orange color, structure I). Afterwards, the system returned to the initial basin (theta) and then completed the transformation by reaching the Alpha structure at around 5.6ns. To characterize the new metastable structure (high Z basin) we started normal MDs at each energy minima region and computed both RDFs and CNs. The comparison between RDFs and CNs of these structures are shown in Figure 50 and it points out that the three structures are different in both Aluminum and Oxygen atoms distributions.

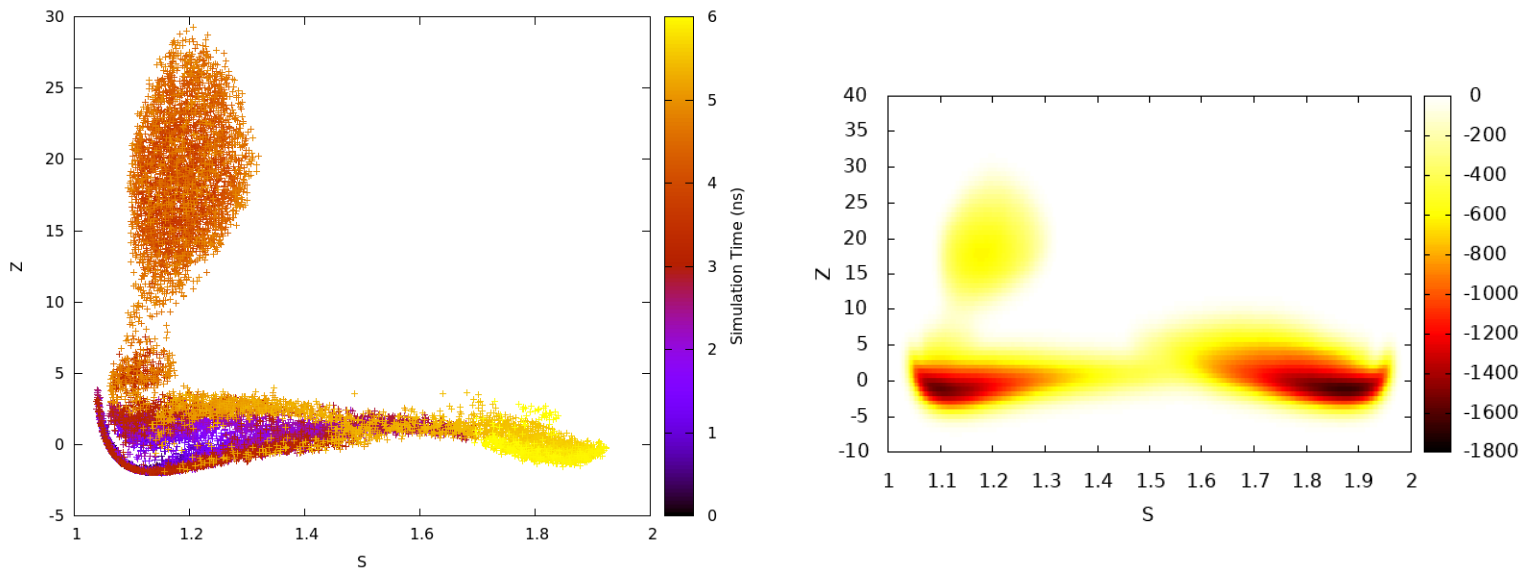


Figure 49: 3D graph showing the A) time progress of the metadynamics simulation at 1500K starting from the theta to alpha structure as function of simulation time (ns) and B) Unconverged free energy profile in the $s - z$ space.

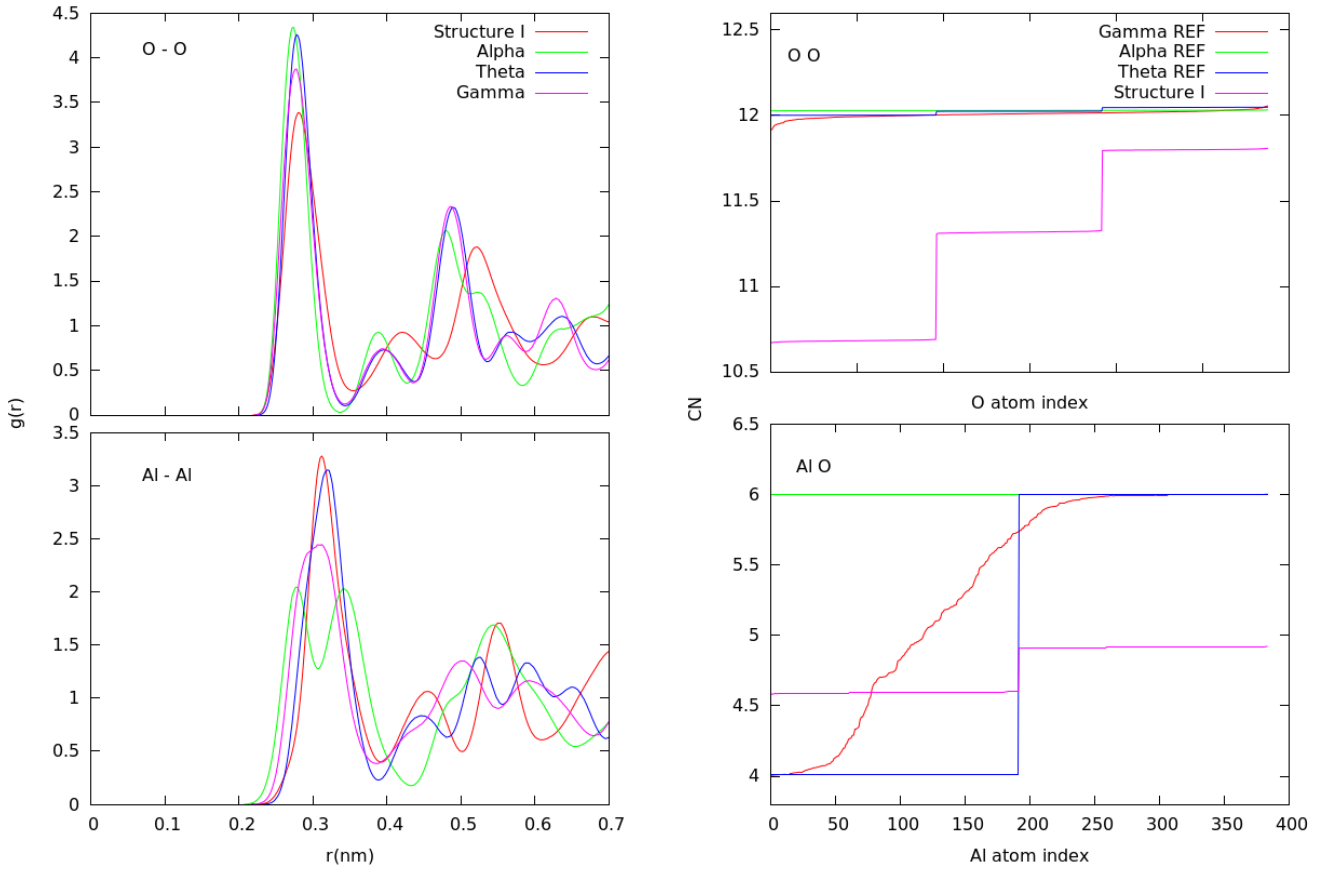


Figure 50: A) RDFs of the 3 structures present in the transformation (theta, alpha and the structure I). B) Coordination Numbers of atoms as function of atom index of different phase structures.

Figures 51 and 52 show that as for the “alpha to gamma” transformation at the same temperature the parameters change smoothly during the transformation, the only discrete step we see is the “jump” to the new structure basin. The transition from theta to the new structure I is characterized by a decrease in the number of 4-coordinated (tetrahedral) Aluminum atoms, accompanied by an increase of Aluminum atoms in Octahedral sites. Correspondingly, the oxygen sublattice changes as shown by the Q_6 and Q_4 O-O plot in Figure 52. As expected, after comparison with the perfect lattice parameters present in Table 2, the Oxygen network changed orientation from fcc lattice in the theta alumina into hcp lattice in the alpha alumina structure. Unfortunately, the Oxygen network of the structure I is not one of the perfect lattices studied by

the work of Hossein Eslami et al. [63] (the Q4 and Q6 O-O values reached in this region can't be compared to any perfect lattice parameters present in the study). These rearrangements of atoms are associated with a major increase in the volume of the cell (Figure 53).

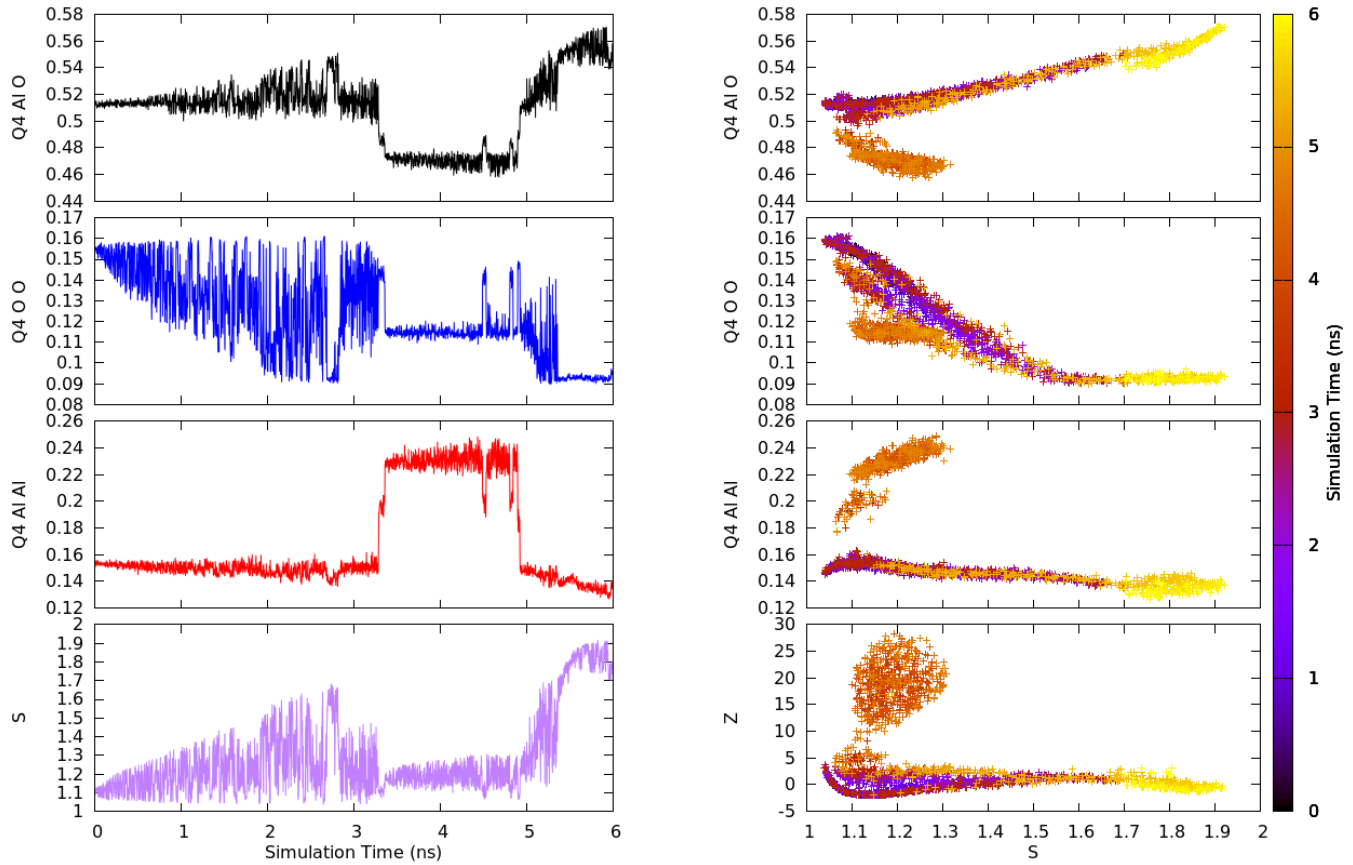


Figure 51: The variation of Steinhardt parameter Q4 between different atoms of the system along the transition from theta to alpha structure as function of time(ns) (left) and s (right).

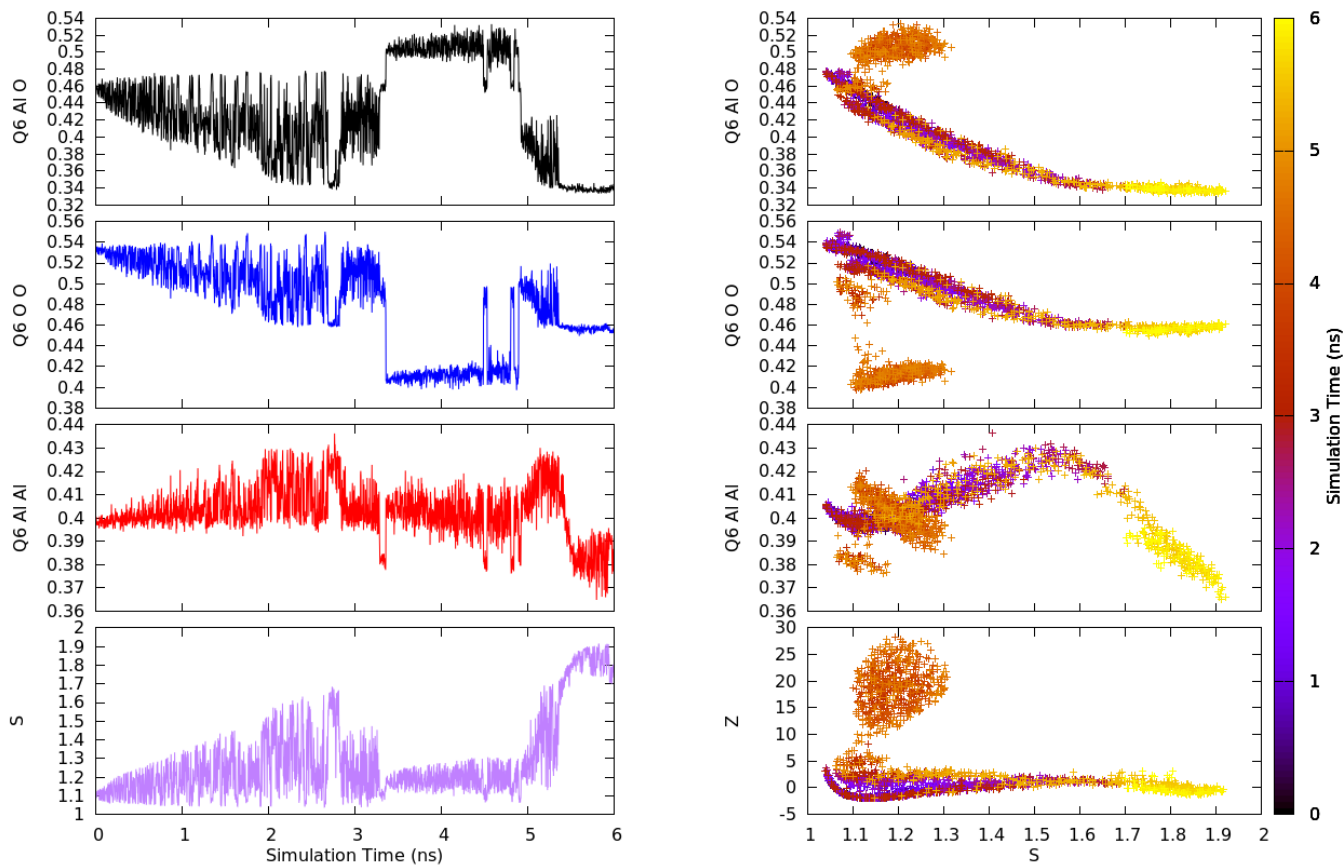


Figure 52: The variation of Steinhardt parameter Q_6 between different atoms of the system along the transition from theta to alpha structure as function of time(ns) (left) and s (right).

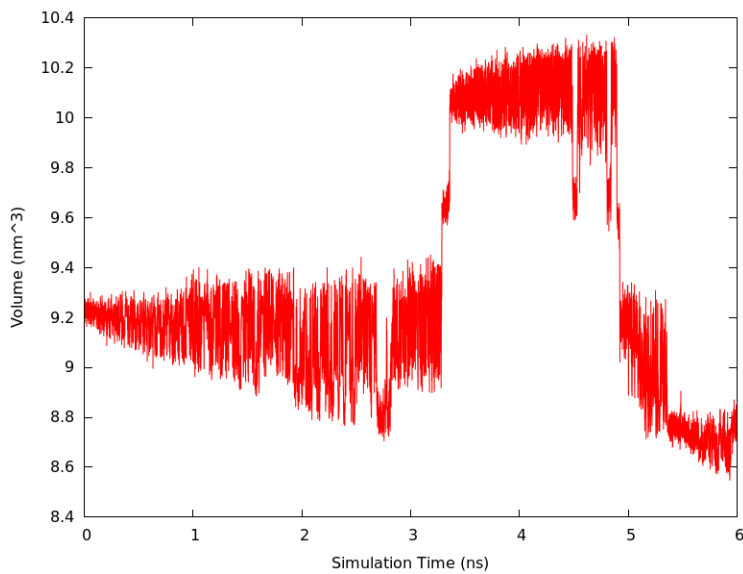


Figure 53: Convergence of the Volume of unit cell during the transformation of theta to alpha structure.

Chapter 6 Conclusions

In this work, we have succeeded to perform and track phase transitions between alumina structures using the recently proposed PIV-PathCV collective variables[54].

In chapter 4, we present a first MD and enhanced sampling study of the crystallization of gamma alumina from the amorphous and liquid phases at different temperatures. We show that the crystallization of gamma alumina is the first step towards the formation of alpha alumina and it proceeds in two steps: firstly, the Aluminum/Oxygen reciprocal orientation moves towards a tetrahedral geometry arrangement, and finally the oxygen network rearranges in a face-centered-cubic unit cell.

We remark that the crystallization of the gamma alumina from the amorphous/liquid phase, towards the formation of alpha alumina, has also been found experimentally[73].

Moreover, we analyze the temperature dependence of the free energy profiles for the gamma alumina crystallization, showing that at low temperature (800-1000K) the free energy difference between the gamma alumina and the amorphous state decreases as a function of temperature. On the contrary, at high temperature i.e., when the diffusion of atoms increases, the disordered state (amorphous/liquid) becomes more and more stable with respect to gamma alumina and the free energy difference increases as a function of temperature.

In chapter 6, first we studied the phase transformation between two stable structures i.e., from Gamma to Alpha alumina, at different temperatures ranging from 500K to 1500K (near the melting point). We show that the system changes by discrete steps and passes by different metastable structures before reaching the Gamma Alumina. The mechanism of the transformation can be summarized by the change in the ordering of the Oxygen network accompanied by the movement of Aluminum atoms from the tetrahedral to Octahedral sites. After that, we have seen

that the transformation free energy becomes smoother (lower energy barriers among intermediates) as the temperature increases.

In the last two chapters we presented the transitions between Theta to Gamma and Theta to Alpha structures. The FES of the transformation from Theta to Gamma shows a direct transition with a small energy difference between the two structures and a tiny barrier between them. While the system starting from Theta structure visited a metastable phase at high Z value before reaching the specified Alpha Alumina. Such an unexpected new phase discovered by the system differs from all reference structures studied in this work. We shall characterize this structure in more detail in the future.

Other transitions between alumina phases may be studied in a future work. It will then be possible to determine the direct transformation and confirm the experimental transformation scheme.

More generally, we presented a demonstration that it is possible to investigate complex transformations involving a large number of atoms without any input on the reaction mechanism or on the reaction coordinate. The extension of the methodology to other complex transformations will depend on the possibility to perform rapidly long metadynamics calculations. Except for very peculiar systems, these calculations are not possible at the quantum/DFT level. The development of reactive force fields may be a good alternative to study complex chemical reactions in liquid phase, including explicitly the solvent molecules. Finally, we remark that this work contributes to the validation of the PIV-PathCV as a general computational tool for the study of complex transformations including the ones involving ionic systems with high energy barriers separating the different (meta)stable phases; in fact, it provides structures and energetics of the full

transformation path including the transition state. In future works we shall address the problem of simulating chemical reactions in solutions and/or on surfaces.

Chapter 7 References

- [1] J. T. Gopinath, M. Soljačić, E. P. Ippen, V. N. Fuflyigin, W. A. King, and M. Shurgalin, “Third order nonlinearities in Ge-As-Se-based glasses for telecommunications applications,” *J. Appl. Phys.*, vol. 96, no. 11, pp. 6931–6933, Dec. 2004, doi: 10.1063/1.1805182.
- [2] A. M. Gatti, G. Valdrè, and A. Tombesi, “Importance of microanalysis in understanding mechanism of transformation in active glassy biomaterials,” *J. Biomed. Mater. Res.*, vol. 31, no. 4, pp. 475–480, Aug. 1996, doi: 10.1002/(SICI)1097-4636(199608)31:4<475::AID-JBM6>3.0.CO;2-I.
- [3] C. B. TAYLOR and V. G. COLLINS, “Development of bacteria in waters stored in glass containers.,” *J. Gen. Microbiol.*, vol. 3, no. 1, pp. 32–42, Jan. 1949, doi: 10.1099/00221287-3-1-32.
- [4] R. O. Dror *et al.*, “Structural basis for modulation of a G-protein-coupled receptor by allosteric drugs,” *Nat. 2013 5037475*, vol. 503, no. 7475, pp. 295–299, Oct. 2013, doi: 10.1038/NATURE12595.
- [5] G. B. Dawe *et al.*, “Distinct Structural Pathways Coordinate the Activation of AMPA Receptor-Auxiliary Subunit Complexes,” *Neuron*, vol. 89, no. 6, pp. 1264–1276, Mar. 2016, doi: 10.1016/J.NEURON.2016.01.038.
- [6] S. Pipolo, M. Salanne, G. Ferlat, S. Klotz, A. M. Saitta, and F. Pietrucci, “Navigating at Will on the Water Phase Diagram,” *Phys. Rev. Lett.*, vol. 119, no. 24, p. 245701, Dec. 2017, doi: 10.1103/PhysRevLett.119.245701.
- [7] Y. Jiang, B. Wang, C. Xu, J. Z.- Metals, and undefined 2020, “Atomistic Simulation of the Strain Driven Phase Transition in Pure Iron Thin Films Containing Twin Boundaries,” *mdpi.com*, Accessed: Jan. 11, 2022. [Online]. Available: <https://www.mdpi.com/769618>.
- [8] T. Taniguchi, H. Sato, Y. Hagiwara, T. Asahi, and H. Koshima, “Photo-triggered phase transition of a crystal,” *Commun. Chem. 2019 21*, vol. 2, no. 1, pp. 1–10, Feb. 2019, doi: 10.1038/S42004-019-0121-8.
- [9] S. L. Chaplot, “Molecular dynamics simulation of phase transitions and melting in MgSiO₃ with the perovskite structure,” *Am. Mineral.*, vol. 83, no. 9–10, pp. 937–941, 1998, doi: 10.2138/AM-1998-9-1001/HTML.

- [10] L. Grajcarova, "Simulations of structural phase transitions in crystals using ab initio metadynamics." Sep. 30, 2013, Accessed: Jan. 04, 2022. [Online]. Available: http://inis.iaea.org.ressources-electroniques.univ-lille.fr/Search/search.aspx?orig_q=RN:50034035.
- [11] A. D. Becke, "Density Functional Theories in Quantum Chemistry," pp. 165–179, Jun. 1989, doi: 10.1021/BK-1989-0394.CH012.
- [12] WEFERS and K., "Oxides and Hydroxides of Aliminum," *Alcoa Tech. Pap.*, vol. 19, p. 18, 1987, Accessed: Jul. 01, 2021. [Online]. Available: <https://ci.nii.ac.jp/naid/20000409742>.
- [13] J. Fierro, *Metal oxides: chemistry and applications*. 2005.
- [14] "View of REVIEW OF ALUMINA IN ADSORPTION PROCESSES FOR EMERGING POLLUTANTS | International Journal of Research -GRANTHAALAYAH." <https://www.granthaalayahpublication.org/journals/index.php/granthaalayah/article/view/3846/3864> (accessed Jan. 01, 2022).
- [15] S. Ciraci and I. P. Batra, "Electronic structure of γ -alumina and its defect states," *Phys. Rev. B*, vol. 28, no. 2, pp. 982–992, 1983, doi: 10.1103/PHYSREVB.28.982.
- [16] P. S. Santos, H. S. Santos, and S. P. Toledo, "Standard transition aluminas. Electron microscopy studies," *Mater. Res.*, vol. 3, no. 4, pp. 104–114, Oct. 2000, doi: 10.1590/s1516-14392000000400003.
- [17] H. C. Stumpf, A. S. Russell, J. W. Newsome, and C. M. Tucker, "Thermal Transformations of Aluminas and Alumina Hydrates - Reaction with 44% Technical Acid.," *Ind. Eng. Chem.*, vol. 42, no. 7, pp. 1398–1403, Jul. 1950, doi: 10.1021/ie50487a039.
- [18] F. W. DYNYS and J. W. HALLORAN, "Alpha Alumina Formation in Alum-Derived Gamma Alumina," *J. Am. Ceram. Soc.*, vol. 65, no. 9, pp. 442–448, Sep. 1982, doi: 10.1111/j.1151-2916.1982.tb10511.x.
- [19] I. Levin and D. Brandon, "Metastable alumina polymorphs: Crystal structures and transition sequences," *J. Am. Ceram. Soc.*, vol. 81, no. 8, pp. 1995–2012, Aug. 1998, doi: 10.1111/j.1151-2916.1998.tb02581.x.
- [20] L. Kovarik, M. Bowden, A. Genc, J. Szanyi, C. H. F. Peden, and J. H. Kwak, "Structure of δ -alumina: Toward the atomic level understanding of transition alumina phases," *J. Phys. Chem. C*, vol. 118, no. 31, pp. 18051–18058, Aug. 2014, doi: 10.1021/jp500051j.
- [21] A. Boumaza *et al.*, "Transition alumina phases induced by heat treatment of boehmite: An

- X-ray diffraction and infrared spectroscopy study,” *J. Solid State Chem.*, vol. 182, no. 5, pp. 1171–1176, May 2009, doi: 10.1016/j.jssc.2009.02.006.
- [22] X. Krokidis, P. Raybaud, A.-E. Gobichon, B. Rebours, P. Euzen, and H. Toulhoat, “Theoretical study of the dehydration process of boehmite to γ -alumina,” *ACS Publ.*, vol. 105, no. 22, pp. 5121–5130, Jun. 2001, doi: 10.1021/jp0038310.
- [23] J. W. Mintmire, “Energetics of aluminum vacancies in gamma alumina,” *Phys. Rev. B - Condens. Matter Mater. Phys.*, vol. 60, no. 2, pp. 773–777, Jul. 1999, doi: 10.1103/PhysRevB.60.773.
- [24] N. M. Stuart and K. Sohlberg, “The Microstructure of γ -Alumina,” *Energies 2021, Vol. 14, Page 6472*, vol. 14, no. 20, p. 6472, Oct. 2021, doi: 10.3390/EN14206472.
- [25] S. H. Cai, S. N. Rashkeev, S. T. Pantelides, and K. Sohlberg, “Phase transformation mechanism between γ - and θ -alumina,” *Phys. Rev. B - Condens. Matter Mater. Phys.*, vol. 67, no. 22, p. 224104, Jun. 2003, doi: 10.1103/PhysRevB.67.224104.
- [26] S. Lamouri *et al.*, “Control of the γ -alumina to α -alumina phase transformation for an optimized alumina densification,” *Boletin de la Sociedad Espanola de Ceramica y Vidrio*, vol. 56, no. 2. Sociedad Espanola de Ceramica y Vidrio, pp. 47–54, Mar. 01, 2017, doi: 10.1016/j.bsecv.2016.10.001.
- [27] J. Neumann, “Molecular dynamics simulations of protein-protein interactions and THz driving of molecular rotors on gold,” 2011.
- [28] R. Y. Rubinstein and D. P. Kroese, *Simulation and the Monte Carlo Method*, 3rd ed. Wiley Publishing, 2016.
- [29] E. Paquet and H. L. Viktor, “Molecular dynamics, monte carlo simulations, and langevin dynamics: A computational review,” *BioMed Research International*, vol. 2015. Hindawi Publishing Corporation, 2015, doi: 10.1155/2015/183918.
- [30] J. Hafner, “Ab-initio simulations of materials using VASP: Density-functional theory and beyond,” *J. Comput. Chem.*, vol. 29, no. 13, pp. 2044–2078, 2008, doi: 10.1002/JCC.21057.
- [31] X. Gonze *et al.*, “A brief introduction to the ABINIT software package,” *Zeitschrift fur Krist.*, vol. 220, no. 5–6, pp. 558–562, May 2005, doi: 10.1524/ZKRI.220.5.558.65066/MACHINEREADABLECITATION/RIS.
- [32] D. A. Case *et al.*, “AMBER 2020,” *Univ. Calif.*, 2020.
- [33] B. R. Brooks *et al.*, “CHARMM: the biomolecular simulation program,” *J. Comput. Chem.*,

- vol. 30, no. 10, pp. 1545–1614, 2009.
- [34] H. Bekker *et al.*, “Gromacs: A parallel computer for molecular dynamics simulations,” in *Physics computing*, 1993, vol. 92, pp. 252–256.
- [35] J. C. Phillips *et al.*, “Scalable molecular dynamics on CPU and GPU architectures with NAMD,” *J. Chem. Phys.*, vol. 153, no. 4, p. 44130, 2020.
- [36] B. J. Alder and T. E. Wainwright, “Phase Transition for a Hard Sphere System,” *J. Chem. Phys.*, vol. 27, no. 5, pp. 1208–1209, Nov. 1957, doi: 10.1063/1.1743957.
- [37] M. Karplus, J. A. McCammon, and B. R. Gelin, “Dynamics of folded proteins,” *Nature*, vol. 267, no. June, pp. 585–590, 1977, [Online]. Available: https://www.nature.com/articles/267585a0.pdf%0Ahttp://www.msg.ucsf.edu/BI204/Discussion/Q1/Jacobson/MacCammon_1977.pdf.
- [38] M. Levitt and S. Lifson, “Refinement of protein conformations using a macromolecular energy minimization procedure,” *J. Mol. Biol.*, vol. 46, no. 2, pp. 269–279, 1969, doi: 10.1016/0022-2836(69)90421-5.
- [39] Loup VzzLzrt, “Computer ‘Experiments’ on Classical Fluids. I. Thermodynamical Properties of Lennard-Jones Molecules,” *Phys. Rev. Lett.*, vol. 159, no. 5, 1967.
- [40] P. Steneteg, “Development of molecular dynamics methodology for simulations of hard materials.” Linköping University Electronic Press, 2012.
- [41] S. Lid, S. Köppen, and L. Colombi Ciacchi, “Creation of models and parametrization of a classical force field for amorphous Al₂O₃/water interfaces based on Density Functional Theory,” *Comput. Mater. Sci.*, vol. 140, pp. 307–314, Dec. 2017, doi: 10.1016/j.commatsci.2017.09.003.
- [42] M. Matsui, “A transferable interatomic potential model for crystals and melts in the system CaO-MgO-Al₂O₃-SiO₂,” *MinM*, vol. 58, no. 2, pp. 571–572, 1994.
- [43] A. Toukmaji, J. B. J.-C. physics communications, and undefined 1996, “Ewald summation techniques in perspective: a survey,” *Elsevier*, Accessed: Jan. 05, 2022. [Online]. Available: <https://www.sciencedirect.com/science/article/pii/0010465596000161>.
- [44] T. Darden, D. York, and L. Pedersen, “Particle mesh Ewald: An N·log(N) method for Ewald sums in large systems,” *J. Chem. Phys.*, vol. 98, no. 12, p. 10089, Aug. 1998, doi: 10.1063/1.464397.
- [45] U. Essmann, L. Perera, M. L. Berkowitz, T. Darden, H. Lee, and L. G. Pedersen, “A smooth

- particle mesh Ewald method,” *J. Chem. Phys.*, vol. 103, no. 19, pp. 8577–8593, Nov. 1995, doi: 10.1063/1.470117.
- [46] L. Verlet, “Computer ‘Experiments’ on Classical Fluids. I. Thermodynamical Properties of Lennard-Jones Molecules,” *Phys. Rev.*, vol. 159, no. 1, p. 98, Jul. 1967, doi: 10.1103/PhysRev.159.98.
- [47] W. C. Swope, H. C. Andersen, P. H. Berens, and K. R. Wilson, “A computer simulation method for the calculation of equilibrium constants for the formation of physical clusters of molecules: Application to small water clusters,” *J. Chem. Phys.*, vol. 76, no. 1, p. 637, Oct. 1998, doi: 10.1063/1.442716.
- [48] M. A. González, “Force fields and molecular dynamics simulations,” *JDN*, vol. 12, pp. 169–200, 2011, [Online]. Available: <https://doi.org/10.1051/sfn/201112009>.
- [49] O. Valsson and M. Parrinello, “Variational Approach to Enhanced Sampling and Free Energy Calculations,” vol. 090601, no. August, pp. 1–5, 2014, doi: 10.1103/PhysRevLett.113.090601.
- [50] R. Lazim, D. Suh, and S. Choi, “Advances in Molecular Dynamics Simulations and Enhanced Sampling Methods for the Study of Protein Systems,” *International Journal of Molecular Sciences*, vol. 21, no. 17. 2020, doi: 10.3390/ijms21176339.
- [51] A. Onuki, *Phase transition dynamics*. 2002.
- [52] A. Barducci, M. Bonomi, and M. Parrinello, “Metadynamics,” *Wiley Interdisciplinary Reviews: Computational Molecular Science*, vol. 1, no. 5. John Wiley & Sons, Ltd, pp. 826–843, Sep. 01, 2011, doi: 10.1002/wcms.31.
- [53] G. Fiorin, M. L. Klein, and J. Héning, “Using collective variables to drive molecular dynamics simulations,” *Mol. Phys.*, vol. 111, no. 22–23, pp. 3345–3362, 2013, doi: 10.1080/00268976.2013.813594.
- [54] S. Pipolo, M. Salanne, G. Ferlat, S. Klotz, A. M. Saitta, and F. Pietrucci, “Navigating at Will on the Water Phase Diagram,” *Phys. Rev. Lett.*, vol. 119, no. 24, pp. 1–5, 2017, doi: 10.1103/PhysRevLett.119.245701.
- [55] G. A. Gallet and F. Pietrucci, “Structural cluster analysis of chemical reactions in solution,” *J. Chem. Phys.*, vol. 139, no. 7, p. 074101, Aug. 2013, doi: 10.1063/1.4818005.
- [56] G. M. Torrie and J. P. Valleau, “Nonphysical sampling distributions in Monte Carlo free-energy estimation: Umbrella sampling,” *J. Comput. Phys.*, vol. 23, no. 2, pp. 187–199, Feb.

- 1977, doi: 10.1016/0021-9991(77)90121-8.
- [57] A. G.- version and undefined 2012, “WHAM: the weighted histogram analysis method.”
- [58] S. Kumar, D. Bouzida, R. H. Swendsen, P. A. Kollman, and J. M. Rosenberg, “Liquid-liquid transition in ST2 water,” *J. Comput. Chem*, vol. 13, pp. 1011–1021, 1992.
- [59] G. E. M. Jauncey, “The Scattering of X-Rays and Bragg’s Law,” *Proc. Natl. Acad. Sci. U. S. A.*, vol. 10, no. 2, p. 57, Feb. 1924, doi: 10.1073/PNAS.10.2.57.
- [60] B. Greenberg and IUCr, “Bragg’s law with refraction,” *urn:issn:0108-7673*, vol. 45, no. 3, pp. 238–241, Mar. 1989, doi: 10.1107/S0108767388012243.
- [61] P. J. Steinhardt, D. R. Nelson, and M. Ronchetti, “Bond-orientational order in liquids and glasses,” *Phys. Rev. B*, vol. 28, no. 2, p. 784, Jul. 1983, doi: 10.1103/PhysRevB.28.784.
- [62] W. Mickel, S. C. Kapfer, G. E. Schröder-Turk, and K. Mecke, “Shortcomings of the bond orientational order parameters for the analysis of disordered particulate matter,” *J. Chem. Phys.*, vol. 138, no. 4, p. 044501, Jan. 2013, doi: 10.1063/1.4774084.
- [63] H. Eslami, P. Sedaghat, and F. Müller-Plathe, “Local bond order parameters for accurate determination of crystal structures in two and three dimensions,” *Phys. Chem. Chem. Phys.*, vol. 20, p. 27059, 2018, doi: 10.1039/c8cp05248d.
- [64] U. Gasser, F. Ziese, G. M.-T. E. P. J. Special, and undefined 2014, “Characterization of local structures with bond-order parameters and graphs of the nearest neighbors, a comparison,” *Springer*, vol. 223, no. 3, pp. 455–467, Feb. 2014, doi: 10.1140/epjst/e2014-02102-6.
- [65] “PLUMED 2: New feathers for an old bird,” *Elsevier*, Accessed: Oct. 14, 2020. [Online]. Available: https://www.sciencedirect.com/science/article/pii/S0010465513003196?casa_token=mwe_cjd_igfQAAAAA:PFdqkXtlh-cyeOCuQZI22hUsDeQpmCmTEiRGz6UHbfhMk0P2y4E8YoIIwRzgW9lzkgmEfglSe9I1.
- [66] M. Bonomi *et al.*, “PLUMED: A portable plugin for free-energy calculations with molecular dynamics,” *Comput. Phys. Commun.*, vol. 180, no. 10, pp. 1961–1972, Oct. 2009, doi: 10.1016/j.cpc.2009.05.011.
- [67] T. D. Kühne *et al.*, “CP2K: An electronic structure and molecular dynamics software package - Quickstep: Efficient and accurate electronic structure calculations,” *J. Chem. Phys.*, vol. 152, no. 19, p. 194103, May 2020, doi: 10.1063/5.0007045.

- [68] W. Humphrey, A. Dalke, K. S.-J. of molecular graphics, and undefined 1996, “VMD: visual molecular dynamics,” *csb.pitt.edu*, Accessed: Oct. 09, 2020. [Online]. Available: <https://www.csb.pitt.edu/BBSI/2007/lectures/VMD.pdf>.
- [69] W. E. Lee and K. P. D. Lagerlof, “Structural and electron diffraction data for sapphire (α - Al_2O_3),” *J. Electron Microsc. Tech.*, vol. 2, no. 3, pp. 247–258, 1985, doi: 10.1002/JEMT.1060020309.
- [70] E. Husson, Y. R.-E. journal of solid state and, and undefined 1996, “Structural studies of transition aluminas. Theta alumina,” *pascal-francis.inist.fr*, Accessed: Sep. 12, 2022. [Online]. Available: <https://pascal-francis.inist.fr/vibad/index.php?action=getRecordDetail&idt=2544467>.
- [71] B. Hamieh, “Genèse de catalyseurs d’HDS CoMoP sur Al_2O_3 (+Si) et SBA(+Al) : rôle du support sur la nature et la dispersion des phases oxydes et sulfures,” *http://www.theses.fr*, Jun. 2021, Accessed: Aug. 17, 2022. [Online]. Available: <http://www.theses.fr/2021LILUR049>.
- [72] G. S. Hammond, “A Correlation of Reaction Rates,” *J. Am. Chem. Soc.*, vol. 77, no. 2, pp. 334–338, 1955, doi: 10.1021/JA01607A027/ASSET/JA01607A027.FP.PNG_V03.
- [73] V. Jayaram and C. G. Levi, “The structure of δ -alumina evolved from the melt and the $\gamma \rightarrow \delta$ transformation,” *Acta Metall.*, vol. 37, no. 2, pp. 569–578, Feb. 1989, doi: 10.1016/0001-6160(89)90240-X.